Friedrich-Schiller-Universität Jena
Physikalisch-Astronomische Fakultät
Thüringer Landessternwarte Tautenburg

Radio Relics: A Joint Analysis of Surveys and Simulations

Dissertation
zur Erlangung des akademischen Grades
doctor rerum naturalium (Dr. rer. nat.)

vorgelegt dem Rat der Physikalisch-Astronomischen Fakultät
der Friedrich-Schiller-Universtität Jena

von **MSc. Jakob Gelszinnis**
geboren am 05.05.1989 in Jena, Deutschland

Gutachter

1. :	**Prof. Dr. Artie Hatzes**	Friedrich-Schiller-Universität, Jena
2. :	**Prof. Dr. Francesco de Gasperin**	Universität Hamburg
3. :	**Prof. Dr. Christoph Pfrommer**	Leibniz-Institut für Astrophysik Potsdam

Tag der öffentlichen Verteidigung: 12.05.2020

Zugl.: Dissertation, Friedrich-Schiller-Universität Jena, 2020

Zusammenfassung

Wir präsentieren eine homogene Zusammenstellung und Analyse von Radiorelikten in durchgeführten und synthetischen Himmelsdurchmusterungen bei 1.4 GHz. Unser Ziel ist es, die Physik der kosmischen Strahlung und die magnetischen Eigenschaften des Haufengases (engl. *intracluster medium*, ICM) zu bestimmen.

Als Datenbasis stellen wir einen aktualisierten Katalog von Radiorelikten innerhalb der *NRAO VLA Sky Survey* (Condon et al., 1998) zusammen. Für die synthetische Himmelsdurchmusterung verbessern wir den von uns in Nuza et al. (2017) entwickelten Ansatz, indem wir die Verstärkung von Magnetfeldern durch Stoßkompression und die Unvollständigkeit der Durchmusterung gegenüber kompakten Radiorelikten sorgfältiger betrachten. Wir untersuchen das Synchrotronemissionsmodell von Hoeft and Brüggen (2007), welches diffuse Stoßbeschleunigung (engl. *diffusive shock acceleration*, DSA) von thermischen Elektronen des Haufengases beschreibt.

Wir führen erstmals eine likelihood-freie Parameterabschätzung der Eigenschaften des Haufengases mittels einer Approximativen Bayesianischen Berechnung durch. Diese Abschätzungsmethode basiert auf dem Auswählen von synthetischen Himmelsdurchmusterungen nach größtmöglicher Ähnlichkeit zu den Beobachtungsdaten. Während eine deutliche Übereinstimmung in Detektionshäufigkeit und Leuchtkraft-Größenverteilung von Relikten erzielt werden kann, tendieren beobachtete Relikte weiter zur Peripherie der Galaxienhaufen und weisen ein im Mittel steileres Spektrum auf. Der geschätzte Anteil der thermalisierten Stoßwellenenergie, welcher durch DSA in die Elektronen fließt, ist $\log_{10}(\xi_\mathrm{e}) = 5.0 \pm 0.2$ bei Magnetfeldstärken des Haufengases von $\log_{10}(B_0/\,\mu\mathrm{G}) = 1.4^{+0.7}_{-0.7} + 0.53^{+0.40}_{-0.49} \log_{10}(n_\mathrm{e}/10^{-4}\,\mathrm{cm}^{-3})$. Das Modell lässt darauf schließen, dass die Hälfte der Relikte mit spektralen Flussdichten über 3.6 mJy noch unentdeckt ist. Zuletzt zeigen wir, dass eine Erweiterung des Modells mit bereits vorhandenen hoch-relativistischen Elektronen im Haufengas die Übereinstimmung mit der Datenbasis nicht signifikant verbessert.

Unsere Arbeit zeigt, wie die Kombination von Himmelsdurchmusterungen und kosmologischen Simulationen zur Modellbildung genutzt werden kann, Radiorelikte im Speziellen für Modelle der Teilchenbeschleunigung und Magnetfelder im Haufengas.

Abstract

We present the compilation of a homogeneous sample and analysis of radio relics found in actual and mock sky surveys at 1.4 GHz. We aim at setting constraints on the physics of cosmic ray (CR) electrons and the magnetic fields in the intracluster medium (ICM).

As the observational data, we compile an updated catalog of radio relics found in the NRAO VLA Sky Survey (Condon et al., 1998). For the synthetic sky survey, we improve the scheme that we developed in Nuza et al. (2017) by considering amplification of magnetic fields through shock compression and a more careful consideration of the survey incompleteness towards compact radio relics. We investigate the synchrotron emission model of Hoeft and Brüggen (2007) - corresponding to diffusive shock acceleration (DSA) of electrons of ICM electrons from the thermal pool.

We are the first to present the results of a likelihood-free parameter inference on ICM properties with approximate Bayesian computation. This approach is based on ranking samples of synthetic sky surveys against the observational data, each trial with an individual set of model parameters. While considerable agreement in detection counts and power-size distribution can be reached, observed relics tend to be farther away and have on average steeper integrated spectral index than their simulated counterparts for all reasonable parameter sets. The estimated fraction of thermalized shock energy put into electrons by the DSA mechanism is $\log_{10}(\xi_\mathrm{e}) = 5.0 \pm 0.2$ at an ICM magnetic field strength of $\log_{10}(B_0/\,\mu\mathrm{G}) = 1.4^{+0.7}_{-0.7} + 0.53^{+0.40}_{-0.49}\,\log_{10}(n_\mathrm{e}/10^{-4}\,\mathrm{cm}^{-3})$. The model also suggests that half the relics above a flux density of 3.6 mJy are yet undiscovered. Lastly, we show that an expansion of the modeling including a population of pre-existing CR-electrons in the ICM does not significantly improve the match between model and data.

Our work demonstrates how the combined usage of sky surveys and cosmological simulations can be used to infer model parameters. Radio relic surveys, in particular, can be regarded as tools to study particle acceleration and magnetic fields in the ICM.

Acknowledgments

Firstly, I want to thank Matthias Hoeft who gave me the opportunity to work at his group of young scientists, and supported this thesis as the technical supervisor throughout all the years. Great thanks goes to him and Sebastian E. Nuza who always supported me during this endeavor, pushed forward the surveys project that became an inherent part of my thesis, and did a lot of commenting on the different stages of this thesis.

I thank my dear colleagues and friends Alexander Drabent, Kamlesh Rajpurohit, and Cosmos Dumba who fostered my research through their questions and channeled my wide interests on the topic of this thesis. Same applies to my dear colleagues and friends Michael Hartmann, Frank Pertermann, Silvia Sabotta, and Thomas Sperling who went on the journey of attaining a PhD together with me. They and Simon Oberhauser helped to significantly improve this transcript with their suggestions and through their proofreading. Even more, I will greatly miss our joint tea breaks.

Many thanks goes to all of my other colleagues at the Thueringian State Observatory which created an environment that fostered my professional and personal growth during my time as a PhD student.

Thanks and thoughts goes to my kind family - my parents, brothers, grandparents, and my small nephews - as well as the beloved person I met along the way.

Acknowledgments of funding:
This work was made possible by being part of the *Deutsche Forschungs Gesellschaft* Research Unit 1254 in the project *A6: Magnetic fields* and by receiving stipend funds from the Thueringian State observatory.

Acknowledgments of used software:
This research made use of APLpy (2011, 2012, 2013 Smithsonian Astrophysical Observatory), an open-source plotting package for Python (Robitaille & Bressert 2012); Astropy, a community-developed core Python package for astronomy (Astropy Collaboration et al. 2013); ABCpmc (Akeret et al., 2015); and the visualization tool *corner* (Salvatier et al., 2016).

Contents

List of Figures

List of Tables

Chapter 1

Radio Relics in Galaxy Clusters

> To try to write a grand cosmical drama leads necessarily to myth. To try to let knowledge substitute ignorance in increasingly large regions of space and time is science.
>
> Hannes Alfvén in 'Cosmology: Myth or Science?' (1984)

Due to observations and simulations we know that matter on cosmological scales is distributed in a foam-like structure of large under-dense volumes, separated by lower dimensional structures of higher density. Galaxy clusters constitute the nodes of this matter distribution. They are convergence zones of matter flows thus comprising the largest virialized systems in our universe. A typical galaxy cluster contains hundreds of galaxies embedded in a Mpc-size dark matter halo, as well as a large amount of hot plasma permeating the clusters volume. This intracluster medium (ICM) represents most of the baryonic mass in galaxy clusters.

Mergers with other galaxy clusters or groups of galaxies and the infall of gas onto the clusters drive turbulence and shocks within the ICM. From these disturbances, particles in the ICM can gain energy through plasma interactions. Some electrons are accelerated to highly relativistic energies and form a population of cosmic rays. In the presence of magnetic fields the latter emit synchrotron radiation. We know about these processes because we observe the resulting synchrotron radio emission in galaxy clusters with radio telescopes. This so-called *diffuse radio emission* incorporates phenomena known as *radio relics*, *radio halos*, and *radio mini-halos*.

These phenomena are viable probes of the ICM's properties and the dynamical processes in galaxy clusters. In particular, radio relics can be used to infer the properties of magnetic fields and cosmic ray electron populations in the cluster outskirts. There is compelling evidence that radio relics trace galaxy cluster merger shocks. Therefore, it is proposed that the observed radio emission is the result of diffusive shock acceleration, a type of first-order Fermi acceleration, whereby charged particles gain energy by successively crossing a shock boundary.

The work presented in this thesis aims at putting constrains on the physics of the radio relic phenomenon. We pursue these objective by performing a joint comparison of radio relics mapped by sky surveys and radio relics that are modeled in large cosmological simulations. The structure of this work is as follows: In **this chapter** we give a brief review of our knowledge about galaxy clusters (Sec. 1.1) and of the radio relics found in these systems (Sec. 1.2). This will be followed in Sec. 1.2.4 by an outline of open questions about radio relics and the approach adopted here to answer them. In **Cha.** 2, we describe the procedure employed to build up a radio relic object catalog from the NRAO VLA Sky Survey (NVSS, Condon et al., 1998) in a cohesive manner. In **Cha.** 3, we describe our approach to create an equivalent mock sky survey from existing cosmological simulations. We apply this scheme on the Marenostrum-MultiDark SImulations of galaxy Clusters second simulation suite (MUSIC-2, Sembolini et al., 2013) cosmological simulation and compare it with the real sky survey. By introducing and applying the method of approximate Bayesian computation in **Cha.** 4, we constrain the parameters of our model and discuss their implications on the origin of radio relics.

1.1 Galaxy Clusters

Galaxy clusters are aggregations of dark matter, galaxies, and intermittent hot plasma (Fig. 1.1) with mass fractions of about 85 percent, 2 percent, and 13 percent, respectively. The formation of galaxy clusters is mainly driven by gravity. Starting from primordial density fluctuations, gravity amplifies the growth of the high-density peaks giving rise to present-day collapsed regions with densities several hundred times larger than the average density of the Universe. In dynamical equilibrium, i.e. with continuous accretion, the dark matter distribution evolves a characteristic profile with the density decreasing towards the cluster outskirts. There is no sharp boundary between a galaxy cluster and its surroundings. This fact is expressed in terms of the galaxy cluster region overdensity, i.e. a factor of Δ_c compared to the critical density ρ_c of the Universe. Typical overdensity values used are $\Delta_\mathrm{c} = 500, 200$, where the latter is used because it is similar to the density at which any volume becomes virialized, i.e. collapses within a ΛCMD cosmology. The radius R_{Δ_c} of the galaxy cluster is the radius of the spherical region in which the averaged density equals Δ_c times the

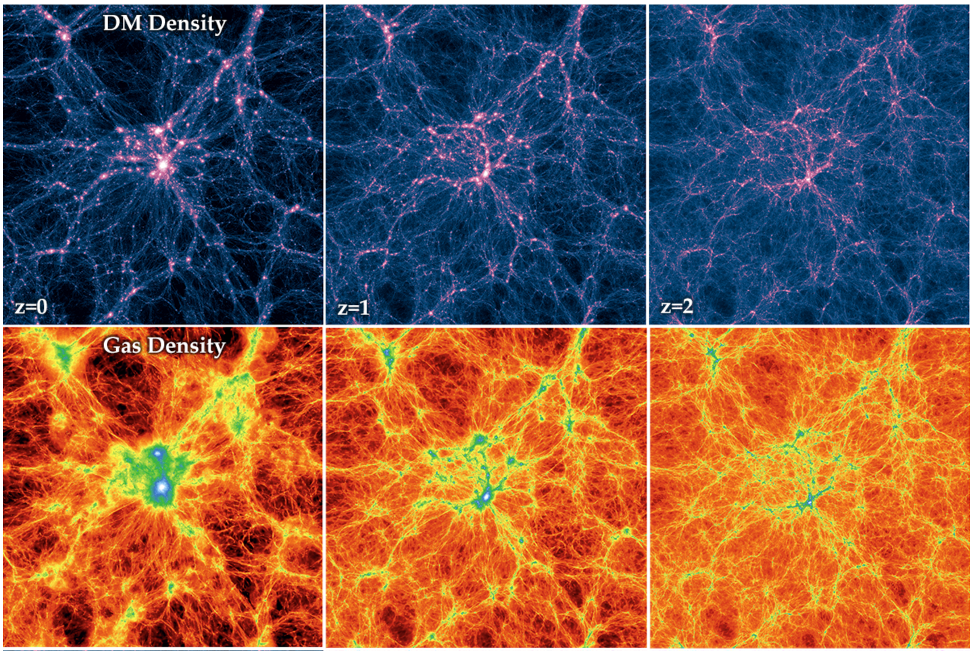

FIGURE 1.1: Redshift evolution of a slice through a simulated box of 106.5 Mpc comoving size (right to left), illustrating the spatial correlation of dark matter density (top) and plasma density (bottom). Adapted from the Illustris Simulation (Nelson et al., 2015)

critical density (White, 2001):

$$\overline{\rho_{\Delta_c}} = \Delta_c \rho_{\mathrm{c}} \,. \tag{1.1}$$

The most massive observed galaxy clusters have R_{200} of $2-3\,\mathrm{Mpc}$. The galaxy cluster mass within R_{Δ_c} is given by

$$M_{\Delta_c} = 4\pi \int_0^{R_{\Delta_c}} r^2 \rho(r)\,\mathrm{d}r \,. \tag{1.2}$$

Galaxy clusters grow with time through accretion of gas and mergers with other galaxy clusters. The growth of galaxy clusters is a hierarchical process. Under the assumptions of self-similarity and spherical collapse Press and Schechter (1974) derived a formalism for the gravitational growth of structures. It results in a prediction of the number density of clusters within a given mass-range, and was the first quantitative model to explain the mass distribution of galaxy clusters (comp. Fig. 1.2). The mass-function and their co-spatial distribution depend sensitively on the initial conditions of the Universe. This is why statistics based on galaxy cluster distributions are an excellent tool for precision cosmology (Abell, 1958; Bocquet et al., 2016; de Haan et al., 2016; Böhringer et al., 2017).

The first galaxy cluster catalogs were compiled through optical studies of galaxy

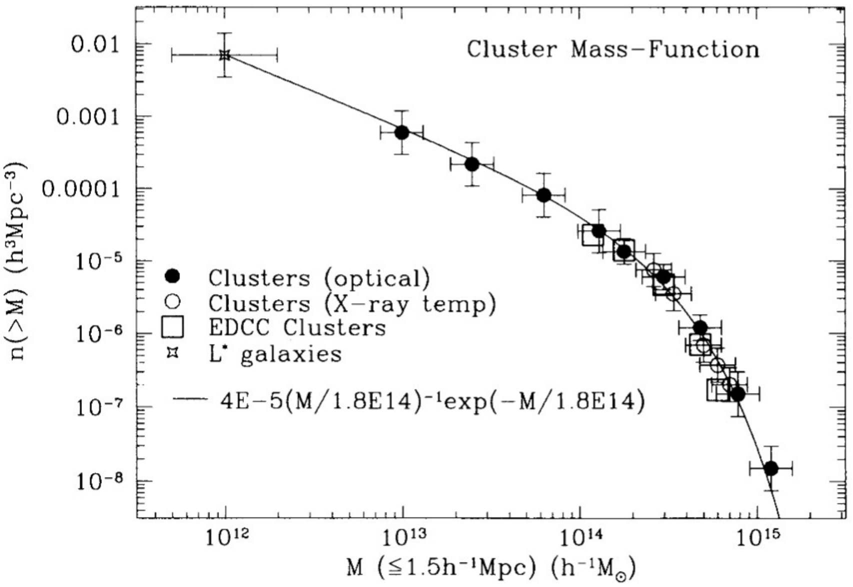

FIGURE 1.2: Mass function of galaxy clusters adapted from Bahcall and Cen (1993, Fig. 1). The sample is compiled from nearby galaxy clusters measured in optical and X-ray. The mass-spectrum forms a power law with exponential cutoff towards the high-mass end, as predicted by Press and Schechter (1974). The scaling variable h refers to reduced Hubble constant, $H_0/(70\,\mathrm{km}\,s^{-1}\,\mathrm{Mpc}^{-1})$.

clustering (Abell, 1958; Abell et al., 1989). Nowadays, the detection and study of galaxy clusters is supplemented by a number of other techniques. Further methods aim for detecting the galaxies that are part of clusters in infrared (Wylezalek et al., 2014) and radio studies (Daddi et al., 2017). Others probe the distribution of matter through weak lensing (Okabe and Smith, 2016). Another viable option is the detection of the diffuse plasma in-between cluster galaxies through X-ray observations (Giacconi et al., 1972; Böhringer et al., 2017), and by the thermal-Sunyaev-Zeldovic effect (Sehgal et al., 2013; Planck Collaboration et al., 2016), where electrons from the intermittent plasma up-scatter cosmic microwave background photons.

1.1.1 The intracluster medium

The intracluster medium (ICM) constitutes the baryonic matter permeating the galaxy cluster, i.e. not bound to any local structures like galaxies. Mergers of clusters, infalling clumps of matter (Zuhone and Markevitch, 2009), and central active galactic nuclei (AGNs, Yang and Reynolds, 2016) stir this medium. This kinetic energy is subsequently deposited into the ICM through the turbulent cascade and shocks.

As a result, the ICM is heated to temperatures of about 10^{7-8} K. Because of these high temperatures, galaxy clusters exhibit strong thermal bremsstrahlung which was first confirmed by the UHURU sky survey (Giacconi et al., 1972). The thermal bremsstrahlung of electrons scattered on positively charged nuclei in plasmas is also referred to as free-free emission. Its emissivity $\epsilon_{\rm ff}$ traces the electron number density $n_{\rm e}$ and kinetic temperature T of the ICM. For a thermal plasma with Solar elemental abundances, the bolometric bremsstrahlung emissivity is given by:

$$\epsilon_{\rm ff} \approx 3.0 \cdot 10^{-27} \left(\frac{n_{\rm e}}{1\,{\rm cm}^{-3}}\right)^2 \left(\frac{T}{1\,{\rm K}}\right)^{1/2} \,{\rm erg\,s^{-1}\,cm^{-3}} \tag{1.3}$$

with $n_{\rm e}$ ranging from $10^{-2}\,{\rm cm}^{-3}$ at the cluster core to $10^{-4}\,{\rm cm}^{-3}$ at a distance of R_{200}. The thermal bremsstrahlung makes the most massive galaxy clusters detectable as extended X-ray sources with integrated luminosities of $L_X \sim 10^{43-45}{\rm erg\,s^{-1}}$. This is why surveys with X-ray satellite proved to be very successful in detecting galaxy clusters. Thermal bremsstrahlung is the main cooling mechanism in galaxy clusters counteracting the heating due to the gravitational infall of matter and galactic outflows.

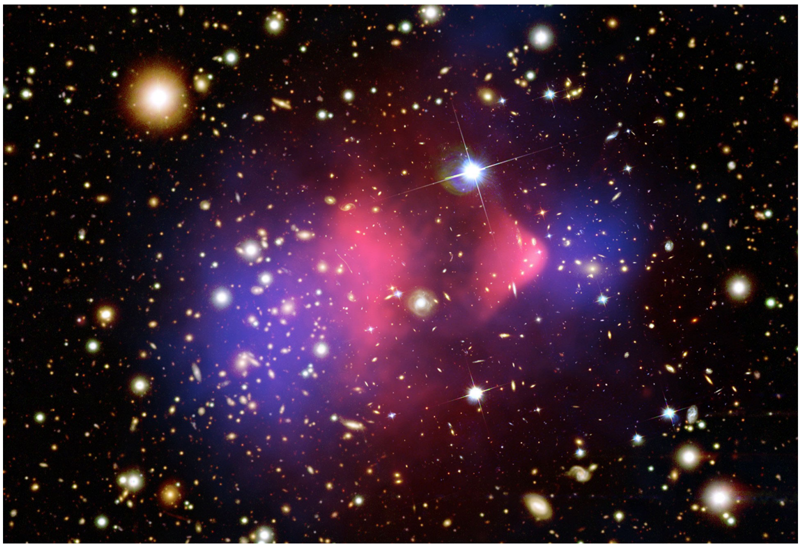

FIGURE 1.3: Composite image of the massive merging 'Bullet' cluster 1E 0657-558 depicting the X-rays emitted by hot gas (magenta, Chandra X-ray by Markevitch, 2006), and the suggested separated dark matter distribution (blue, Magellan optical weak lensing by Clowe et al., 2006). Added is a true-color Hubble observation.

The Coulomb mean free path λ_C of a thermal ion of temperature T in the ICM of density n is:

$$\lambda_C \approx 20\,{\rm kpc} \left(\frac{T}{10^8\,{\rm K}}\right)^2 \left(\frac{n}{10^{-3}{\rm cm}^{-3}}\right)^{-1} . \tag{1.4}$$

Below a scale of $\sim$ 20 kpc the ICM is foremost a *collisionless* plasma and its viscous behavior is not mediated through Coulomb interactions, but rather collective electromagnetic interactions (Sarazin, 1986; Brunetti and Lazarian, 2011).

Measures of the magnetic field strength in galaxy clusters are relatively sparse: Faraday Rotation Measures are used to estimate how the rotation angle of polarized emission changes when it travels through a magnetized medium. They can be used to infer the magnetic field strength of the medium between a source of polarized radio emission and the observer. Bonafede et al. (2010) used this technique to estimate the magnetic field strength in the ICM of the Coma cluster. These measures reveal field strengths of $0.1 - 1.0$ μG in the cluster outskirts and roughly 10 μG in the cluster center. This and other studies of this kind are consistent with a power-law density scaling of the magnetic field with an exponent of 0.4 to 0.7 (Govoni et al., 2017). This implies that the ratio of thermal to magnetic pressure

$$\beta_{\mathrm{P}} = \frac{p_{\mathrm{therm}}}{p_{\mathrm{mag}}} = \frac{n k_B T}{B^2/2\mu_0} \tag{1.5}$$

(k_B: Boltzmann constant, μ_0: vacuum permeability) is high in the ICM, i.e. larger around 10. We call this a high β-plasma (Marinacci et al., 2018, Sec. 3.1; Fig. 3). The implication is that its large-scale dynamic behavior can mostly be described by hydrodynamics which stands in contrast to the colder interstellar medium in galaxies (Marinacci et al., 2018). Interestingly, at smaller scales magneto-hydrodynamical phenomena become the governing factor.

Simulations by Vazza et al. (2017) show that based on the different possibilities of magnetogenesis the volume filling factor and power spectra of the magnetic fields can differ widely. The origin of the ICM's magnetic field is subject of active research but its genesis through a multi-staged process is likely. Starting with amplification through adiabatic compression, any primordial magnetic field is most likely superseded in galaxy clusters by magnetic seeding from active galactic nuclei (AGN)s (Hoyle, 1969), galactic winds (Yoel Rephaeli, 1988) or star formation (Pudritz and Silk, 1989). Additional amplification by a small-scale turbulent dynamo also likely occurs in the cluster environment (Vazza et al., 2014; Cho, 2014). Magnetic fields in galaxy clusters are not pristine, but rather the result of their formation process.

1.1.2 Cluster merger shocks

X-ray observations of galaxy clusters reveal two kinds of brightness discontinuities, i.e. shocks and cold fronts in the ICM. While cold fronts are zones in pressure equilibrium, a shock front is not. As shock fronts propagate at supersonic speeds they force a discontinuity of the hydrodynamic quantities like pressure, density, and temperature within the medium. We refer to regions before and after a shock front as up- and downstream, also as pre- and postshock, respectively.

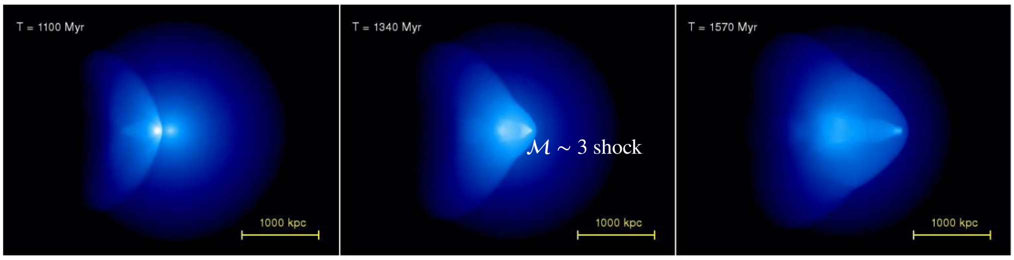

FIGURE 1.4: Simulation of the massive merging 'Bullet' cluster 1E 0657-558 showing the bolometric bremsstrahlung of the two sub-components of a mass ratio 10:1 at different times after both cluster components approaching their mutual virial radii $R_{\text{vir}} \sim 1.2\,R_{200}$. Jumps in the brightness map can be seen, which at the later stages correspond to $\mathcal{M} \sim 3$ shocks. The middle panel shows a snapshot that resemble observations of the actual system. Adapted from Springel and Farrar (2007).

The *Rankine-Hugoniot conditions* apply to shocks in the collisionless ICM in the same way as in their hydrodynamic counterparts (Landau and Lifshitz, 1959). The strength of the discontinuity or *jump* is governed by the Mach number

$$\mathcal{M} := v_{\text{shock}}/v_{\text{sound,upstream}} \tag{1.6}$$

i.e. the ratio of upstream flow velocity v_{shock} to the upstream speed of sound $v_{\text{sound,upstream}}$. Those conditions result in following relation for an oblique shock, with $\mathcal{M} > 1$, that expands into a homogeneous medium (a so-called *quasi-stationary shock*) with the adiabatic index $\Gamma = 5/3$:

$$\frac{P_2}{P_1} = 1 + \frac{5}{4}(\mathcal{M}^2 - 1)\,, \tag{1.7}$$

where P_1 is the preshock and P_2 the postshock pressure. Discontinuities also appear in density and temperature:

$$\frac{T_2}{T_1} = \frac{(5\mathcal{M}^2 - 1)(\mathcal{M}^2 + 3)}{16\mathcal{M}^2}, \tag{1.8}$$

$$\frac{\rho_2}{\rho_1} = \frac{\frac{8}{3}\mathcal{M}^2}{\frac{2}{3}\mathcal{M}^2 + 2} \overset{!}{=} C\,, \tag{1.9}$$

with the compression factor C approaching a value of four at strong shocks (Fig. 1.5), while temperature- and pressure-ratios scale by the square of the Mach number.

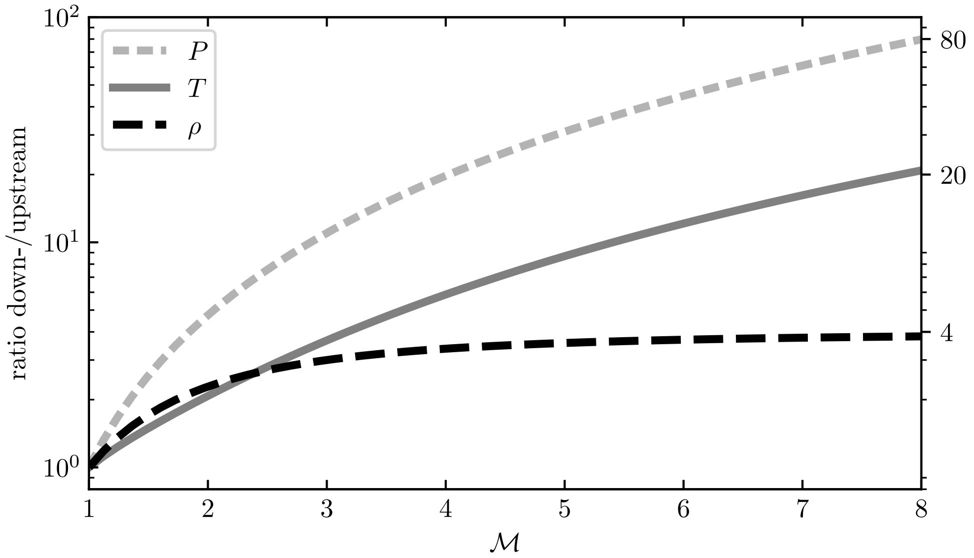

FIGURE 1.5: Shown are the ratio of pressure P, temperature T, and density ρ at a shock discontinuity due to the Rankine-Hugoniot equations (Eq. 1.7-1.9).

At galaxy cluster scales there are merger-, infall-, and accretion shocks (Zinger et al., 2018; Hurier et al., 2019). These are caused by the infall of galaxy clusters, groups and non-virialized gas, respectively. The former two reach bulk motions of $\sim 1500\,\mathrm{km/s}$ and can penetrate or disturb the cluster core. Accretion shocks are limited to the galaxy clusters' outskirts, where non-virialized gas first becomes shocked and compressed. The amount of gravitational energy dissipated during galaxy cluster mergers is a considerable fraction of the total bounding energy, which is of the order 10^{60} erg. The dissipated energy is channeled into the heating of the ICM (Ryu et al., 2003), magnetic field enhancement, and the acceleration of cosmic rays.

1.1.3 Cosmic ray electrons and their energetic losses

The fact that the ICM is a collisionless plasma at the scale of shock-physics means that particles can become accelerated through electromagnetic interactions before they are thermalized through collective damping (Longair, 2011, e.g.). The non-thermal components can be of highly-relativistic energies, at their extreme cosmic ray (CR) with Lorentz factors

$$\gamma_{\mathrm{CR}} = \sqrt{1 + \left(\frac{p}{mc}\right)^2} \gg 1 \tag{1.10}$$

where m is the rest mass. While CRs force an additional non-thermal pressure in the ICM, measures of profiles of hydrostatic masses and intracluster gas fraction suggest that the median non-thermal pressure is low compared to the thermal pressure (Eckert et al., 2019, of 6% and 10% at R_{500} and R_{200}, respectively).

Due to the Lorentz force, CR particles in the ICM follow a helical path along the field lines, with η being the *pitch angle* between the magnetic field vector $\mathbf{B}$ and the particle's velocity vector $\mathbf{v}$. While being under constant acceleration in a magnetic field those CRs emit synchrotron radiation within a cone of half-angle γ^{-1}. The synchrotron spectrum of a particle with charge q peaks close to the *critical angular frequency* ω_c (Condon and Ransom, 2019):

$$\omega_c = \frac{3\gamma^2 q B \sin\eta}{2mc} \quad \overset{q \doteq e,\, m \doteq m_\mathrm{e}}{\sim} \quad 26.4\,\mathrm{Hz}\frac{B}{1\,\mu\mathrm{G}}\gamma^2\,. \tag{1.11}$$

For frequencies much higher than $\omega_c/2\pi$, the synchrotron radiation is negligible. At radio frequencies of $\nu \sim 400\,\mathrm{MHz}$ and ICM magnetic field strength of $\sim\ \mu$G, electrons with $\gamma \sim 10^4$ are observed. Hence, radio astronomy provides information about high-energy cosmic ray electrons (CRes) in galaxy clusters.

The emitted bolometric synchrotron power $\dot{E}_\mathrm{syncr}$ of a CR particle depends quadratic on the local magnetic field strength, the rest mass, and even stronger on the Lorentz factor γ:

$$\dot{E}_\mathrm{syncr} \propto \frac{\gamma^3 (B \sin\eta)^2}{m^2}\,. \tag{1.12}$$

At radio frequencies accessible from the Earth's surface, the synchrotron emission of electrons dominates over the one from protons. Our further considerations will hence concern CR-electrons. When averaging over an isotropic distribution of pitch angles η the corresponding synchrotron emissivity gives

$$b_\mathrm{syncr,e} = \frac{\dot{E}_\mathrm{syncr,e}}{\gamma} \simeq 1.3 \cdot 10^{-21}\,\mathrm{s}^{-1} \cdot \gamma^2 \left(\frac{B^2}{1\,\mu\mathrm{G}}\right)\,. \tag{1.13}$$

A second energy loss mechanism for electrons within the ICM is the inverse Compton (IC) scattering - the very same mechanism that is responsible for the thermal-Sunyaev-Zeldovic effect. Cosmic microwave background (CMB) photons are scattered to higher energies at the ICM electrons. This results in an energetic loss of the ICM electrons of the power:

$$\dot{E}_\mathrm{IC} \propto \gamma^3 U_\mathrm{CMB}\,. \tag{1.14}$$

Because both synchrotron and inverse Compton losses have the same dependency on γ, one can treat the energy density U_{CMB} as a redshift-dependent equivalence magnetic field strength B_{CMB} (Klein and Fletcher, 2014)[1]:

$$B_{\mathrm{CMB}} = 3.25 \cdot (1+z)^2 \ \mu\mathrm{G}\,. \tag{1.15}$$

If only these two losses were present, low-energy CRes would accumulate within the ICM. However at $\gamma \lesssim 100$ energy losses due to the mentioned thermal bremsstrahlung become more relevant. In addition, losses due to Coulomb scattering become important (Y. Rephaeli, 1979). The latter is density dependent and becomes the major energetic loss for intermediate γ at electron densities above $10^{-5}\mathrm{cm}^{-1}$:

$$\dot{E}_{\mathrm{Coulomb}} \propto \gamma^2 n_{\mathrm{e}}\,. \tag{1.16}$$

The characteristic emissivity is:

$$b_{\mathrm{Coloumb}} = 1.21 \cdot 10^{-12}\,\mathrm{s}^{-1} \frac{n_{\mathrm{e}}}{1\mathrm{cm}^{-3}} \left[1.0822 + 0.0119 \,\ln\left(\frac{\gamma}{n_{\mathrm{e}}/\mathrm{cm}^{-3}}\right)\right]\,. \tag{1.17}$$

At a constant injection rate of CRes the equilibrium energy distribution will be shifted towards lower energies in a denser medium. The characteristic lifetime τ of a CR particle due to all these combined losses can be computed as:

$$\tau = E_{\mathrm{kin}}/\dot{E} \tag{1.18}$$

$$\tau_{\mathrm{e,ICM}} = \frac{(\gamma-1)m_{\mathrm{e}}c^2}{\dot{E}_{\mathrm{syncr}} + \dot{E}_{\mathrm{IC}} + \dot{E}_{\mathrm{Coloumb}}}\,. \tag{1.19}$$

with E_{kin} being the (relativistic) kinetic energy. The combined effect of these energetic losses is called *particle aging*. Fig. 1.6 shows that since $z \lesssim 0.8$ electrons that lost most of their energy through synchrotron or inverse Compton cooling can accumulate in the cluster outskirts as their loss-timescale becomes comparable to the typical occurrence time of major merger events, ie. several Gyr.

Whilst the radiative losses of CR protons in the ICM are far from any detection, the synchrotron emission of CRes is detected in the form of so-called *diffuse radio emission*. This type of emission is a volume filling type of synchrotron radiation that permeates the ICM (Feretti et al., 2012). There are four different classes of diffuse radio emission detected in galaxy clusters of diverse dynamic states: giant radio relics, radio phoenices, giant radio halos, and radio mini halos (van Weeren et al., 2019).

---

[1] Taken from shortly before equation 2.43 Klein and Fletcher, 2014

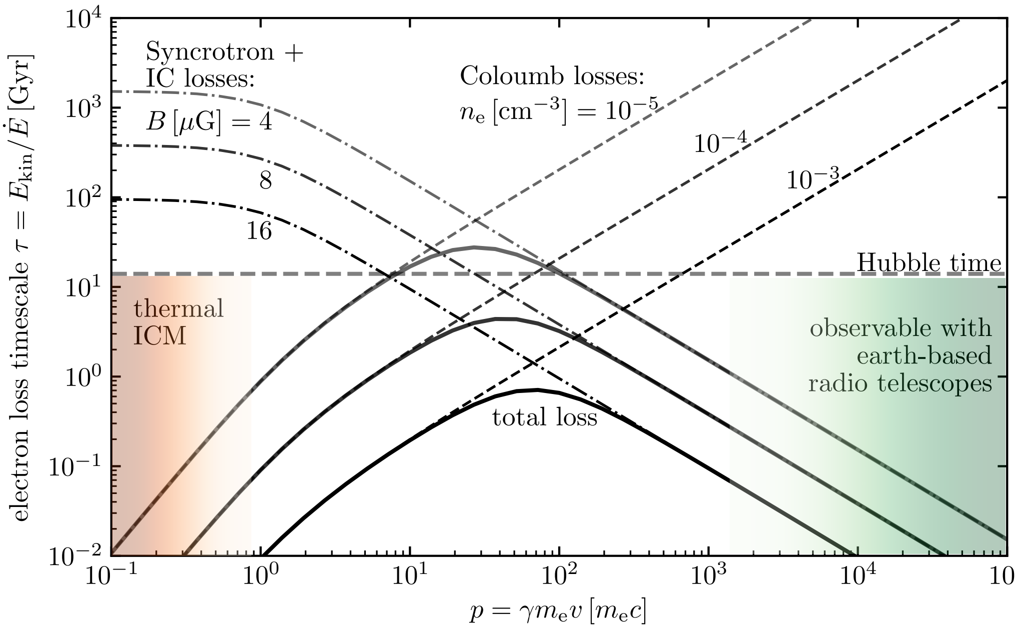

FIGURE 1.6: Cooling time of CRes for typical conditions in the ICM plotted of their relativistic impulse. The chosen magnetic fields are similar B_{CMB} at $z = 0.1$, 0.6, and 1.2. Electrons with a Lorentz-factor of $\gamma \sim 30$ can reach a characteristic lifetime larger than the Hubble time if injected in cluster outskirts ($n_e \sim 10^{-5}\,\mathrm{cm}^{-3}$) with magnetic fields of $\sim 4\,\mu$G. Adapted from EnSSlin et al. (2011)

All classes of diffuse emission share the so-called *diffusion problem*: the size of observed structures and the relatively short timescales at which this CRes age, are incompatible with local acceleration and diffusion across the cluster volume (comp. Fig. 1.6). However, one possible for the non-locality is a connection with dynamical processes in galaxy clusters that are coherent on scales $\gtrsim 100\,\mathrm{kpc}$ (Ensslin et al., 1998; EnSSlin et al., 2011).

1.2 Giant Radio Relics

Giant radio relics, also referred to as *radio gischt* or *(cluster) radio shocks*, are synchrotron emission sites found in downstream regions of galaxy cluster shocks. The synchrotron emission stems from CRes. At those high high-energy levels, the CRes must have been accelerated within the last dozen of million of years. The leading hypotheses is that this (re-)acceleration occurs at the shock fronts produced in galaxy cluster mergers (Ensslin et al., 1998; van Weeren et al., 2019). In particular, radio gischt *shares* a set of observational properties (Feretti et al., 2012, also Fig. 1.7):

(1) They are found in massive galaxy cluster that show signs of merging activities. There is strong evidence that this gischt traces shock fronts based on numerous detections of temperature-discontinuities equivalent to $\mathcal{M} = 2 - 4$ shocks at radio relics (e.g. Finoguenov et al., 2010).

(2) Within the GHz-regime the flux density $F(\nu)$ of most radio relics exhibit a power-law-like integrated spectrum of their flux density

$$F(\nu) = F_0 \left(\frac{\nu}{\nu_0} \right)^{\alpha}, \tag{1.20}$$

with F_0 as reference flux density at the frequency ν_0 and with the integrated spectral index $\alpha_{\text{int}} \lesssim -1$.

(3) They are elongated and concavely bent towards the cluster center. The spectrum is flattest at the outer edge of the relic with $\alpha_{\text{inj}} \approx \alpha_{\text{int}} + 0.5$ (comp. Eq. 1.23) and steepens gradually towards the cluster center.

(4) The emission is strongly linearly polarized, with the B-vectors parallel aligned to the *shock surface* and fractional polarizations up to 40 percent at frequencies $5 - 10\,\text{GHz}$ (Kierdorf et al., 2017; Loi et al., 2017).

Originally, Kempner et al. (2004) introduced the convention that first differentiated between radio *gischt* and *phoenices*. Radio phoenices, in contrast to radio gischt, have a spectrum steeper than $\alpha_{\text{int}} < -1.7$ which bends downwards at higher frequencies. In general, they also have a smaller size of around 100 kpc and tend to be located closer to the center of the cluster (Feretti et al., 2012). It is reasonable to assume that those common properties provide insights about the formation mechanism of these structures. The leading hypotheses for the existence of *phoenices* is that they are the result of shock compression and re-energization of aged plasma which got expelled from AGNs (van Weeren et al., 2019). Sometimes aged plasma is detected in the form of so-called *AGN relics*, which are considered potential precursors of radio phoenices.

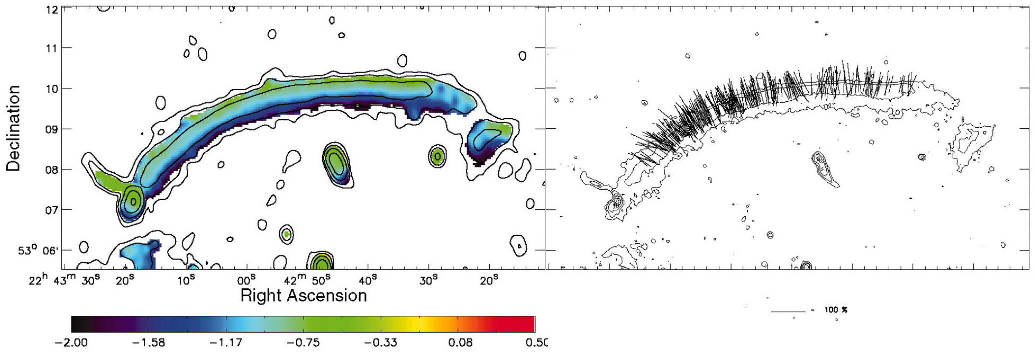

FIGURE 1.7: The Sausage relic in CIZA J2242.8+5301 exhibits spectral steepening towards the cluster center (*left*) and has aligned linear polarization vectors (*right*, perpendicular to the magnetic field vectors). Both properties are typical for giant radio relics. Adapted from van Weeren et al. (2010)

Conversely, *gischt* is supposed to stem from FERMI-I type acceleration of electrons at merger shocks (see Sec. 1.2.1).

Some merging galaxy clusters host relics on opposing sides of the cluster. These objects are called *double relics*. Both simulations and the mass distribution in galaxy clusters suggest that double relics may occur when two clusters of comparable mass merge with a low impact parameters and are observed edge-on, i.e. with the merger axis being orthogonal to our observers perspective (Roettiger et al., 1999).

Observations of radio relics with X-ray telescopes suggest that the acceleration of electrons to CR-energies occurs close to the shock discontinuity (van Weeren et al., 2019). Under the assumption that the synchrotron emission of radio relics stems from a CR population aging downstream a quasi-stationary shock Hoeft and Brüggen (2007) derived a closed expression of the width of the radial synchrotron profile at which the flux density decreased to 30 percent of the peak flux density. For relics with $\mathcal{M} \sim 3$ the maximum possible width (reached for a magnetic fields around $2\,\mu$G):

$$\Delta l_{\mathrm{cool,max}} \sim 50\,\mathrm{kpc} \left(\frac{\nu_{\mathrm{obs}}(1+z)}{1.4\,\mathrm{GHz}} \right)^{-1} \tag{1.21}$$

and roughly inverse-proportional the observing frequency. While we can resolve the downstream structure of radio relics with present day radio telescopes the downstream structure of the shock with a scale of few kpc will remain ellusive until the next generation of X-ray telescopes (Markevitch, 2006; Mushotzky et al., 2019).

Understanding the acceleration mechanism in radio relics requires information about the present CR population, its history and the magnetic fields in the outskirts of galaxy clusters. In the next four subsections we discuss further insights on the CR population starting with the diffusive shock acceleration (DSA) mechanism, which is one of the main drivers of CR-acceleration in astrophysical shocks.

1.2.1 Diffusive shock acceleration

Diffusive shock acceleration (DSA) is a first-order Fermi acceleration process. DSA already was identified as a key mechanism for the CR generation in supernova remnant shock shells (Lagage and Cesarsky, 1983; Lee et al., 2012), solar flares, and in Rayleigh-Taylor instability regions of highly relativistic extragalactic jets. In the DSA-process charged particles gain energy by successively traveling across the shock boundary (Fig. 1.8) until they reach the highly-relativistic energies typical of CRs (Blandford and Eichler, 1987; Baring, 1997). This mechanism requires that the particles have large-enough Larmor radii for the shock to be considered as an infinitely thin boundary separating two regions of different plasma properties. Consequently, this mechanism is only efficient for particles of sufficiently high energies, i.e. several GeV. While for many astrophysical phenomena this requires an existing population

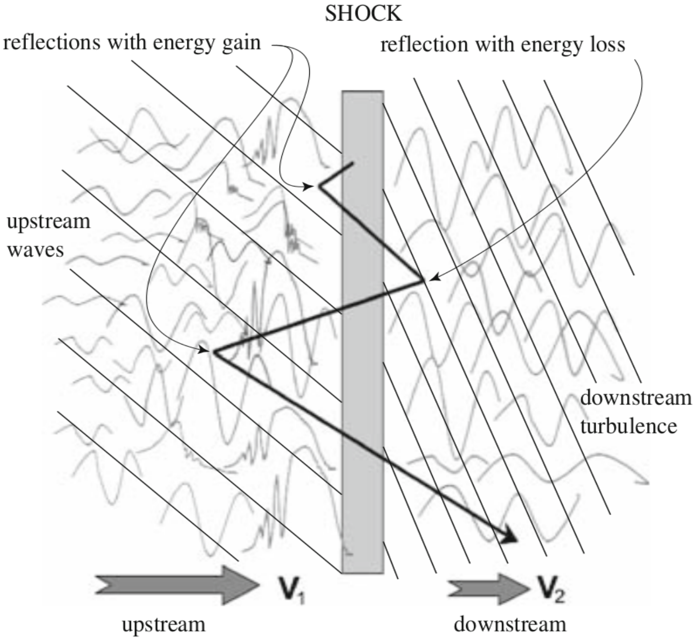

FIGURE 1.8: A sketch of the DSA mechanism taken from Treumann (2009, Fig. 43): An energetic particle gets injected from the shock to the upstream medium. With a certain chance the particle is scattered back from waves. Under these circumstance upstream and downstream waves act as approaching magnetic mirrors. Reflection on impeding upstream waves gives the particle more energy than it loses by being reflected at downstream waves. The particles energy increases successively proportional to the velocity of the shock v_s (first-order) until it escapes from the shock to free space as a CR.

of pre-accelerated electrons, Ensslin et al. (1998) and Miniati et al. (2001) proposed that the high-energy tail of thermalized gas in galaxy clusters could yield electrons of sufficiently high energies to trigger DSA at cluster merger shocks.

Attempts to draw stringent conclusions on the latter are, however, not free of difficulties: Simulations of the DSA process of both electron and proton population are computational unfeasible and limited to extrapolations. Scales involved range from the electron gyroradius up to to several hundreds of proton gyroradii.As an approximation to the problem, several groups have worked on semi-analytical solutions for the DSA mechanism at $\mathcal{M} < 10$ shocks within the ICM (Hoeft and Brüggen, 2007; Kang et al., 2012).

If DSA is efficient enough, it will result in a power-law CR electron population in momentum space. In this case, the injection index directly after the shock, α_{inj}, is tied to the initial exponent p_{inj} of the momentum distribution $f(p)$ of the accelerated electrons:

$$\alpha_{\mathrm{inj}} = \frac{p_{\mathrm{inj}} + 1}{2} \quad \text{with} \quad p_{\mathrm{inj}} = 2\frac{1 + \mathcal{M}^2}{1 - \mathcal{M}^2} < -2\,. \tag{1.22}$$

For a quasi-stationary shock, i.e. a shock that expands into a homogeneous medium, the integrated downstream flux density will follow a power-law with spectral index

$$\alpha_{\mathrm{int}} = a_{\mathrm{inj}} - \frac{1}{2}, \tag{1.23}$$

which conforms to the observations of radio relics (Eq. 1.20). The resulting radio structures will resemble radio relics in their aforementioned key features.

If DSA is performed on thermal ICM electrons then only shocks $\mathcal{M} > 2.5$ are efficient at accelerating electrons (Fig. 1.9), implying that there should be no radio relics at weak shocks if thermal-pool DSA is the single mechanism at work in merger shocks. However, several cases of radio relics are known that have an integrated spectral index $\alpha_{\mathrm{int}} < -1.4$, corresponding to Mach numbers smaller than 2.5 (e.g. A1682 NW). They provide evidence for additional acceleration mechanisms at work in the ICM or the existence of a non-thermal population of electrons that contributes to DSA.

The details of the plasma processes in the ICM - considered as micro-physics at the scale of galaxy clusters - are largely unknown and additional pathways for particle acceleration do exist (Brunetti and Jones, 2014). For instance, shock drift acceleration (SDA) is supposed to work efficiently on low Mach number shocks and lower energetic electrons (Guo et al., 2014a; Guo et al., 2014b). Because of this, SDA could have a significant impact as a pre-acceleration path for DSA in galaxy clusters.

One finding by Guo et al. (2014a) that makes a joint contribution of SDA and DSA likely is that SDA strongly favors the acceleration of electrons over protons. Hence, SDA relaxes the tension on the detection of low Mach number relics (Sec. 1.2.2) and the non-detection of CR-protons in galaxy cluster cores (Ackermann et al., 2016).

1.2.2 Pre-existing cosmic ray electrons

Once electrons are accelerated to ultra-relativistic energies they age, i.e. lose their energy by inverse-Compton and synchrotron losses. If they remain with energies well above their rest-mass energy ($m_e c^2 = 0.511\,\mathrm{MeV}$) they can become more easily injected into the DSA process. This concept is referred as *re-acceleration* of *pre-existing CR electrons*. A possible prevalence of pre-existing CRes in present-day galaxy clusters arises from a local minimum of aging at a Lorenz-factor of a few (Fig. 1.6). Arguments in favor of pre-existing CRes are energetic requirements, the discovery of low Mach numbers relics, and possible physical connections of relics with AGNs:

- Colafrancesco et al. (2017) argue that the absence of any correlation between radio power and Mach number in radio relic statistics indicates that the radio relic properties are mainly governed by pre-existing CR electron populations.
- Kang et al. (2012) and Vazza and Brüggen (2014) argue that there is evidence for pre-existing CRes based on the brightness profile and total brightness of certain radio relics. Kang (2017) further elaborate on the case of the 'Sausage' relic by assuming pre-existing electrons and post shock turbulence.
- Shimwell et al. (2015) suggest that the compact region accounting for 98 percent of the radio emission in the radio relics of the *Bullet cluster* might be due to the prevalence of fossil plasma which didn't had time to diffuse further.
- Simulations by Pinzke et al. (2013) show that depending on the cooling history pre-existing CRes can influence the DSA efficiency in the $> 0.8 R_{200}$ outskirts of a galaxy cluster. They also derive predictions for the emission of relics of varying shock strength (see Fig.1.9) under the existence of a pre-existing electron population. Their findings strongly support the idea of pre-existing CRes for radio relic emission found at $\mathcal{M} \lesssim 3$ shocks.
- Macario et al. (2011) find an $\alpha_{\mathrm{int}} \sim -1.9$ radio structure close to an X-ray detected cluster shock, suggesting a radio relic at a shock, that is too weak for DSA acceleration from the thermal pool to be responsible.

- Based on a relic-AGN connection Bonafede et al. (2014) claim that there is evidence for electron re-acceleration in the radio relic of the galaxy cluster PLCKG287.0+32.9 based on their spatial co-occurrence and a flattening of the relic spectral index towards the AGN. van Weeren et al. (2017) follow the same line of reasoning for the southern relic of the galaxy cluster Abell 3411.

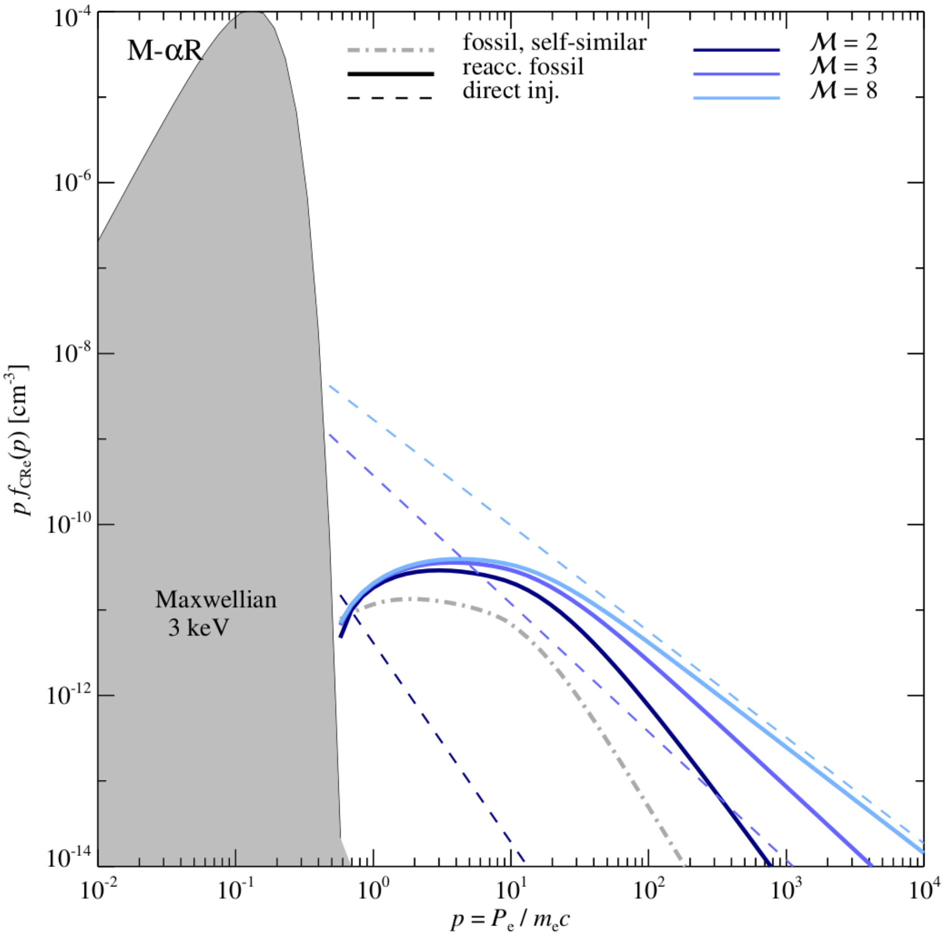

FIGURE 1.9: Comparison of a DSA accelerated electron spectra from the thermal pool and pre-existing mildly relativistic CRes (Pinzke et al., 2013): While the spectral slope resulting from the acceleration is identical for both cases the effective normalization is not. The normalization of high-energetic CRes that stem from DSA on pre-existing CRes is less dependent on the Mach number than in the case of DSA on the thermal pool. Especially for $\mathcal{M} \leq 3$, depending on their prevalence, pre-existing CRes can yield a larger accelerated electron population than thermal pool electrons.

Studies *by how much* this pre-existing population of CRes influence the generation of radio relics are only at their beginning. It is also unclear if the CR electron population in galaxy clusters is volume-filling and prevalent or relatively local or transient.

1.2.3 On the Mach number measurements

A comparison of the Mach numbers obtained through X-ray profiles and through integrated spectra of radio observations reveal mismatches van Weeren et al. (2019): It has been found that the estimates derived by means of the X-ray profile of galaxy clusters are systematically lower than the ones derived from the integrated spectral index of the synchrotron emission. Skillman et al. (2013) performed cosmological magneto-hydrodynamic simulations of merging galaxy clusters. According to them, the projection of shocks with different Mach numbers within one relic can also mimic aging. Hong et al. (2015) also performed simulations in which they point out the importance of the shock surface associated to relics, consisting of multiple shocks with different Mach numbers. If the DSA efficiency has a strong dependency on the Mach number of the shock then Mach numbers derived from synchrotron emission could be biased towards stronger shock regions. In this respect, a significant tension is posed by the northern relic in galaxy cluster 1RXS J0603.3+4214 (Itahana et al., 2015) where an X-ray inferred temperature-jump suggest a Mach number of $\simeq$ 1.5, while investigations of the radio emission suggest $\simeq$ 4.0 (Rajpurohit et al., 2018).

1.2.4 Population statistics of radio relics

Uncertainties about the process that leads to the observed population of radio relics include magnetic fields in galaxy clusters (Sec. 1.1.1), particle acceleration processes (Sec. 1.2.1), and the local population of non-thermal particles (Sec. 1.2.2). In addition, the retrieval of some of the properties that determine the particle acceleration, like the Mach number(s) of the shock, are also subject of systematic uncertainties (Sec. 1.2.3).

Most of the tools used to generate synthetic radio relic populations rely on the analysis of simulations of cosmological plasmas. Those simulations range from Particle-in-Cell Simulations aiming to answer details about particle acceleration in the ICM (Guo et al., 2014a), to the attempt to reproduce observed relic properties by simulating merging galaxy clusters (Skillman et al., 2013), and to the simulation of galaxy cluster ensembles in order to analyze them on their general synchrotron emission properties (Hoeft et al., 2008; Vazza et al., 2012; Nuza et al., 2012; Hong et al., 2015; de Gasperin et al., 2014; Nuza et al., 2017).

All of those techniques belong to the family of forward-modeling techniques (Fig. 1.10). Forward-modeling occurs when a model M is used as a generator for data D (Press and Schechter, 1974; Marzke, 1998) – which can be further processed to mimic observations or experiments. Backward-modeling starts from the observable and aims at inferring the underlying model parameters $\boldsymbol{\theta}$. Both methods can be used jointly. One could imagine a quantity that is neither fully physical nor a real observable, but that is a useful discriminator between theory and observation (Fig. 1.10). These quantities can be summary statistics, coefficients of a reconstructed signal, and/or other variables that describe the structure of the data. When faced with complex models and observations it is worth to use advanced statistical methods to increase the precision or lower the bias of the conclusions.

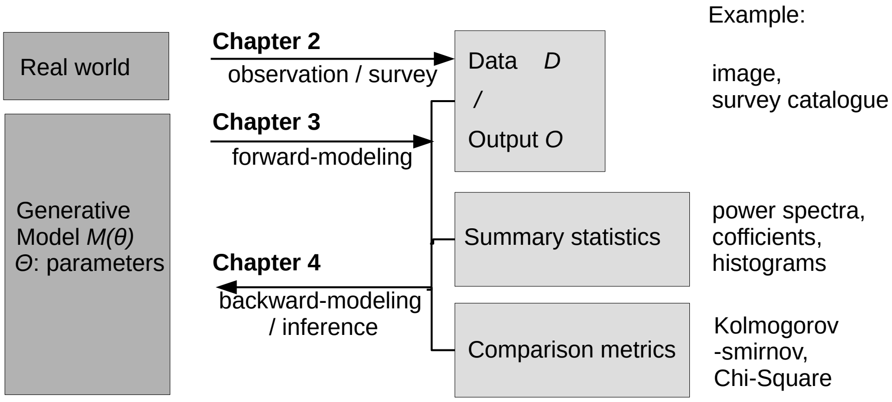

FIGURE 1.10: Shown is the methodology of this thesis used to perform parameter inference on the ICM processes through the radio relic population statistics.

One particular challenge of backward-modeling is posed by sky surveys of astrophysical objects. While they in principle contain information about the physical processes of interest, they also include a large number of nuisance parameters, i.e. factors that are needed to take into account to explain observations, but which do not belong to the physical problem itself. When simulating radio relics one significant complication is the complexity of galaxy cluster growth history and resulting uncertainties about shock fronts in the ICM. Several publications acknowledge the value of using ensembles of simulations to better manage the intrinsic stochasticity of galaxy cluster mergers in the cosmological context.

The main innovation in this work will be to leverage a consistent strategy to derive the observed and simulated sample of radio relics to perform model parameter inference. Specifically, we will use forward-modeling techniques in the form of mock sky surveys for the inference of radio relic model parameters. Here, we present, for the first time, a likelihood-free parameter inference on the physics of CR electron acceleration in galaxy clusters. Applying this approach to the population statistics of radio relics will allow for inferences on the magnetic field strength, the acceleration processes, and the amount of pre-existing CRes in the ICM.

Chapter 2

The NVSS sample of radio relics

If radio relics are observed in a uniform manner, one can reasonably simplify the process that leads from physical quantities to radio images. Surface brightness limited sky surveys are ideal in that regards as they simplify the understanding of the radio map generation (Carassou et al., 2017). Whilst the trade-off is less recovered relics than are actually known from targeted observations, the advantage of such an approach is a deep understanding of the data generation process.

Radio relics are foremost detected and described at frequencies from 0.1 to 2 GHz. Most of the imaging of those extragalactic radio sources is accomplished by aperture synthesis of radio interferometers. In Sec. 2.1 we describe some of the key characteristics of this method. This motivates Sec. 2.2, where we give a brief overview on corresponding sky surveys which mapped a large number of radio relics. The NRAO VLA Sky Survey (NVSS, Condon et al., 1998) delivers both large survey area and sensitivity for extended emission at 1.4 GHz. It hence successfully recovers the sample of known radio relics in the range of $z \sim 0.05 - 0.60$. This is why we choose NVSS as the main source of our study. In Sec. 2.3 we describe the sample of radio relics in NVSS and highlight some of its summary statistics that find use throughout this work. We assume a flat universe, specifically the ΛCDM cosmology with matter density fraction $\Omega_{\mathrm{M}} = 0.27$, cosmological constant fraction $\Omega_{\Lambda} = 0.73$ and Hubble constant $H_0 = 70\,\mathrm{km s^{-1}\,Mpc^{-1}}$.

2.1 Imaging radio relics with interferometers

Most investigations of radio relics are performed through radio interferometers. Radio interferometers are arrays of receivers that allows one to record the inference patterns of radio signals. The primary motivation is to achieve a much higher angular resolution than for each single element. Radio interferometers can provide the resolution which is needed to determine the fundamental properties of radio relics (Sec. 1.2) and discern them from other sources, most notably AGNs.

Each receiver pair (i,j) provides a baseline of length $b_{i,j}$ which sample spatial frequencies of the sky brightness distribution. The sampling of the spatial frequencies with aperture arrays is sparse. If only an instantaneous observation is performed, we call this a *snapshot* observation. If observations are taken over a considerable fraction of the Earth's rotation period, one and the same baselines can gather information about *an ellipse of positions* in the Fourier-space. This so-called *earth-rotation synthesis* increases the coverage in the Fourier space of the sky brightness distribution and allows a better reconstruction of the sky brightness distribution. Because of this, there is not a single, but a manifold of models of the sky brightness distribution that can explain the data. A model of the sky brightness distribution has to be inferred through iterative reconstruction algorithms. This procedure requires a considerable amount of computing resources and expertise.

The highest achievable angular resolution of a radio interferometer is given by the ratio of the observing wavelength $\lambda_{\rm obs}$ (corresponding observing frequency $\nu_{\rm obs}$) to the length of the longest baseline $b_{\rm max}$:

$$\Theta_{\rm min} = 5.39'' \left(\frac{\nu_{\rm obs}}{1.4\,{\rm GHz}}\right)^{-1} \left(\frac{b_{\rm max}}{10\,{\rm km}}\right)^{-1} = 1.22' \,\frac{\lambda_{\rm obs}}{b_{\rm max}}\,. \tag{2.1}$$

For the image reconstruction process one prefers to use a so-called *restoring beam* of Gaussian shape with a $\Theta_{\rm FWHM}$ of 1.177 times this value. The array's shortest baseline $b_{\rm min}$ sets a similar scale:

$$\Theta_{\rm max} = 8.98' \left(\frac{\nu_{\rm obs}}{1.4\,{\rm GHz}}\right)^{-1} \left(\frac{b_{\rm min}}{100\,{\rm m}}\right)^{-1} = 4.19' \left(\frac{b_{\rm min}}{{\rm k}\lambda_{\rm obs}}\right)^{-1} \tag{2.2}$$

above which structures will be imaged with an increasing loss of flux density. Snapshot observations, provide a limited sampling of the largest angular scales. At snapshot observations, hence, flux loss already occurs at a scale smaller than the theoretical $\Theta_{\rm max}$. For the arrays considered within this work snapshot observations reduce the effective $\Theta_{\rm max}$ by roughly 50 percent compared to a full *rotation synthesis* observation (Farnsworth et al., 2013). The image noise under best circumstances is spatially uncorrelated and shows a Gaussian power distribution, which is why we express it in units of root means square (rms) variance. Because interferometer images of radio relics are always reconstructions, their resolution is not fixed but chosen in an attempt to maximize the interpretability of the image by balancing resolution $\Theta_{\rm FWHM}$ and noise variance $\sigma_{\rm rms}$. The sky surveys of interest by default have a resolution that is optimized for resolved point-sources. Starting from this resolution, the increase of the rms noise with the beam full width half maximum (FWHM) will be proportional at best:

$$\sigma_{\mathrm{rms}} \propto \Theta_{\mathrm{FWHM}}^{1.0} \tag{2.3}$$

but depending on the array setup and image reconstruction will have a scaling-exponent > 1.0. Lowering the image resolution *can* increase the signal/noise ratio of an extended object, like a radio relic. The general behavior is exemplified in Fig. 2.1 where we show how the resolution can influence the measurements of size and flux of a radio relic. In general, the best signal/noise ratio is reached, if the resolution equals the size of the extended structure.

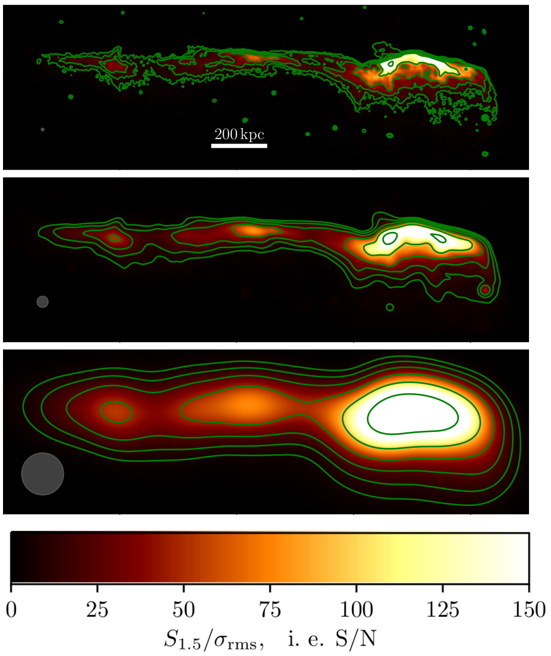

FIGURE 2.1: Shown is a flux density $S_{1.5}$ map of the bright northern relic in 1RXS J06+42 at 1.5 GHz central frequency masked and imaged at resolutions of 3 **(left)**, 12 **(middle)**, and 45 **(bottom)** arcseconds FWHM resulting from a deep observation with the Expanded Very Large Array (eVLA) . Contours start from 6 σ_{rms} and increase by multiples of two. σ_{rms} is the average rms flux of the measured background being in order of deceasing resolution 4.0 μJy/beam, 28 μJy/beam, and 180 μJy/beam. This suggests a scaling of the σ_{rms} with $\Theta_{\mathrm{FWHM}}^{1.4}$. The beam-size is shown by a circle in the lower left corner of each image. Data courtesy of Rajpurohit, K.)

2.2 Radio interferometric surveys of radio relics

Radio relics are faint and rare objects. Because of this the sensitivity for extended structures and the covered area are the most crucial survey parameters. There is a large number of radio surveys in which radio relics are present (comp. Tab. 2.1 and Fig. 2.2).

The NRAO VLA Sky Survey (NVSS, Condon et al., 1998) mapped the sky above -40 degree declination with the Very Large Array (VLA) telescope at 1.4 GHz. The fractional sky coverage of NVSS is remarkably high with 82%. NVSS was designed to yield a high sensitivity for objects extending to angular scales up to $\sim 10'$. The

TABLE 2.1: Compilation of large radio sky surveys of the last decades and upcoming years. It is a selection of surveys with possible use for this work and follow-up studies. Surveys marked with ⧖ are yet to be fully released. Shown are the survey name, the sensitivity of at the highest resolution, FWHM of the beam due to Eq. 2.1, and largest imagable scale Θ_{max} due to Eq. 2.2. The ^{s} label denotes snapshot observations in which case Θ_{max} was scaled down by a factor of 0.5. The survey coverage f_{sc} is given in fractions of an all-sky survey with 41,253 deg^2 coverage.

Survey	σ_{rms} mJy/beam	$\nu_{\text{obs,cen}}$ MHz	Θ_{FWHM} arcsec	Θ_{max} arcmin	f_{sc}	Reference
NVSS	0.45	1400	45	8^s	.82	Condon et al. (1998)
FIRST	0.15	1400	5	1^s	.26	Becker et al. (1995)
TGSS ADR	4	148	25	9^s	.89	Intema et al. (2017)
GLEAM	10	150	100	430^s	.75	Hurley-Walker et al. (2017)
MSSS-HBA	5	144	120	46^s	.50	Heald et al. (2015)
⧖ MSSS-LBA	15	52	150	127^s	.50	Heald et al. (2015)
⧖ LoTSS	0.1	144	5	92	.50	Shimwell et al. (2017)
⧖ EMU	0.01	1280	10	24	.85	Norris et al. (2011)
⧖ WODAN	0.01	1280	15	12	.49	Röttgering et al. (2011)

average rms of the surface brightness fluctuations $\sigma_{\text{rms,NVSS}}$ is 0.45 mJy beam^{-1}. As relics tend to be faint at GHz frequencies compared to the predominant radio galaxies, a proper identification and subtraction of other nearby sources is paramount. NVSS provides a restoring beam of $45''$ FWHM which translates into a physical scale of 80, 150 and 244 kpc for $z = 0.1$, 0.2 and 0.4, respectively. Because this resolution is not always sufficient to identify most of the AGN sources - we make further use of auxiliary data (Sec. 2.3.2). Existing high resolution observations of our targets are quite plentiful at 1.4 GHz because of the VLAs A-configuration. Faint Images of the Radio Sky at Twenty-cm (FIRST, Becker et al., 1995), for example, is not a survey for extended objects itself, but because of its high resolution is often used to help identifying compact sources.

The alternative data release of TIFR GMRT Sky Survey (TGSS ADR1, Intema et al., 2017) shows a similar sky coverage and sensitivity for resolved objects with a spectral index of $\alpha = -1.3$ (de Gasperin et al., 2018). This allowed de Gasperin et al. (2018) to create a spectral index catalog based on NVSS and TIFR GMRT Sky Survey (TGSS). However, due to the use of the calibration scheme SPAM (Intema et al., 2009; Intema, 2014) the TGSS ADR1 it is less sensitive to faint and extended objects which applies to a large fraction of known radio relics (Fig. 2.3).

Both frequency bands of the Multifrequency Snapshot Sky Survey (MSSS, Heald et al., 2015) are the first attempt of utilizing the survey capabilities of the Low Frequency Array (LOFAR), which comprise high resolution images at low frequencies with good sensitivity for extended structures. Eventually, they will be succeeded by the LOFAR

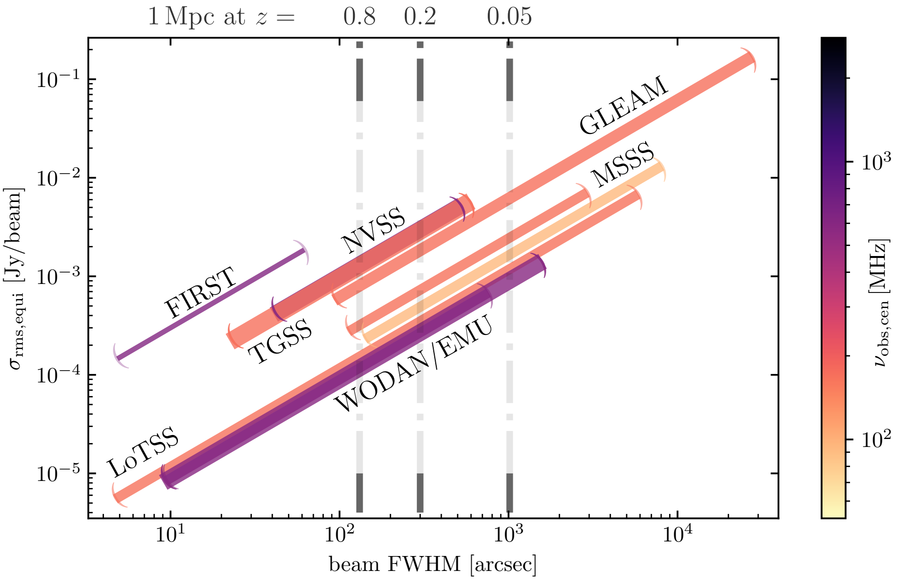

FIGURE 2.2: Shown is the r.m.s of high-resolution radio sky surveys for their sensitive scales ranging from the FWHM up to its largest imageable scale due to Eq. 2.3: The sensitivities $\sigma_{\mathrm{rms,equi}}$ are scaled to an equivalent of the σ_{rms} at 1.4 GHz frequency for a relic with spectral index $\alpha = -1.25$; and to different angular scales via Eq.2.3. The width of the line is proportional to the survey fractional sky coverage. The angular scale for a 1 Mpc sized relic at a given redshift is indicated at the upper border.

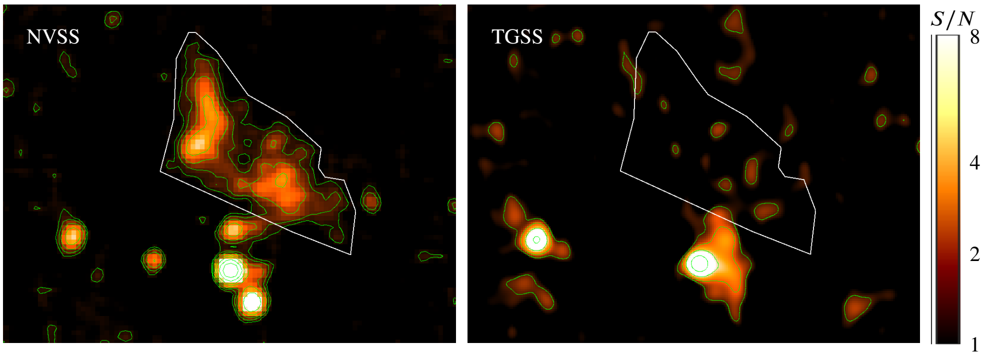

FIGURE 2.3: Galaxy cluster A2256 in both the NVSS (left) and TGSS ADR1 convolved to NVSS resolution of 45″ FWHM (right). Contours are flux levels starting from $2\sigma_{\mathrm{rms}}$ and increase by factors of 2. Due to extrapolation of the spectral index, both relic images should yield a detection of similar S/N for A2256. While the authors of TGSS ADR1 (Intema et al., 2017) point out a reduced sensitivity of this survey for extended sources this effect is more pronounced than expected from the survey specifications (Tab. 2.1).

Two-metre Sky Survey (LoTSS, Shimwell et al., 2017).

Future surveys like LoTSS, the Evolutionary Map of the Universe (EMU, Norris et al., 2011), and Westerbork Observations of the Deep APERTIF Northern sky (WODAN, Röttgering et al., 2011) will map much fainter relics than NVSS and make them available for an all-sky survey catalog. The joint use of these surveys will provide spectral index information for most relics known today. In the more distant future one can expect spatially-resolved polarization and spectral index maps for a large fraction of NVSS relics. Until then NVSS remains the survey best suited for radio relic studies because of its large fractional sky coverage.

2.3 Compilation of the NVSS relic database

In this section we present an updated compilation of radio relics and their host clusters. It continues the work of Nuza et al. (2017), which the author was part of, which used radio relic compilations of Nuza et al. (2012); Feretti et al. (2012); Yuan et al. (2015) and publications of new discoveries. Note that van Weeren et al. (2019) maintain a list of diffuse radio emission, including radio relics since mid 2018[1]. While it doesn't provide any access to images or point-source models, we used it as an independent source to ensure the completeness of our compilation.

We measure the radio relics' spatial location, size, and other parameters with the goal to encode the important-statistics in as few parameters as possible. This will become important once we compare the statistics of NVSS and synthetic surveys in Cha. 4.

2.3.1 Compilation of relic hosting clusters

The purity of the catalog of radio gischt is a major factor for the quality of any study based on it. Luckily, that most galaxy clusters with known radio relics have been studied interferometrically both with different radio arrays and at different frequencies. We use the classification scheme described in Sec. 1.2, differentiating between giant radio relics (i. e. radio gischt) and radio phoenices. For some objects the existing data is inconclusive and no clear classification is possible. We include these objects in our sample as *candidates*. Henceforward, we only consider clusters listed in Tab. 2.2 in the subsequent analysis as relic-hosting clusters.

---

[1] The compilation is listed under `https://galaxyclusters.hs.uni-hamburg.de/`.

TABLE 2.2: Shown are the radio relic hosting clusters selected for this study: Flux density of relics measured in NVSS images **column (4)** and reported in literature **column (5)**. The inventory of diffuse emission in the specific cluster is shown in **column (6)** with ‘(’ as main relic, ‘)’ as counter relic, ‘•’ as halo, and ‘*’ as diffuse emission that does not belong to any of these categories (comp Sec. 1.2). Grayed out objects are those considered only to be candidates.

Cluster (1)	z [] (2)	M_{200} $[10^{14} M_{\odot}]$ (3)	S_{NVSS} [mJy] (4)	$S_{1.4,\mathrm{lit}}$ [mJy] (5)	Diff. Emi. RHR* (6)	References mass | relics (7)
1RXS J06+42	0.225	12.9	309.9	364.0	(• *	Ogr13 - Wee16
A115	0.197	6.4	68.9	147.0	(	Fer12 - Gov01
A521	0.253	13.5	14.1	15.0	(•	Fer12 - Gia06
A610	0.095	3.0	15.9	18.6	(	Bos08 - Gio00
A746	0.232	7.8	13.1	24.5	(•	Fer12 - Wee11a
A781	0.300	8.7	16.8	15.5	(•	Fer12 - Gov11
A1240	0.159	3.5	12.4	16.1	( )	Fer12 - Bon09
A1300	0.307	18.2	18.1	20.0	(•	Fer12 - Ven13
A1351	0.322	12.9	19.2	13.0	(•	Gia09 - Gia09
A1443	0.269	11.0	9.0	9.8	(•	Bon15 - Bon15
A1612	0.179	6.0	62.0	62.8	(	Fer12 - Wee11a
A1664	0.128	7.4	99.7	107.0	(*	Fer12 - Gov01
A1682	0.226	12.0	18.6	26.9	(• *	Ven13 - Ven13
A1758N	0.280	12.3	16.2	24.7	(• *	Ebe98 - Bot18
A2034	0.113	8.5	28.3	24.0	(• *	Ebe98 - Wee11a
A2061	0.097	8.7	6.5	27.6	(	Wee11a - Wee11a
A2163	0.203	26.3	13.0	18.7	(•	Fer12 - Fer01
A2256	0.058	8.7	188.0	462.0	(•	Cla06 - Cla06
A2345	0.177	11.0	82.2	59.0	( )	Bon09 - Bon09
A2744	0.308	17.4	10.7	18.2	(•	Fer12 - Gov01
A3365	0.093	3.2	39.8	47.9	( )	Wee11a - Wee11a
A3411	0.169	8.3	24.7	53.0	(• *	Ebe02 - Wee13
A3527-bis	0.200	3.3	23.1	35.0	(	Gas17 - Gas17
CIZA J0107	0.107	8.7	6.5	30.0	( )	Ran16 - Ran16
CIZA J0649	0.064	6.3	19.3	27.5	(	Wee11a - Raj17
CIZA J2243	0.192	12.0	110.6	144.0	(• *	Fer12 - Str13
MACS J0717	0.555	11.5	108.8	83.0	(•	Fer12 - Pan13
MACS J1149	0.544	16.2	14.7	10.3	( )	Bon12 - Bon12
MACS J1752	0.366	12.3	91.9	101.8	(•)*	Bon12 - Bon12
PLCK G200	0.220	2.7	21.7	24.9	(	Kal17 - Kal17
PLCK G287	0.390	53.0	59.0	58.0	(•)	Fer12 - Bag11
PSZ1 G004	0.516	10.4	13.0	19.0	(	Shi14 - Shi14
PSZ1 G097	0.300	7.6	21.1	27.2	( )	Gas14 - Gas14
PSZ1 G108	0.332	7.7	105.0	113.1	(•)	Gas15b - Gas15b
RXC J0225	0.061	2.0	31.5	37.0	(	Sha16 - Sha16
RXC J1054	0.070	8.5	8.6	15.0	(	Fer12 - Wee11a
RXC J1314	0.247	15.8	41.4	30.3	(•)	Fer05 - Fer05
ZwCl 0008	0.104	2.2	45.7	67.0	( )	Fer12 - Wee11c
ZwCl 2341	0.270	5.8	24.1	22.0	( )	Gas14 - Gio10

Some objects formerly listed as radio relics are now classified as rare types of radio galaxies. For the diffuse emission near the galaxy cluster Abell 786 Kale and Dwarakanath (2012) reported a compact radio source near the center of the emission. The diffuse emission near the galaxy cluster Abell 2069 formerly listed as relic candidate has been also identified to be part of a radio galaxy (Drabent et al., 2015). Therefore, we do not include these sources in our list. Information about disregarded cluster emission can be found in Tab. A.1.

While the galaxy cluster dynamic state is motivation for an ubiquity of scientific investigations (Markevitch and Vikhlinin, 2007; Hitomi Collaboration et al., 2017; Golovich et al., 2018), we limit ourselves to three cluster parameters in this work: redshift, center position and cluster mass.

Galaxy cluster redshift

We do not further curate this data but rather use the value given in the publications concerning the radio relic(s). The adopted redshift is predominantly taken from studies which agglomerate the spectral-line redshift of all galaxies associated to the galaxy cluster.

Galaxy cluster center position

We derived the physical distance of relics from the cluster center using the known redshift of the clusters. In Nuza et al. (2017) we used the Set of Identifications, Measurements and Bibliography for Astronomical Data (SIMBAD) catalogue for the cluster positions (Wenger et al., 2000). However, SIMBAD positions are not determined homogeneously from the X-ray surface brightness distribution. Some cluster positions are based on observations of the thermal-Sunyaev-Zeldovic effect. In a few cases like ZwCl 0008+5215 and PSZ1 G108.18-11.53 this leads to a significant offset of several NVSS resolution elements (i.e. several 100 kpc) compared to the reported X-ray peak.

Where possible, we use positions that are based on the X-ray peak of the most massive cluster component. This is also consistent with the reference used for the synthetic survey (see Cha.3). Note that de Gasperin et al. (2014) use center coordinates that are based on the center of double relics - which is a measure independent of X-ray emissions. However, because this would limit our galaxy cluster sample to less than half the current size we use the aforementioned method.

Deriving cluster masses and radii

Though radio relics occur in merging systems we do not separate the galaxy cluster in several components but only consider its total mass. By knowing the cluster mass and characteristic radii we are able to investigate relic-cluster mass relations, and to map relic positions in units of R_{200}. For conversion of $M_{\Delta_c}(z)$, of an over-density $\Delta_c(z)$ to $M_{200}(z)$ we adopt the Navarro-Frenk-White profile (Duffy et al., 2008), specifically we use the Python implementation of Dietrich (2016).

We always convert the most reliable mass estimate to M_{200} and use this value to derive all other measures: Used measures on the mass are in decreasing order of preference the Sunyaev-Zeldovic effect, microlensing, and X-ray luminosity. The X-ray luminosity is the most prevalent proxy to estimate the cluster mass - comprising 70 percent of the sample. We convert X-ray luminosity $L_{500,0.1-2.4}$ to cluster masses via the relation in Böhringer et al. (2014, Eq.10) that we reorganize to M_{200}:

$$M_{200} = 3.467 \cdot 10^{14}\,\mathrm{M}_\odot \cdot \left(\frac{L_{500,0.1-2.4}}{10^{44}\,\mathrm{erg/s}}\right)^{0.6623} E(z)^{-1} \tag{2.4}$$

with $E(z) = \sqrt{\Omega_M(1+z)^3 + \Omega_\Delta}$. Note that galaxy cluster luminosity and their dynamic state are correlated, i.e. the mass of merging cluster observed along their collision-axis tends to be underestimated Takizawa et al., 2010. We do not implement any correction for this effect, which should be in the range of ~ 10 percent in average.

2.3.2 Analyzing NVSS Images

We use radio images provided by the NVSS Postage Stamp Server[1] and measure flux density, size and shape for all relics hosted by the clusters in Tab. 2.2. Note that we do not attempt to perform a surface brightness limited survey, but measure properties of already known relics. We do this, because this work does not aim for increasing the sample of known relics but for interpreting it. By pre-selecting the relic regions, the Eddington-Bias (Eddington, 1913), i.e. overestimation of source count due to image noise, is effectively eliminated.

For NVSS this procedure needs three further inputs in addition to the image: a relic selection region; a catalog of compact sources to subtract; and the cluster center. We first define regions that enclose the relic reported in the literature. This is done

---

[1] cv.nrao.edu/nvss/postage.shtml

manually to include the full region of interest, while keeping the number of sources to be subtracted low.

We compiled a list of sources that get subtracted from the images and are parameterized by a Gaussian with position, flux density, and FWHM (Appendix A). We implemented source subtraction in the image space and used the residual images for any subsequent analysis (Fig. 2.4).

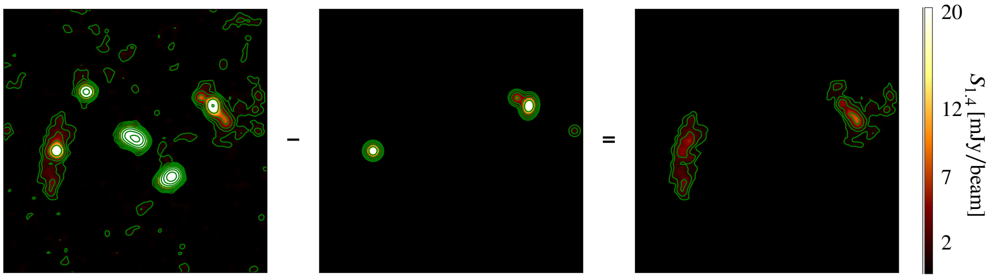

FIGURE 2.4: Image subtraction for the case of the galaxy cluster Abell 2345: NVSS image (left), component model (middle), subtracted (right). The colorscale denotes the flux density per beam. Note than only sources that do overlap with the radio relics need to be included in the source model.

To identify the relics within the residual images we apply a threshold on the areal flux density of each pixel, i.e. $S_{\mathrm{th}} = 2 \times \sigma_{\mathrm{NVSS}}$. We choose this value, because it is low in terms of the rms noise level. We do this to recover as much diffuse flux as possible. Note that even with this value, some relics decompose into several objects, like Abell 3411. Others are not detectable at all like the relics in clusters labeled as 'too faint' in Tab. A.1. In some cases the selection boundaries attenuates the pixels which where otherwise connected above low signal-to-noise threshold. We tried to minimize this effect through thoroughly choosing the relic region. Fig. 2.5 shows six examples of relics within NVSS with their diverse recovered morphologies.

We measure the properties of each separated object. Its solid angle Ω is the angular area of all constituent pixels. We also determine the largest angular scale (LAS), by the diameter of the smallest circle that encloses the object. From the latter, we also derive the largest linear size (LLS) of the objects by adopting the galaxy cluster redshift. The spectral flux density $S_{1.4}$ results from summing the surface brightness over the relics' pixels and dividing by the beam solid angle in units of pixels. The restoring beam solid angle:

$$\Omega_{\mathrm{beam}} = \frac{1}{\ln 2} \frac{\pi}{4} \Theta^2_{\mathrm{FWHM}} \tag{2.5}$$

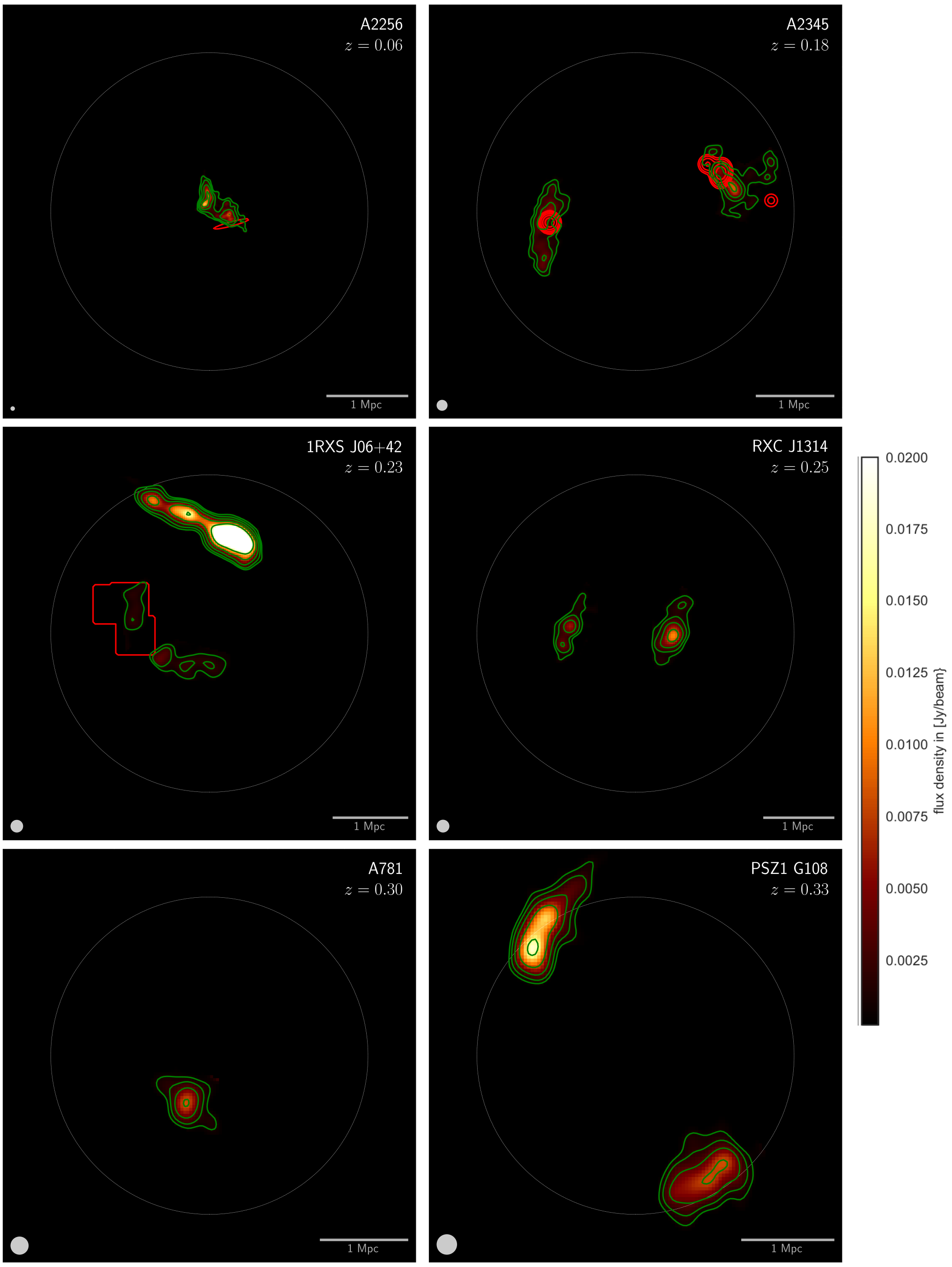

FIGURE 2.5: Examples of NVSS radio emission within the selection region after subtraction of compact sources. The color scale indicates the surface brightness distribution. Green contours show the diffuse emission, red contours the subtracted compact emission. Contours are drawn at [2,4,8,16,32] σ_{NVSS}, where σ_{NVSS} is the average rms brightness fluctuations in the NVSS images. Indicated are the R_{200} cluster vicinity (white circle).

derives itself from its associated Θ_{FWHM}. We adopt 45″ as FWHM of the restoring beam and neglect the beam's small size variations across the survey area.

The NVSS was carried out with the VLA in D and DnC configurations in snapshot mode, hence, above a largest angular scale of 8′ flux density measures are biased (comp. 2.1). In particular, for clusters at redshifts $z < 0.05$, relics of a typical size of 1 Mpc are too extended for a reliable flux density measurement. In fact, for the extended relics in Abell 2256, Abell 115 and CIZA J2242 - all of them at redshift ∼ 0.05 - we measure less flux density in NVSS than reported in the literature (Fig. 2.6). The cluster ZwCl 0008 is a good example of flux loss at a roughly 1 Mpc sized relic at $z \sim 0.1$.

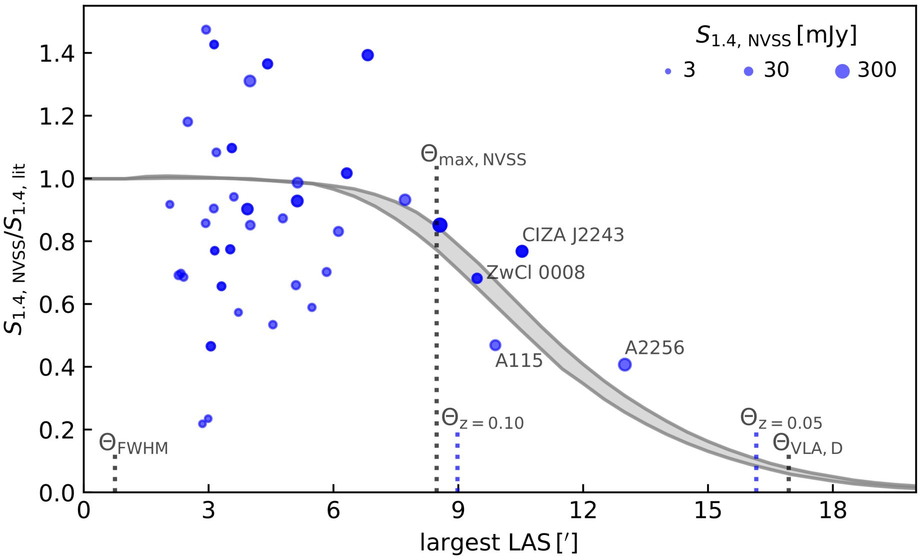

FIGURE 2.6: The effect of missing flux density due to limited short baselines (Eq. 2.2) is illustrated by the ratio of measured NVSS and literature flux density for each cluster $z > 0.05$ plotted over the LAS of the largest identified relic. Expectations for the NVSS as empirically derived by Farnsworth et al. (2013) are indicated by the gray shaded region. Also shown are angular scales Θ_z for distances of 1 Mpc at different redshifts.

We also do not want to include faint objects that could be heavily affected by the image noise. We disregard all objects below a flux density of $S_{1.4,\mathrm{min}} = 8 \cdot \sigma_{\mathrm{NVSS}} \cdot \mathrm{beam}$, i.e. 3.6 mJy, which is a compromise between reliable measures and a large object count. The final relic catalog is shown in Tab. 2.3 and includes 55 objects in 39 clusters.

We use the flux density of each object to infer its radio luminosity in the restframe, $P_{1.4}$. The redshift-dependent shift of the spectrum

$$P_{\mathrm{rest},1.4} = P_{\mathrm{obs},1.4} \cdot (1+z)^{-1-\alpha_{\mathrm{int}}} \tag{2.6}$$

is accounted for by the so-called k-correction (Hogg et al., 2002). For radio relics with unknown α_{int} we use the median spectral index of NVSS radio relics $\langle\alpha_{\mathrm{int}}\rangle$ of -1.25. We utilize image moments to describe the objects through their area, signal intensity, centroid, and shape. Image moments find use in astronomical source extraction tools (Stobie, 1980; Bertin and Arnouts, 1996). First, the emission-weighted center (x_c,y_c) of each object is determined. The central moments, μ_{pq}, of order $p+q$ are computed as

$$\mu_{pq} = \sum_i \sum_j (x_i - x_c)^p (y_i - y_c)^q I_{ij} \tag{2.7}$$

with the pixel coordinates (x_i,y_j) and the pixels surface brightness I_{ij}. By taking the ratio

$$s \equiv \lambda_2/\lambda_1 \tag{2.8}$$

with λ_1 as λ_2 the first and second eigenvalues of the covariance matrix $\mathbf{M}$

$$\mathbf{M}_{\mathrm{cov}} = \frac{1}{\mu_{00}} \begin{pmatrix} \mu_{20} & \mu_{11} \\ \mu_{11} & \mu_{02} \end{pmatrix} \tag{2.9}$$

we get a descriptor of the shape s of the object which is also closely related to the ellipticity e

$$e = \sqrt{1 - s^2}\,. \tag{2.10}$$

Rotational symmetric objects have a shape parameter of $s = 0$, linearly extended ones $s = 1$. Higher order image moments yield the degree and direction of the object's asymmetries like curvature, and are left for future work.

The location of the relics is measured both absolutely and with respect to their host cluster. Because we want to highlight the extended nature of the relic, we derive the projected distance D_{proj} not by the relic central coordinates but by the distance of all pixels towards the cluster center x_{cc},y_{cc} weighted by the pixel-wise flux density S:

$$D_{\mathrm{proj,pix}} = \frac{\sum_{i,j\in\mathrm{obj}} \sqrt{(x_i - x_{\mathrm{cc}})^2 + (y_i - y_{\mathrm{cc}})^2} S_{ij}}{\sum_{i,j\in\mathrm{obj}} S_{ij}}\,. \tag{2.11}$$

This measure is not arbitrarily small but limited of roughly a quarter the source extend. We now will proceed to investigate some of the basic properties of the selected relics population.

TABLE 2.3: Radio relic objects identified in the NVSS images with a flux density $S_{1.4} > 3.6$ mJy, in clusters with $z > 0.05$ totaling 55 relics in 39 clusters.

Identifier	RA [deg]	Dec [deg]	α_{int}	$S_{1.4}$ [mJy]	$\log_{10}(P_{1.4})$ [W/Hz^{-1}]	LAS [']	LLS [kpc]	λ_2/λ_1	$D_{\mathrm{proj,pix}}$ [kpc]
1RXS J06+42 N	90.82	+42.30	-1.10 ± 0.02	289.1 ± 30.7	$25.66^{+0.04}_{-0.05}$	8.56	1865	0.06	1353
1RXS J06+42 S	90.87	+42.17	-1.28 ± 0.05	14.6 ± 3.7	$24.36^{+0.10}_{-0.13}$	4.56	994	0.09	601
1RXS J06+42 SW	90.94	+42.22	-1.11 ± 0.05	6.3 ± 1.9	$24.00^{+0.11}_{-0.15}$	2.97	647	0.15	1079
A115	14.00	+26.46	-1.20	68.9 ± 14.6	$24.91^{+0.08}_{-0.10}$	9.89	1943	0.08	739
A521	73.59	-10.28	-1.50	14.1 ± 3.1	$24.47^{+0.09}_{-0.11}$	3.61	859	0.13	918
A610	119.87	+27.12	-1.40	15.9 ± 3.4	$23.57^{+0.08}_{-0.10}$	2.93	310	0.40	318
A746	137.23	+51.58		13.1 ± 3.6	$24.35^{+0.11}_{-0.14}$	4.54	1014	0.12	1507
A781	140.13	+30.47	-1.40 ± 0.16	16.8 ± 2.9	$24.72^{+0.07}_{-0.08}$	3.19	857	0.54	644
A1240 N	170.86	+43.17	-1.20 ± 0.10	6.6 ± 2.1	$23.68^{+0.12}_{-0.16}$	3.15	520	0.36	656
A1240 S	170.96	+43.01	-1.30 ± 0.20	5.8 ± 1.7	$23.62^{+0.11}_{-0.15}$	2.18	361	0.44	1169
A1300 SW	172.95	-19.95		18.1 ± 3.0	$24.78^{+0.07}_{-0.08}$	3.13	854	0.40	1289
A1351	175.59	+58.50		19.2 ± 3.2	$24.85^{+0.07}_{-0.08}$	2.94	830	0.50	717
A1443	180.27	+23.10		9.0 ± 1.7	$24.34^{+0.07}_{-0.09}$	2.07	515	0.44	1276
A1612	191.96	-2.88	-1.40	62.0 ± 8.9	$24.77^{+0.06}_{-0.07}$	5.14	935	0.20	1090
A1664	195.88	-24.37	-1.10	99.7 ± 22.5	$24.65^{+0.09}_{-0.11}$	7.72	1062	0.75	1068
A1682 NW	196.68	+46.57	-1.62	18.6 ± 3.2	$24.48^{+0.07}_{-0.08}$	2.28	498	0.68	343
A1758N E	203.23	+50.55	-1.20 ± 0.10	8.2 ± 2.6	$24.34^{+0.12}_{-0.17}$	2.38	610	0.58	628
A1758N W	203.16	+50.56	-1.20 ± 0.10	8.0 ± 2.0	$24.33^{+0.10}_{-0.13}$	3.31	848	0.22	220
A2034 W	227.42	+33.52	-1.20	28.3 ± 3.7	$23.98^{+0.05}_{-0.06}$	2.50	309	0.49	808
A2061	230.00	+30.53	-1.00	6.5 ± 1.8	$23.20^{+0.11}_{-0.14}$	2.99	323	0.22	2116
A2163	244.06	-6.09	-1.00	13.0 ± 2.1	$24.21^{+0.07}_{-0.08}$	2.34	470	0.41	1581
A2256	255.84	+78.73	-1.20	188.0 ± 31.7	$24.19^{+0.07}_{-0.08}$	13.00	877	0.18	194
A2345 E	321.90	-12.19	-1.30 ± 0.10	42.5 ± 8.5	$24.59^{+0.08}_{-0.10}$	6.82	1231	0.09	1203
A2345 W	321.67	-12.14	-1.50	39.6 ± 8.1	$24.56^{+0.08}_{-0.10}$	6.00	1082	0.70	1304
A2744	3.67	-30.35	-1.25 ± 0.15	10.7 ± 3.2	$24.55^{+0.11}_{-0.15}$	5.48	1502	0.09	1470
A3365 E	87.27	-21.78		39.8 ± 8.7	$23.95^{+0.09}_{-0.11}$	6.12	636	0.15	880
A3411 a	130.51	-17.57	-1.00 ± 0.10	16.8 ± 3.3	$24.14^{+0.08}_{-0.10}$	3.05	530	0.29	1155
A3411 c	130.56	-17.54	-1.00 ± 0.10	7.9 ± 1.5	$23.81^{+0.08}_{-0.09}$	1.98	343	0.40	1247
A3527-bis	192.77	-37.03	-0.70	23.1 ± 4.8	$24.45^{+0.08}_{-0.10}$	5.10	1014	0.08	1408
CIZA J0107 SW	16.92	+54.09		6.5 ± 2.4	$23.29^{+0.14}_{-0.20}$	2.85	335	0.60	388
CIZA J0649	102.16	+18.02		19.3 ± 5.3	$23.29^{+0.11}_{-0.14}$	5.84	432	0.16	788
CIZA J2243 N	340.74	+53.15	-1.06 ± 0.04	93.7 ± 15.1	$25.02^{+0.06}_{-0.08}$	10.53	2028	0.10	1567
CIZA J2243 N	340.91	+53.09	-0.74 ± 0.07	12.3 ± 2.5	$24.13^{+0.08}_{-0.10}$	3.02	582	0.23	1553
CIZA J2243 S	340.64	+52.94	-1.29 ± 0.04	4.6 ± 1.3	$23.70^{+0.11}_{-0.14}$	2.52	484	0.16	1108
MACS J0717	109.40	+37.76	-1.10 ± 0.10	108.8 ± 12.1	$26.19^{+0.05}_{-0.05}$	3.99	1561	0.41	238
MACS J1149 NW	177.35	+22.39	-0.75	7.6 ± 1.5	$25.01^{+0.08}_{-0.10}$	2.08	805	0.32	1149
MACS J1149 SE	177.44	+22.36	-1.15	7.1 ± 1.8	$24.98^{+0.10}_{-0.13}$	3.13	1212	0.24	1238
MACS J1752 NE	268.09	+44.70	-1.16	64.6 ± 7.7	$25.51^{+0.05}_{-0.06}$	3.93	1209	0.22	1159
MACS J1752 SW	267.98	+44.63	-1.00	27.3 ± 3.6	$25.14^{+0.05}_{-0.06}$	3.23	992	0.41	1045
PLCK G200	72.59	-3.03	-1.21	21.7 ± 4.5	$24.52^{+0.08}_{-0.10}$	4.78	1025	0.14	1067
PLCK G287 N	177.71	-28.05	-1.30	37.7 ± 6.6	$25.35^{+0.07}_{-0.08}$	6.32	2023	0.12	604
PLCK G287 S	177.81	-28.19	-1.50	21.2 ± 5.2	$25.10^{+0.10}_{-0.12}$	5.20	1664	0.17	2879
PSZ1 G004	289.27	-33.52		13.0 ± 2.1	$25.18^{+0.07}_{-0.08}$	2.40	904	0.42	214
PSZ1 G097 N	284.15	+66.44		7.3 ± 1.9	$24.36^{+0.10}_{-0.13}$	2.70	727	0.15	1005
PSZ1 G097 S	284.18	+66.33		13.7 ± 3.3	$24.63^{+0.09}_{-0.12}$	3.52	947	0.24	873
PSZ1 G108 NE	350.71	+48.82	-1.25 ± 0.02	61.1 ± 7.7	$25.39^{+0.05}_{-0.06}$	5.13	1480	0.16	1673
PSZ1 G108 SW	350.56	+48.66	-1.28	43.8 ± 6.9	$25.24^{+0.06}_{-0.07}$	3.76	1084	0.39	1534
RXC J0225	36.47	-29.61		31.5 ± 4.7	$23.45^{+0.06}_{-0.07}$	4.00	282	0.21	891
RXC J1054	163.21	+54.94		8.6 ± 1.9	$23.02^{+0.09}_{-0.11}$	3.72	299	0.12	740
RXC J1314 E	198.70	-25.26	-1.20	14.0 ± 2.8	$24.44^{+0.08}_{-0.10}$	4.32	1011	0.12	992
RXC J1314 W	198.58	-25.26	-1.40	27.4 ± 4.8	$24.73^{+0.07}_{-0.08}$	4.42	1034	0.22	516
ZwCl 0008 E	3.11	+52.61	-1.60	35.5 ± 8.7	$24.00^{+0.10}_{-0.12}$	9.45	1085	0.04	889
ZwCl 0008 W	2.79	+52.51	-1.50	10.2 ± 2.9	$23.46^{+0.11}_{-0.15}$	3.60	413	0.25	716
ZwCl 2341 N	355.91	+0.35	-1.31 ± 0.14	9.4 ± 2.1	$24.36^{+0.09}_{-0.11}$	2.70	674	0.23	579
ZwCl 2341 S	355.95	+0.23	-1.20 ± 0.18	14.7 ± 3.8	$24.55^{+0.10}_{-0.13}$	3.56	888	0.43	1312

2.4 Statistics of radio relic properties

Scatter-plot matrices are a standard tool for statisticians to assess the distribution of parameter pairs. In Fig. 2.7 we apply this technique to LLS, power, integrated spectral index and projected distance of NVSS relics. The plot includes three sub-sections which visualize the distribution of the measures in different ways. Most of these quantities and their relations were already discussed in other publications and we go ahead to describe the ones that we think of to be most important. In Nuza et al. (2017) we investigated the luminosity function, shapes, orientation angles and LLS distribution of radio relics. Of particular interest are correlations between, parameter pairs, because they allow to draw conclusions on the scaling-relations of physical quantities. For this purpose we adopt the significance test, with the p-value indicating the probability that there is *not* a Pearson correlation between the variables.

2.4.1 Correlations of measured quantities

The $P_{1.4}$-LLS correlation was first presented in Feretti et al. (2012). In our sample this parameter pair shows the strongest correlation with a correlation coefficient of 0.82 in line with our recent publication (Nuza et al., 2017) and a scaling of

$$P_{1.4} \propto \mathrm{LLS}^{2.39\pm0.21} \tag{2.12}$$

The slope tentatively being larger than two indicates that the relics with the largest LLS also are the ones with the highest surface brightness (Nuza et al., 2017, comp. Fig. 12). Later, we argue that this correlation arises largely from compiling a surface-brightness (comp. Fig. 3.14).

Of particular interest for models of particle acceleration at radio relics are the integrated spectral index and the corresponding Mach number (see Eq. 1.23) of the shock. They encode the efficiency of the acceleration mechanisms for different Mach numbers. Relics emission in A3527-bis, MACS J1149 NW, and CIZA J2243 N was measured with an integrated spectral index larger than -1 which violates the range that is possible when assuming thermal pool DSA at stationary shocks. While miss-classification might be possible, the relics in the sample hold further investigations. The relic α_{int} and $D_{\mathrm{proj,pix}}$ show a tentative Pearson correlation with a p-value= $5.45 \cdot 10^{-2}$, supporting the idea that the Mach-number of merger-shocks tends to increase as they transverse outwards. Interestingly, in their review paper van Weeren et al. (2019) do not mention this correlation, but rather discard a previously

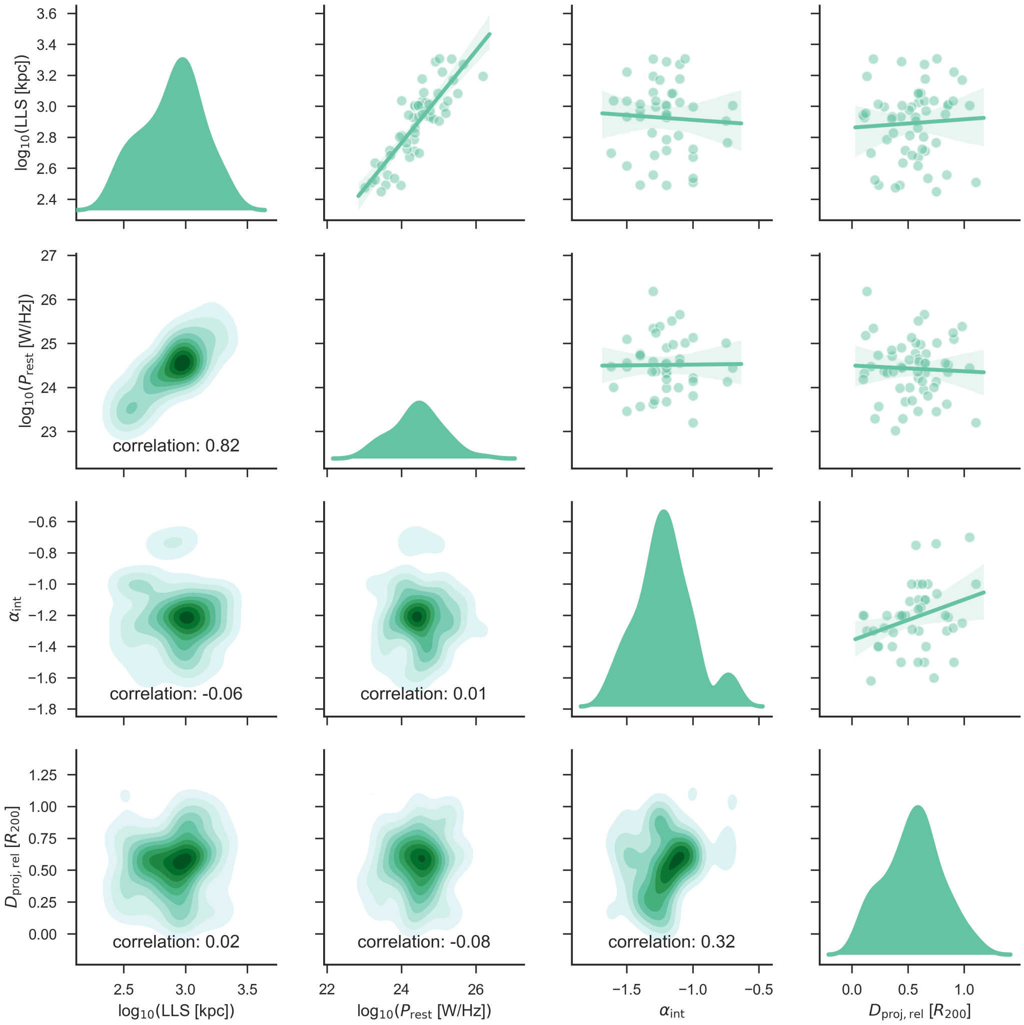

FIGURE 2.7: Shown are the scatter matrices of measured properties of NVSS relic in Tab.2.3 consisting of a regression plot with 1σ confidence shaded area **(upper right)** as well as the kernel density estimation (KDE)s for one **(central diagonal)** and two parameters **(lower left)**.

hypothesized LLS - α_{int}correlation from van Weeren et al. (2009). Due to the strong scaling of thermal-pool DSA efficiency with the Mach number one might expect a significant correlation of the integrated spectral index α_{int} and power P_{rest}. In resemblance of Colafrancesco et al. (2017), we do not find any significant α_{int}-P_{rest} correlation (comp. Sec.1.2.2).

Also, some correlations differ from the ones reported in the literature, due to our differing sample selection criteria. We do not observe a correlation between LLS and D_{proj} as found by (van Weeren et al., 2009; Bonafede et al., 2012; de Gasperin et al., 2014). We reject the hypothesis of correlation with a p-value of 0.991 when expressing D_{proj} in units of R_{200} and p=0.484 when expressing D_{proj} in units of kpc. Relics below a projected distance of 0.3 R_{200} and above an LLS of 1.2 Mpc are MACS J0717, PLCK G287 N and A115. Relics above a distance of 0.6 R_{200} and below a size of 500 Mpc are A1240 S, A2061, A3411c, and RXC J0225. Only PLCK G287 N and A1240 S are in the sample of de Gasperin et al. (2014), the latter with a much larger LLS than in our sample. We explain this discrepancy in the measured LLS by the fact that for some of the relics in our sample only the brightest regions are taken into consideration (Fig. 2.1).

2.4.2 Emission power, redshift, and cluster masses

The mass of the cluster is correlated with several measures of the relic statistics (Fig. 2.8). The strong $P_{1.4}$-redshift correlation indicates the prevalence of a significant Malmquist-Bias, i.e. detection of only the brightest objects of a population depending on their distance. At the same time a considerable M_{200}-redshift correlation correlation exists. Any $P_{1.4}M_{200}$-correlation derived from our sample should hence to a large degree, be influenced by the Malmquist-Bias.

A correlation of X-ray power and radio power of galaxy clusters was established by Feretti et al. (2012). This was confirmed by de Gasperin et al. (2014) in the form of the correlation of mass and radio power for double relics with the following coefficients:

$$P_{1.4\,\mathrm{de\,Gasperin}} \propto M_{500}^{2.83\pm0.39} \tag{2.13}$$

We confirm a correlation with a p-value of $3.23 \cdot 10^{-4}$ but find a much weaker trend:

$$P_{1.4\,\mathrm{this\,work}} \propto M_{200}^{1.05\pm0.27} \tag{2.14}$$

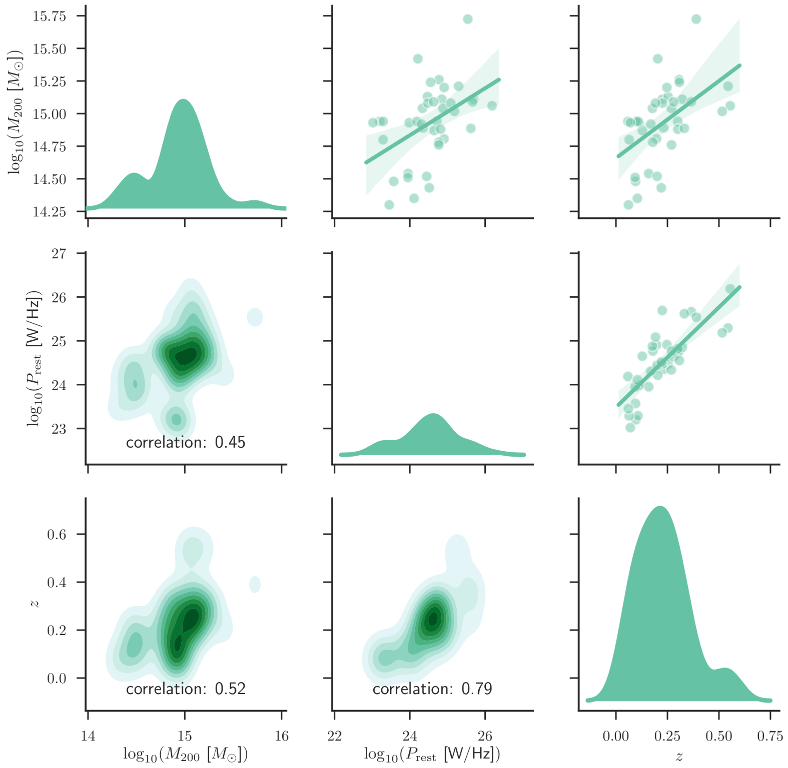

FIGURE 2.8: Shown are the KDEs of NVSS cluster-wide quantities that are significantly correlated with M_{200}.

When only considering double relics in our sample we obtain

$$P_{1.4\,\text{this work,double}} \propto M_{200}^{1.13\pm0.37} \tag{2.15}$$

which differs very much from the estimate in de Gasperin et al. (2014). The two relics in our sample that skew the linear estimate the most are CIZA J0107 and PLCK G207. CIZA J0107, not being in the double relic sample of (de Gasperin et al., 2014), is under-luminous for its mass. Same holds for PLCK G207 which we present with $M_{200} = 53\,M_\odot \rightarrow M_{500} = 39\,M_\odot$ i.e. 2.8 times larger than the values used in (de Gasperin et al., 2014). Adjusting the sample for these differences leads to a somewhat steeper slope of 1.69 ± 0.38, which is still much shallower than the 2.83 from (de Gasperin et al., 2014). The reason is that many other differences remain, like differences of the referenced radio power of ZWCl 2341, or the fact that (de Gasperin et al., 2014) fits the relics with weights due the known error of the measurement. This case exemplifies that fitted correlations sensitively depend on the selection procedure of objects and their values.

2.4.3 The average projected radio relic position in NVSS

We have now a rich selection of possible criteria to compare radio relics with simulations we will further use in Cha. 3-4. The last topic of this chapter are the quantities LAS, area and orientation angle ϕ. They describe the morphology of relics in the observation and were investigated in Nuza et al. (2017). Due to the limited scope of this thesis, we summarize these quantities together with the projected relic distance within one statistic. We thereby implement a new summary statistic of radio relic samples - the average projected radio relic. Deriving a general representation of the radio relic population by centering, aligning, and stacking provides a higher signal-to-noise representation of the typical relic sites in galaxy clusters. It follows up on the consideration of relic distances by Feretti et al. (2012); Nuza et al. (2017) using a projection scheme like the one applied to giant radio galaxies by Malarecki et al. (2015).

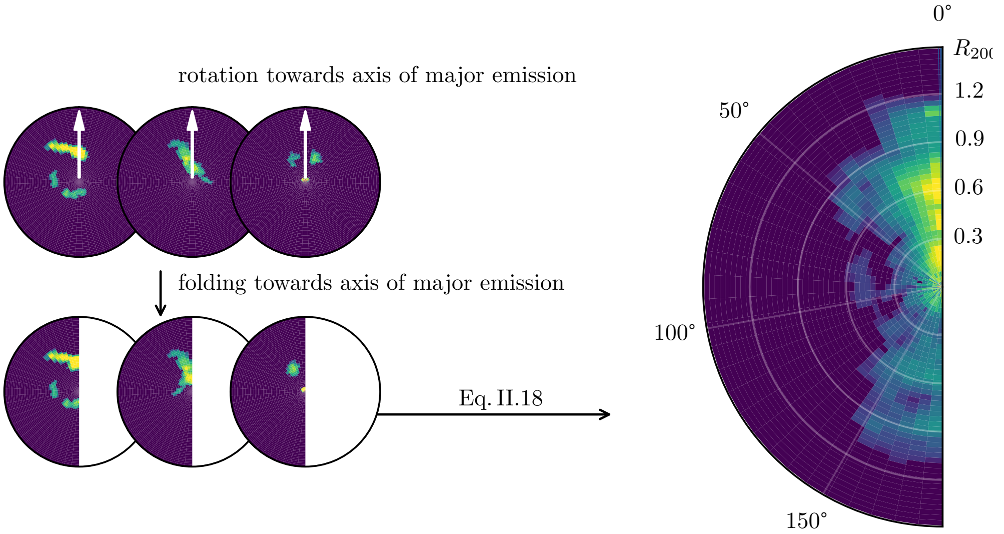

FIGURE 2.9: Shown is the scheme for the derivation of the average projected radio relic position on the example of NVSS.

While radio relics show a wide morphological variety, the variability can be reduced by aligning the images through rotation towards the axis of major emission. As seen in Fig. 2.9, we bin the radio relic flux $S_{1.4}$ in distance $D_{\mathrm{proj,pix}}$ expressed in units of R_{200} and position angle ϕ from the axis of major emission. In addition, we squeeze the signal by i) mirroring the axis of major emission and ii) deriving the weighted sum of all galaxy clusters.

We derive the direction of major emission by matching a template. The ad hoc chosen template I is the square-root of a dipole moment, and the chosen angle ϕ which maximizes the correlation with the flux density $s_{1.4}$:

$$R(\phi_{\mathrm{corr}}) = \int_{\phi} \sqrt{\cos^2(\phi - \phi_{\mathrm{corr}})} \cdot s_{1.4}(\phi - \phi_{\mathrm{corr}})\,\mathrm{d}\phi\,, \tag{2.16}$$

$$\phi_{\mathrm{best}} = \arg\max(R(\phi_{\mathrm{corr}}))\,. \tag{2.17}$$

A single sided, compact relic will result in a stark contrast between the best and all possible angles. In Fig. 2.10 we see how this approach pans out for our relic sample.

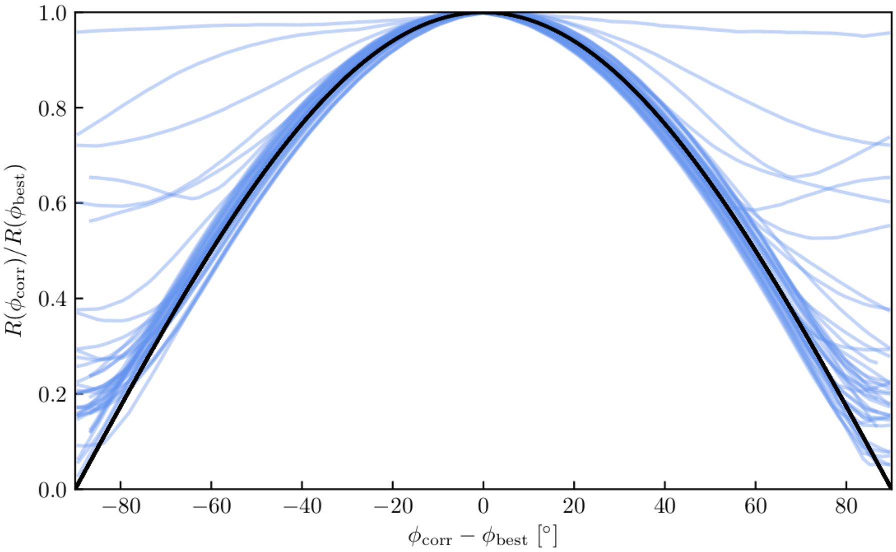

FIGURE 2.10: Results of template matching: Blue lines show the correlations R over varying angles (Eq.2.17) for all relics within our compiled NVSS sample. The correlation for a point source, i.e. very compact emission is shown in black.

Some cases like A2256 have a weak contrast, the most extreme case being the relic in PSZ1 G004. Other clusters show an increase towards 90° misalignment, which hints on relics orthogonal to the brightest relic. Most of the relics clearly have a favored direction, indicated by a large difference between the best and worst match with the template. In consequence, we are able to reliably find the direction of major emission with radio information and without the use of cluster morphological parameters. Now we average the resulting half-polar histograms $\mathbf{H_i}$ by summing the histogram of each galaxy cluster i

$$\mathbf{H}_{\mathrm{sur}} = \frac{1}{N_{\mathrm{cl}}} \sum_{i=1}^{N_{\mathrm{cl}}} S_{1.4,i}^{m} \mathbf{H_i}, \tag{2.18}$$

normalized by the total number of clusters $N_{\mathrm{cl}} = 39$ and weighted by its total flux density $S_{1.4}$ to the power of m. By choosing $m = -0.75 > -1$ we give slightly more weight to rare and high $S_{1.4}$ objects rather than the more common relic clusters with lower $S_{1.4}$. With this exponent, we find that the relic with most of the flux accounts to 4.5% of the total signal, while the average projected relic accounts for 2.2% of the signal. The reasoning for using a weight is that we expect more powerful relic clusters to be classified with higher confidence. By using flux density $S_{1.4}$ rather than P_{rest} we can give more weight to the more reliant radio relic detections as we work in the signal domain. Applying this routine to the NVSS sample creates a characteristic distribution (Fig. 2.11, bottom), that we linearly project with

$$\mathbf{v}_{\mathrm{D}} = \begin{pmatrix} 1 \\ 0 \end{pmatrix} \tag{2.19}$$

towards the axis of major-relic emission:

$$\mathbf{S}_{\mathrm{sur,D}} = \mathbf{H}_{\mathrm{sur}} \cdot \mathbf{v}_{\mathrm{D}} \tag{2.20}$$

to create the one-dimensional signal distribution (Fig. 2.11, top). The characteristics of the radio relic flux density distribution $\mathbf{S}_{\mathrm{sur,D}}$ at 1.4 GHz are:

- Ramp up of signal up to 0.6 R_{200}, followed by a sharp decline.
- Radio emission at $-0.6\,R_{200}$ with a signal ratio of $\sim$ 0.17 compared to the pro-relic side. We interpret this as the contribution of the merger along the counter-direction to the radio emission, e.g. double relics.
- Seven local, minor peaks exist. The galaxy cluster sample size suggest that most of those sub-features are a direct result of sampling noise. For later comparison we convolve $\mathbf{S}_{\mathrm{sur,D}}$ with a Gaussian of a FWHM of 0.3 R_{200}, resulting in a much smoother distribution that retains all the features mentioned above. In doing so we are confident that the intrinsic properties of the population statistic remain unchanged through this processing step.

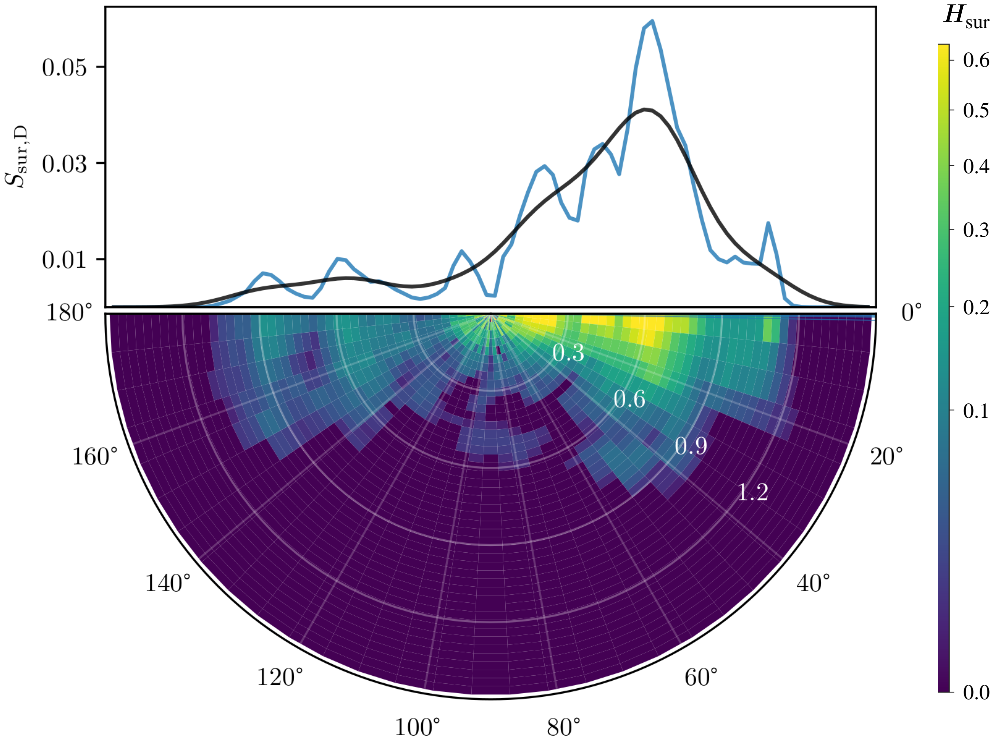

FIGURE 2.11: Shown are the relic summary for the NVSS survey of the weighted surface flux density according to Eq. 2.18 for all relics in Tab. 2.3 (bottom) and radially binned histogram according to Eq. 2.20 with (black) and without (blue) Gaussian smoothing (top).

2.5 Summary

We derived a sample of 55 NVSS radio relics in 39 galaxy clusters with focus on homogeneity in the observation setup to allow for a systematic comparison with simulations. This systematic setup allowed us to measure relic power at 1.4 GHz ($P_{1.4}$ GHz), largest linear scale (LLS), shape s, and projected distance from the cluster center ($D_{\mathrm{proj,pix}}$). We compare these measures against each other as well as their integrated spectral index α_{int}, the cluster mass M_{200}, and redshift z:

- We theorize that the most significant correlation of relic $P_{1.4} \propto \mathrm{LLS}^{2.39\pm0.21}$ is a direct result of the implementation of our synthetic observation. We will test the first hypothesis in Cha. 3.
- Other than van Weeren et al. (2009); Bonafede et al. (2012); de Gasperin et al. (2014) we do not confirm a correlation between LLS -D_{proj}, most likely also as a direct effect of our measurement procedure.
- We confirm the correlation by Feretti et al. (2012) between $P_{1.4}$ and $M_{200/500}$ with a p-value of $3.3 \cdot 10^{-4}$, albeit but find a much weaker scaling.
- There is a tentative (p-value= 0.055) correlation between D_{proj} and α_{int} which could result from the increasing average Mach-number of shocks towards the galaxy clusters outskirts. Other than the more recent van Weeren et al. (2019) we do confirm the finding of van Weeren et al. (2009).
- The very strong correlations of $P_{1.4}$ and M_{200} with the cluster redshift indicates that a strong Malmquist (selection of the brightest objects) bias likely imposed a strong influence on other measured correlations.

In this section we also investigated ways to summarize information on the radio relic population. Specifically, we encoded the location of the synchrotron radiation relative to the cluster center into an average projected radio relic. The collective signal strongly peaks at $D_{\mathrm{proj}} = 0.6\,R_{200}$. We will use these statistics for a comparative analysis with simulations in the following chapters.

Chapter 3

Synthetic sky surveys of radio relics

In this chapter we describe the model that we employ to create NVSS-like synthetic sky surveys of radio relics. We leverage the complexity of already simulated galaxy cluster mergers in cosmological simulations to provide a range of plausible scenarios for the generation of cluster merger shocks. In Sec. 3.1 we describe the requirements for our synthetic survey on the cosmological simulation adopted, known as MUSIC-2.

In Sec. 3.2 we describe the compilation of synthetic surveys, i.e. the generation of synthetic NVSS-like synthetic images used for the generation of survey products. We modify the approach of Nuza et al. (2017) to generate more realistic synthetic surveys. For the model of CR-electron acceleration we implement the solution of Hoeft and Brüggen (2007) which describes DSA from the thermal ICM.

With Sec. 3.3 we conclude this chapter by comparing radio relics in NVSS to the mock surveys based on the MUSIC-2 cosmological simulation for a set of model parameters, similar to the ones used in Nuza et al. (2017).

3.1 Cosmological Simulations

The standard measure to describe the volume of a cosmological simulation is the comoving volume. It is the volume locked to the Hubble flow - which is the standard to describe volume elements in cosmological simulations. The comoving volume element for intervals of solid angle Ω and redshift z is:

$$\mathrm{d}V_{\mathrm{com}} = D_{\mathrm{H}} \frac{D_{\mathrm{A}}^2}{H(z)/H_0} \mathrm{d}\Omega \mathrm{d}z \tag{3.1}$$

with the Hubble distance D_{H}, the transverse comoving distance D_{M}, and the Hubble expansion factor H. In a flat universe the local comoving distance is proportional to the local physical distance times the factor $(1 + z)$. A full sky survey up to $z = 0.22$ corresponds to $3\,\mathrm{Gpc}^3$ comoving volume. Up to a redshift of $z = 0.7$, which is the at the redshift of the most distant relic-hosting cluster in our sample, one would need a simulated comoving volume of 60 Gpc^3 to represent the observable Universe once.

While cosmological simulations become increasingly larger and more complex, trade-offs between five characteristics exists: The span in time and space, the spatial and temporal resolution, and the complexity of the implemented physics. The number of resolution elements that can be simulated is directly linked to the amount of available computing resources, typically a few million central processing unit (CPU)-hours. The largest cosmological simulations therefore often have a resolution which is coarse compared to their smaller counterparts (comp. Tab. 3.1).

TABLE 3.1: Some existent cosmological simulations that can contribute to radio relic population studies: Simulations with a comoving volume *'zoomed'* comprise sub-volumes that were resimulated with the zooming technique of Klypin et al. (2001). The *Physics* column indicates the different physical modules implemented; dark-matter-only simulations (*gravity*), additional adiabatic hydrodynamic physics (*+hydro*), and additional hydrodynamic physics with radiative processes like Bremsstrahlung and supernova feedback (*+hydro+rad*). For the hydrodynamic suites, there is an equal amount of dark matter particles and gas particles of mass $\sim m_{\mathrm{dm}}/4$.

Name	V_{com} [Gpc^3]	m_{dm} [$\mathrm{M}_\odot$]	Physics	Reference/Comment
MultiDark	2.9	$1.3 \cdot 10^{10}$	gravity	Klypin et al., 2011
BigMDPL	46	$3.4 \cdot 10^{10}$	gravity	Klypin et al., 2016
HugeMDPL	187	$1.1 \cdot 10^{11}$	gravity	Klypin et al., 2016
Millenium-XXL	78	$8.9 \cdot 10^{9}$	gravity	Angulo et al., 2012
Magneticum B2b	0.8	$9.9 \cdot 10^{8}$	+hydro+rad	Dolag et al., 2016
Magneticum B0	57	$1.9 \cdot 10^{10}$	+hydro+rad	Dolag et al., 2016
MUSIC-2	zoomed	$1.3 \cdot 10^{9}$	+hydro & +hydro+rad	283 clusters from MultiDark with $M_{\mathrm{z=0}} > 1.4 \cdot 10^{15}\mathrm{M}_\odot$
MUSIC-2 new	zoomed	”	+hydro+rad	545 clusters from MultiDark with $M_{\mathrm{z=0}} > 7.1 \cdot 10^{13}\mathrm{M}_\odot$

Galaxy cluster simulations are performed on different levels of physical realism; in order of increasing fidelity:

I) Dark matter-only simulations are viable to trace the formation of dark matter halos of galaxy clusters and galaxies. Those simulations populate the largest volumes with galaxy clusters.

II) Hydrodynamic simulations include gas physics, hence also the thermal-ICM and shock fronts.

III) Magnetohydrodynamical (MHD) simulations include magnetic field which have a direct influence on the synchrotron emission process. MHD simulations are costly, but comprise a natural progression towards more realistic studies of plasma phenomena in galaxy clusters (Vazza et al., 2017). However, MHD-simulations are yet to be performed for volumes we consider large enough for our kind of study: once the simulated volume is a considerable fraction of the volume mapped by NVSS up to the redshift where relics are found (Fig. 3.1).

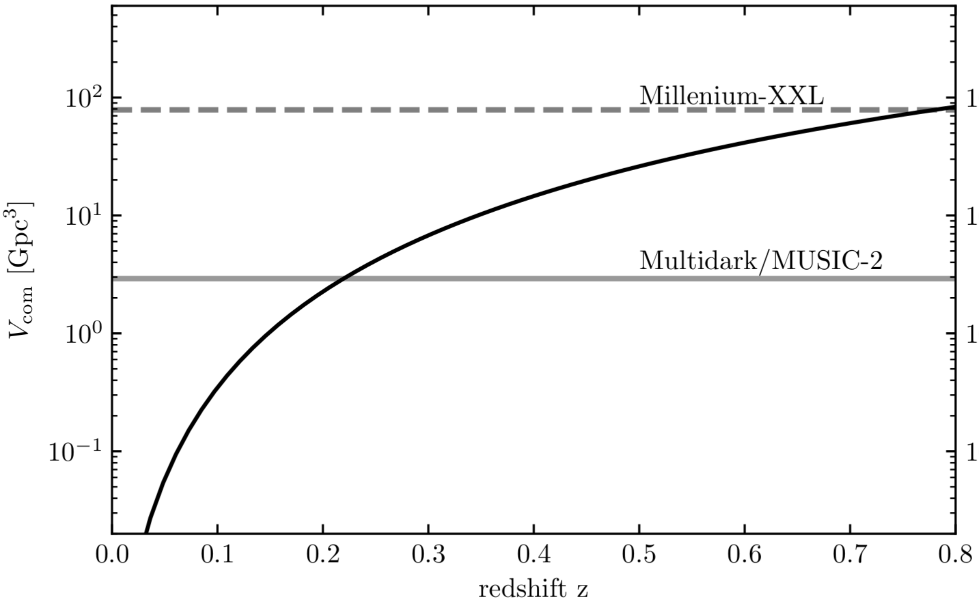

FIGURE 3.1: Shown is the integrated comoving-volume mapped by NVSS up to the redshift z (thick, curved line). For comparison, the volumes of the Multidark/MUSIC-2 and Millenium-XXL cosmological simulations are shown.

The largest simulated volumes maintaining large-scale shocks, being the single-most import physical phenomenon for this study, are provided by hydrodynamical simulations. In particular, we use MUSIC-2, which is a hydrodynamic re-simulation of MultiDark sub-volumes at the positions of massive galaxy clusters (Sembolini et al., 2013). All clusters with a $M_{200} > 1.4 \cdot 10^{15}\ M_{\odot}$ at $z = 0$ were re-simulated resulting in $N_{\mathrm{cl}} = 283$ different Lagrangian regions. As each cluster at $z = 0$ defines the center of one of those sub volumes, we use the terms *'sub-volume'* and *'cluster'* interchangeably. Starting from the same initial conditions two cases of different physics were simulated: an adiabatic simulation and one with cooling and heating physics. The dark matter particle mass in MUSIC-2 is $1.3 \cdot 10^9\ \mathrm{M}_{\odot}$. Therefore, a galaxy cluster with $M_{200} = 10^{15}\ M_{\odot}$ is represented by $8 \cdot 10^5$ dark matter and gas resolution elements each.

In smoothed particle hydrodynamics (SPH) simulation particles of a fixed mass $m_{\rm gas}$ represent physical subvolumes of gas. All quantities in SPH simulations are derived from mathematical operations on particle groups weighted by the so-called smoothing kernel. Ordinarily, the number of particles within the kernel is kept constant. Because of that, the resolution of an SPH simulation is linked to the adaptive smoothing length of the kernel $h_{\rm kernel}$ (Lodato and Clarke, 2011):

$$h_{\rm kernel} = 86\,{\rm kpc} \cdot \left(\frac{N_{\rm kernel}}{64} \cdot \frac{m_{\rm gas}}{10^9\,{\rm M}_{\odot}}\right)^{1/3} \left(\frac{n_e}{10^{-4}\,{\rm cm}^{-3}}\right)^{-1/3} . \tag{3.2}$$

The FWHM of the kernel is $2.4\,h_{\rm kernel}$ and proportional to $n^{-1/3}$, i.e. it increases in denser regions. To ensure that the derived quantities of the shock are reliable it is critical that the shock in SPH simulations is represented by a sufficient number of smoothing lengths. The shock finder employed to MUSIC-2 (Sec. 3.2.4) yields a FWHM of about 150 kpc in the region where most relics are found, i.e. $n_e \sim 5 \cdot 10^{-5}\,{\rm cm}^{-3}$.

3.2 Radio Relic Mock Surveys

Mock surveys are studies based on a set of synthetic observations. We implement a procedure to perform mock surveys of radio relics with the design of NVSS (Cha. 2). While it is possible to attempt mock surveys on full cosmological simulations, we use the already existing resimulation MUSIC-2 of massive galaxy clusters. For each of the 283 MUSIC-2 clusters, a simulation output exists at a particular time or *snapshot*. For MUSIC-2 the snapshots at $z < 0.7$ are

$$z_{{\rm snap},z<0.7} \in (0.05, 0.11, 0.18, 0.24, 0.33, 0.43, 0.54, 0.67) .$$

3.2.1 Distribution of clusters in the observed volume

To generate a sensible sample of galaxy clusters in the survey we have to distribute the available simulated volume of MUSIC-2 across the full observed light cone. While MUSIC-2 includes the most massive galaxy clusters in a volume as large as $3\,{\rm Gpc}^3$, it comes at the cost that most of the original volume is not simulated. We hence cannot simply create a light cone that integrates the full signal along a line of sight.

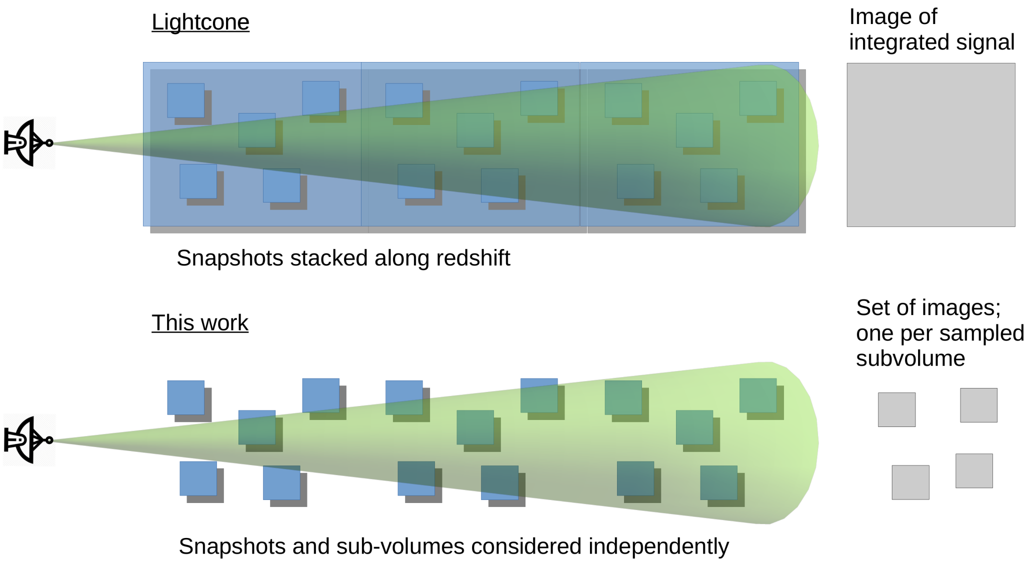

FIGURE 3.2: Scheme of the distribution of clusters in the survey volume, illustrating the difference between a simulated light cone and our survey approach.

All NVSS relic detections in our sample can be attributed to individual merging galaxy clusters. We therefore assume that the integrated signal of individual radio relics at NVSS-like sensitivity can mostly be recovered from a single sub-volume of MUSIC-2 instead of a full light-cone. Following Nuza et al. (2017), we select sub-volumes and treat them as observations along an independent line of sight (Fig. 3.2). We also assume that the galaxy clusters are homogeneously distributed on cosmological scales. This resembles the cosmological principle and can be applied to clusters which are common at their observed redshift. We know that this is not completely true as clusters represent notes in the filamentary cosmic web, but the spatial correlation, but, for our purposes, the spatial correlation of galaxy clusters can be safely neglected.

The comoving volume mapped by a NVSS-like survey up to a redshift of 0.7 is twenty times larger than the volume that MUSIC-2 is based on. By default this will lead the synthetic population of radio relics to show relatively less fidelity, limiting the effectiveness of forward simulations. To alleviate this limitation as much as possible we use MUSIC-2 galaxy clusters more than once: i) with different rotations; ii) at different snapshots, iii) and at different observed redshifts. Randomization of the rotation is effective at increasing the sampling variance because, as shown in Hoeft et al. (2008); Skillman et al. (2011) and Nuza et al. (2017, Fig. 7), the natural variation of the viewing angle can account for the large morphological variety seen in radio relics. While the flux remains roughly constant, measured size, shape, and position relative to the cluster center depend sensitively on the relative orientation of the cluster towards the observer.

The second and third randomization techniques are implemented through a series of considerations: Starting from the redshift $z_{\mathrm{min}} = 0.05$, we divide the observed light cone in $N_{\mathrm{shell}} = 150$ shells of redshift width $\Delta z = (z_{\mathrm{max}} - z_{\mathrm{min}})/N_{\mathrm{shell}} = 4.3 \cdot 10^{-3}$. By using a small Δz we limit discretization effects and emulate a continuous volume. We now sample the volume-elements containing the massive galaxy clusters from a Poisson-distribution with the expected count λ. The volume of each shell within this light cone then becomes:

$$V_{\mathrm{shell},i} = V_{\mathrm{com}}(z_{i+1}) - V_{\mathrm{com}}(z_i) \tag{3.3}$$

whereas the integrated comoving volume $V_{\mathrm{com}}(z)$ is set by the minimum and maximum considered redshifts. Within each shell i the expected number of subvolumes to be selected is

$$\lambda_{\mathrm{shell},i} = \frac{V_{\mathrm{shell},i}}{V_{\mathrm{simu}}} . \tag{3.4}$$

Cosmological evolution plays a strong role for all mock surveys. An evolution of the large-scale structures exists throughout the various snapshots of the simulation. We account for this by predominantly mapping snapshots to shells with a comparable central redshift. We do this by attributing a Gaussian density function $p_j(z)$ of the variance σ in redshift space to any snapshot j, with a larger variance σ making it more likely that a snapshot is chosen for a shell at a very different redshift. Within each shell i the expected count for a given snapshot j is:

$$\lambda_{\mathrm{snap},i,j} = \frac{p_j(z_i)}{\sum_j p_j(z_i)} = \frac{\exp\left[-\frac{1}{2}\left(\frac{z_{\mathrm{shell},i}-z_{\mathrm{snap},j}}{\sigma}\right)^2\right]}{\sum_j \exp\left[-\frac{1}{2}\left(\frac{z_{\mathrm{shell},i}-z_{\mathrm{snap},j}}{\sigma}\right)^2\right]} . \tag{3.5}$$

The variance is chosen as $\sigma = 0.1$ in order to strike a balance between distributing many snapshots to a redshift shell and respecting the cluster evolution with redshift. Sky surveys only cover a fraction $f_{\mathrm{sc}} \leq 1$ of the whole sky. In this work we use the fractional sky coverage of NVSS, i.e. $f_{\mathrm{sc}} = 0.82$. The total expected count for any shell i, snapshot j and cluster k then becomes:

$$\lambda_{i,j,k} = f_{\mathrm{sc}} \cdot \lambda_{\mathrm{shell},i} \cdot \lambda_{\mathrm{snap},i,j} . \tag{3.6}$$

By definition this expected count $\lambda_{i,j,k}$ is independent of the galaxy cluster $k$and can be larger than one for any given redshift shell (Fig. 3.3). We consider this sampling procedure, specifically Eq. 3.5, as an effective improvement over Nuza et al. (2017) as it allows for a more consistent transition between different snapshots. It increases the internal sampling variance within any redshift range, which we consider to be crucial, because it is biased low by the limited amount of simulated volume. We also added four more MUSIC-2 snapshots to the six snapshots investigated in Nuza et al. (2017). This improves the fidelity of the forward modeling in the redshift range were NVSS radio relics are identified. For each realization of a mock survey, we now attain a list of galaxy clusters where each cluster has an affiliated snapshot, redshift, and projection. In our NVSS-like case for each mock survey from $z = 0.05$ to $z = 0.7$, the expected cluster number count relates itself to the snapshots, like that shown in Fig. 3.3. Within the range of the majority of relic detections, every simulated snapshot is mostly used less than two times. Snapshots at higher redshift enter the relic sample more often, but originate only few relics. At these high redshifts the majority of sampling variance can only come from the random viewing angle rather than the snapshot selection.

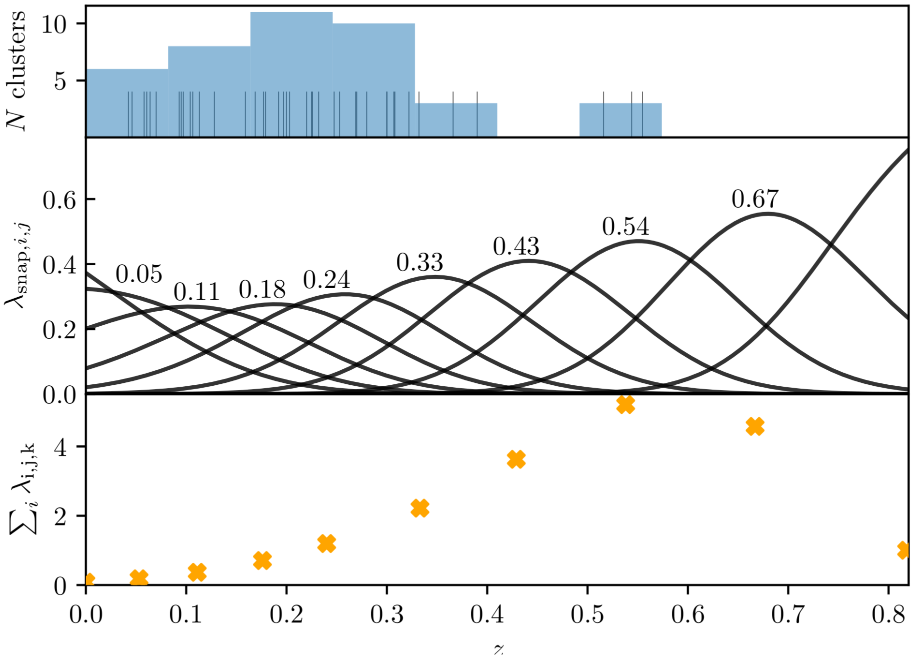

FIGURE 3.3: Plot of three redshift-related quantities: NVSS cluster count with relic detections (*top*); probability $\lambda_{\text{snap},i,j}$ of given snapshot to be selected at a given redshift due to Eq. 3.5 (*middle*); $\sum_i \lambda_{i,j,k}$ alias the expectation value of how often a snapshot of a galaxy cluster enters the sample due to Eq. 3.6 (*bottom*).

While any more sophisticated estimates of the galaxy cluster distribution and merger state will benefit future studies (Anderson et al., 2018) the most impactful biases are based on the simulation itself and occurs on several levels:

1) due to the limited volume of the simulation large scale modes will be attenuated, leading to a dearth of the most massive clusters at high redshift,

2) due to the limited resolution of the simulation, relics in low density environments can show an unrealistic morphology, flux, or might not even be found at all,

3) due to the limited selection of only the most massive clusters in MUSIC-2, relics in less massive clusters will not occur in the sample.

3.2.2 Acceleration model: DSA from the thermal pool

For the radio emissivity we follow the general framework of Hoeft and Brüggen (2007). The principal assumption is that Mach number and the exponent of the particle-distribution are linked through Eq. 1.22, in line with DSA, and that a fraction ξ_e of the energy of thermalized by the shock is put into CR-electron acceleration. We use Eq. 17 of Hoeft et al. (2008) to estimate the flux density of DSA synchrotron emission resulting from a quasi-stationary shock running through a fully thermalized collisionless ICM:

$$
\begin{aligned}
P_\nu &= 1.28 \cdot 10^{24}\,\mathrm{W\,Hz^{-1}} \\
&\cdot f_B \Psi(\mathcal{M},T_\mathrm{down}) \frac{A}{\mathrm{Mpc}^2} \frac{n_\mathrm{e,down}}{10^{-4}\,\mathrm{cm}^{-3}} \frac{\xi_e}{10^{-5}} \left(\frac{\nu_\mathrm{obs}}{1.4\,\mathrm{GHz}}\right)^{p_\mathrm{inj}/2} \left(\frac{T_\mathrm{down}}{7\,\mathrm{keV}}\right)^{3/2} && (3.7) \\
\text{with} \quad f_B &= \frac{(B_\mathrm{down}/\mu\mathrm{G})^{1-\frac{p_\mathrm{inj}}{2}}}{(B_\mathrm{CMB}/\mu\mathrm{G})^2 + (B_\mathrm{down}/\mu\mathrm{G})^2}. && (3.8)
\end{aligned}
$$

It includes the factor f_B of CR electron energy that arises from part of the CR energy being channeled in the inverse-Compton effect instead of synchrotron radiation (Eq. 1.15), the function $\Psi(M,T_\mathrm{down})$ that comprises all Mach number dependencies, the area of the shock front A, downstream electron density $n_\mathrm{e,down}$ and downstream ICM temperature, T_down the observing frequency ν_obs and the exponent of the CR electron power distribution p_inj (Eq. 1.22).

The model is derived for the so-called test-particle regime, i.e. the downstream pressure of the CR is small compared to the overall pressure and does hence not modify the shock dynamics. In consequence, the value of ξ_e is constrained to be $\lesssim 10^{-3}$ (Kang and Ryu, 2010). This is reinforced by the fact, that there is currently no observational evidence of an altered shock dynamic at merger-shocks. The function $\Psi(M,T_\mathrm{down})$ comprises both the dependency of the particle-power-law slope p of DSA on the Mach numbers (Sec. 1.2.1) and the fraction of downstream internal energy that is thermalized at the shock. Specifically, $\Psi(\mathcal{M},T_{\rm down})$ rises steeply from $\mathcal{M} = 2$ to $\mathcal{M} = 4$ where it starts to converge against a value of one. How the Mach number of the shocks are derived is shown on Sec. 3.2.4.

The shock surface area A of an SPH-particle is approximated by:

$$A = \frac{f_A}{N_{\rm SPH}} h^2_{\rm kernel} \tag{3.9}$$

scaled by a constant $f_A = 6.5$, the number of particles in the smoothing kernel $N_{\rm SPH}$ (Hoeft et al., 2008, Sec. 4.2, 4.4), and the smoothing length $h_{\rm kernel}$ (Eq. 3.2). The model assumes that the emission takes place on a thin surface, i.e. the aging of electrons downstream the shock is instantaneous. A typical relic width of 40 kpc at 1.4 GHz (comp. Eq. 1.21) is smaller than the NVSS resolution for clusters at $z > 0.045$. In this case the assumption yields a fair approximation of the observed emission.

For magnetic field strengths $B_{\rm down} \lesssim B_{\rm CMB}$, inverse-Compton cooling dominates over the synchrotron emission losses of CRes. Under these conditions the overall synchrotron emission becomes proportional to $B^2_{\rm down}/B^2_{\rm CMB}$ for high Mach number shocks. Because $B^2_{\rm CMB} \sim (1+z)^4$, inverse-Compton cooling can result in a strong additional down-scaling of radio relic brightness with redshift.

3.2.3 The magnetic field model

The hydrodynamical simulation that is employed does not include the magnetic field in its computations and output. As a necessary measure, we employ a model of the magnetic field based on properties that are recorded in the simulation snapshots. Following Dolag et al. (2001), we assume a power-law relation of the magnetic field strength and ICM upstream density:

$$B_{\rm up} = B_0 \left(\frac{n_{\rm e,up}}{10^{-4}\,{\rm cm}^{-3}} \right)^{\kappa} \tag{3.10}$$

where B_0 is the normalizing constant, κ the exponent of the power law and $n_{\rm e,up}$ is the upstream electron density. Other than in Nuza et al. (2017) we apply this power-law relation to the upstream density rather than the downstream density and utilize the Mach number dependent compression factor C (Eq. 1.9):

$$B_{\rm down} = B_{\rm up} \cdot C^{\zeta} \tag{3.11}$$

to let our model capture the magnetic field amplification due to shock compression (Iapichino and Brüggen, 2012, Eq.3). Particle-in-Cell simulations have quantified how the acceleration efficiency varies with the Mach number and obliquity (Caprioli and Spitkovsky, 2014; Guo et al., 2014a): CRes have a higher-acceleration efficiency in shocks were the ICM flow is perpendicular to the magnetic field. Wittor et al. (2017), however, finds that merger-shocks in the ICM are predominantly perpendicular shocks. This implies that most of the DSA induced synchrotron emission should stem from particles in magnetic fields most amplified by shock compression. If the synchrotron emission is sensitive to the absolute downstream magnetic field then compression implies $\zeta = 2/3$ for an unordered upstream magnetic field. We use $\zeta = 0.85$ which is an average of the former value and a DSA acceleration that is only efficient for the magnetic field component perpendicular to the velocity vector ($\zeta = 1$, see Wittor et al., 2017). We do not consider here that the downstream magnetic field strength might be further enhanced by shock upstream instabilities (Guo et al., 2014a) and downstream turbulence (Donnert et al., 2016). The estimate of the downstream magnetic field amplification hence is a lower bound.

3.2.4 Shock identification

Shock fronts are identified as described in (Hoeft et al., 2008; Nuza et al., 2012). The shock identification is performed particle-wise: For each gas particle, the pressure gradient and the shock normal are evaluated as $\mathbf{n} = \nabla\mathbf{P}/|\nabla\mathbf{P}|$. Three conditions are imposed on the shock candidate:

i) $\nabla \cdot \mathbf{v} < 0$, where $\mathbf{v}$ is the velocity field,

ii) $n_{\mathrm{e,up}} < n_{\mathrm{e,down}}$, with n_{e} as the electron density, i.e. it is not a cold front, and

iii) $S_u < S_d$, as the entropy for the upstream and downstream regions respectively.

For each of these three quantities we compute the Mach number based on the Rankine-Hugoniot equations for hydrodynamical shocks (Eq. 1.6 - Eq. 1.9) and obtain three different estimates of the Mach number $\mathcal{M}$. Following Nuza et al. (2017), we only consider the lowest of the three derived Mach numbers to suppress spurious detections of shocks. The statistics of shocks in a typical sample of galaxy clusters is shown in Fig. 3.4. While Ψ favors shocks of $\mathcal{M} > 5$, both $n_{\mathrm{e}}A$ and T tend to weight shocks of $\mathcal{M} < 3$ the most. The resulting product $\Psi n_{\mathrm{e}} A T^{3/2}$ which with exception of the magnetic field factor f_{B} defines the emission very much resides at the intersection of those curves, with most of the emission resulting from $\mathcal{M} = 2 \ldots 10$ shocks.

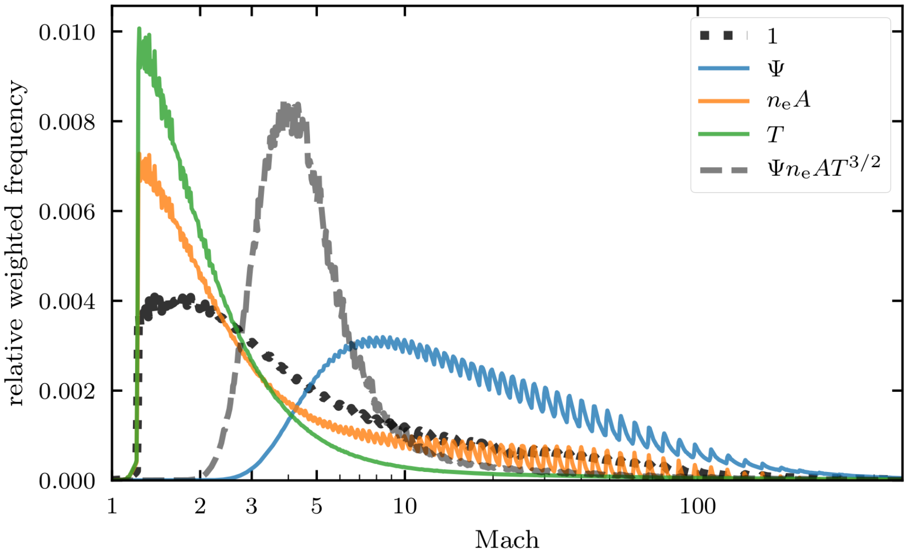

FIGURE 3.4: Shown is the histogram of the relative frequency of particles with a $\mathcal{M}$ shock weighted by quantities given in the legend in a representative sample of galaxy clusters in a synthetic survey.

Note that SPH-simulations in general tend to be noisy when deriving hydrodynamical properties. Especially density an-isotropies smaller than the kernel size will bias the estimate of the quantities derived from gradients, like the Mach number.

3.2.5 Mock image generation

For every cluster in our sample we create a mock image which together form a sample which can be compared with NVSS. Starting with the SPH particle radio luminosity (Eq. 3.8) we compute the radio flux density S_i for each simulated particle i above $\mathcal{M} > 1.5$ at 1.4 GHz

$$S_{i,1.4} = 83.6\,\mathrm{mJy} \cdot \frac{P_{1.4}}{10^{25}\,\mathrm{W\,Hz^{-1}}} \cdot \left(\frac{D_\mathrm{L}(z)}{1\,\mathrm{Gpc}}\right)^{-2} \tag{3.12}$$

with the redshift-dependent luminosity distance $D_\mathrm{L}(z)$, being around 1 Gpc at $z = 0.2$. As this emission stems from a galaxy cluster with $z > 0$ we apply the k-correction (Hogg et al., 2002) to compute the flux observed at $z = 0$:

$$S_{i,\mathrm{obs}} = S_{i,1.4}\;(1+z)^{\alpha_i+1}\;. \tag{3.13}$$

To produce mock images that resemble NVSS we first bin all particles within a distance of $2R_{200}$ from the cluster center into a map $\mathbf{m}$ with a pixel size of $10''$, i.e.

22 percent of the FWHM of the NVSS. We then convolve all maps of the flux density $\mathbf{m}_\mathrm{S}$ with the restoring beam $\mathbf{k}_\mathrm{beam}$ of NVSS:

$$\mathbf{m}_\mathrm{S,conv} = \mathbf{m}_\mathrm{S} * \mathbf{k}_\mathrm{beam}\,. \tag{3.14}$$

From these maps the relics are extracted like described in Sec. 2.3.2. In particular, all pixels within a $2\sigma_\mathrm{rms}$ threshold region are considered to be one relic instance. An excerpt from a typical sample of simulated radio relics is shown in Fig. 3.5. By only selecting relics above $S_{1.4} = 3.6\,\mathrm{mJy}$ and above redshifts $z = 0.05$ we select those objects that are least affected by image noise and reconstruction artifacts, respectively. The use of $\mathbf{m}_\mathrm{S,conv}$ hence comprises a computational inexpensive alternative to putting the maps $\mathbf{m}_\mathrm{S}$ through radio interferometric reconstruction pipelines.

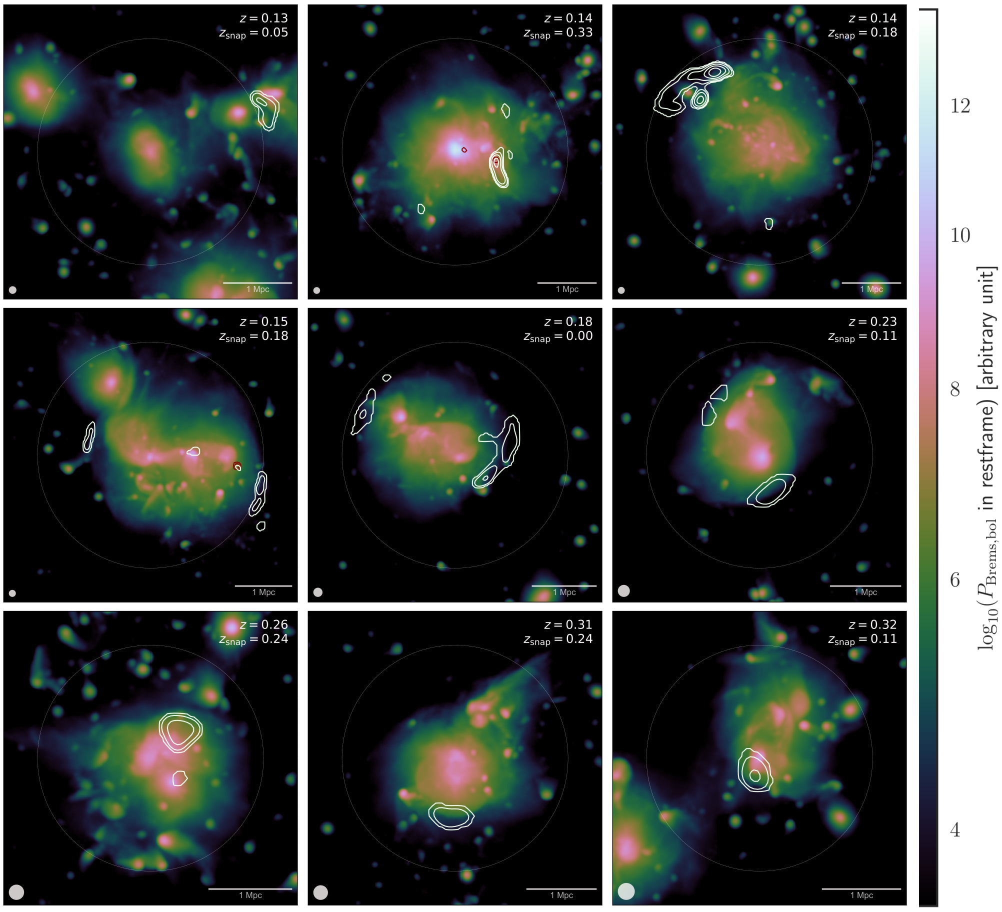

FIGURE 3.5: A variety of simulated relics chosen from the simulated MUSIC-2 sample, ordered from left to right, top to bottom with decreasing redshift: Emission from the NVSS-like survey is shown in white contours, red contours show emission subtracted with the Difference-of-Gaussians (DoG) image filter (see next section). Contours start at $2\sigma_\mathrm{rms}$ and spaced by a factor of 2. The background color denotes a simply approximation of the bolometric Bremsstrahlung emission due to Eq. 1.3.

We also create maps $\mathbf{m}_x$ of flux-weighted quantities x, which we use to get insights on the ICM densities, Mach number and integrated spectral indices for the synthetic radio relic population at a whole, used in Sec. 3.3.4. For all N particles within a pixel we take the flux weighted sum of the searched quantity x

$$\overline{x} = \frac{\sum_i^N x_i S_i}{\sum_i^N S_i}, \tag{3.15}$$

and convolve the resulting map $\mathbf{m_x}$ with the restoring beam $\mathbf{k}_{\mathrm{beam}}$ equivalent to Eq. 3.14. In order to retrieve the flux-weighted quantity for the *whole* relic, we now average over every pixel j within the relic

$$\overline{x}_{\mathrm{relic}} = \frac{\sum_{j \in \mathrm{relic}} \overline{x}_j S_j}{S_{1.4,\mathrm{relic}}}. \tag{3.16}$$

For the integrated spectral index α_{int}, we use an empirical model to impose an additional error on the measurements of the simulated radio relics. Using the average measurement uncertainty we corrupt the simulated integrated spectral index of a relic by a random value chosen from a Gaussian with standard deviation 0.1.

3.3 The NVSS to MUSIC-2 Comparison

In Nuza et al. (2017) we first presented a comparison of NVSS and MUSIC-2 radio relics. We further elaborate on this work by extending one some of the properties described in the Cha.2. Within this section we assume $B_0 = 1\ \mu$G, $\kappa = 0.5$ similar to Nuza et al. (2017). The values initially used for B_0 and κ are motivated by the rotation-measure-based B-field measures in the Coma cluster (Bonafede et al., 2010) and are also supported by measures of the central magnetic field strength in the center of several galaxy clusters (Govoni et al., 2017, Fig. 14, Fig. 15). In simulations like Kunz et al. (2011); Marinacci et al. (2018) a similar scaling of magnetic field strength with density $\kappa \sim 0.5 - 0.7$ is found. Because we implemented magnetic field amplification through compression and parameterize B by upstream density (Eq. 3.10) the same B_0 in this work will correspond to a higher downstream magnetic field strength than in Nuza et al. (2017). To balance this effect and obtain a comparable radio relic number count we adopt a 60 percent lower efficiency $\xi_e = 2 \cdot 10^{-5}$.

Both Fig 3.6 and Nuza et al. (2017, Fig. 15) are key plots to understand the incompleteness of the NVSS radio relic sample and its impact on models of mock observations. The reason for a deviating count of clusters with relic detections can very complex and due to several influences. One, however, can draw some

TABLE 3.2: Comparison of parameters used for the synthetic survey in this work and Nuza et al. (2017)

Symbol	Parameter	Nuza et al. (2017)	This work
f_{sc}	fractional sky coverage	0.82	0.82
ξ_e	energy fract. in supra-thermal e$^-$	$5.0 \cdot 10^{-5}$	$2.0 \cdot 10^{-5}$
B_0	reference B at $n_{\mathrm{e}} = 10^{-4}$	0.8 μG	1 μG
	reference density n_{e}	downstream	upstream
κ	exponent of B-density scaling	0.5	0.5
ζ	exponent of compressive B-ampl.	-	0.85

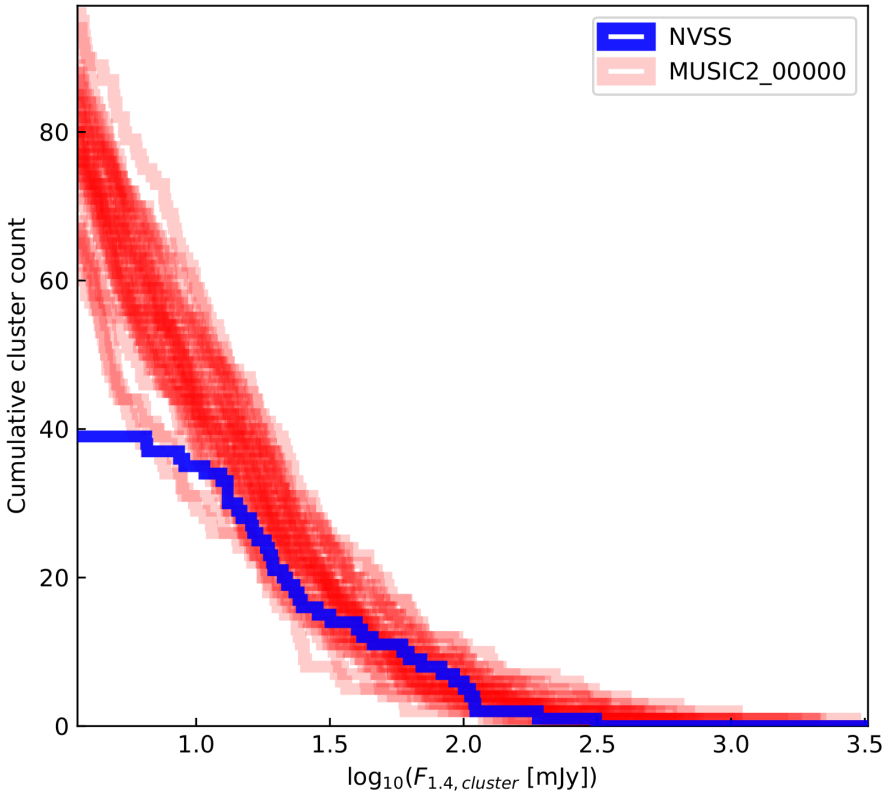

FIGURE 3.6: Plotted is the cumulative count of clusters with relic detections of total flux density $S_{1.4,\mathrm{cluster}}$ for NVSS *(dark)* and 36 realizations of the synthetic survey with the model parameters from Tab.3.2 (MUSIC-2, *bright)*. Note that the simulation exhibits a variable count which stems from the stochastic nature of galaxy cluster selection and projection. It also shows a larger fractions of clusters with a radio flux close to the detection threshold. This supports the idea the NVSS is incomplete towards clusters with fainter radio relics.

conclusions from the previous diagnostic plots. In clusters with low radio (and X-ray) flux, relics are less likely found in NVSS than in its MUSIC-2 equivalent. Because we attempt a statistical comparison we will have to account for this effect. Without any additional measures there will be many more relics in clusters with a low flux in the synthetic survey than in NVSS (Fig 3.6).

3.3.1 Radio relic selection by their morphology

Quantitatively MUSIC-2 includes more 'roundish' and small objects than NVSS. In Nuza et al. (2017) we used a distinction between elongated and 'small-roundish' relics to reduce the discrepancy between the number counts of relics in the survey and simulation. We acknowledge the importance of controlling our sample of simulated shocks. Therefore, we further iterate on methods to to constrain the number of detected relics in the synthetic sample to match observations. In Nuza et al. (2017) we identified three possible reasons for this: i) spurious shocks in the simulation due to the shock-detection scheme, ii) additional clumping resulting from missing radiative physics, and iii) real detection bias in NVSS.

Removal of spurious shocks with image filters

We attribute spurious shocks to compact agglomerates of SPH particles in the simulation. In the image they should show up as bright, compact regions within the galaxy cluster. We remove these regions by applying a mask in the image plane that is derived from a DoG image (Fig. 3.7). This method stems from the field of computer vision (Young, 1987) and leverages Gaussian image filters F_σ: Two instances of the same image $I_\sigma = I * \mathrm{F}_\sigma$ at different resolutions σ_1,σ_2, with $\sigma_2 > \sigma_1$ are subtracted from each other. The normalized difference image:

$$I_{\mathrm{DoG,norm}} = \frac{I_{\sigma_2} - I_{\sigma_1}}{I_{\sigma_2}} \tag{3.17}$$

can be thresholded to attain a blob detector (Schowengerdt, 2007). Sources which appear as point-like below a resolution of σ_2 and above a resolution of σ_1 are detected detected as blobs. The more similar σ_1 and σ_2 are, the more responsive is the DoG algorithm to only a certain scale. We use Gaussians of 20 kpc and 60 kpc FWHM to filter bright shocks that are below $\sim$ 50 kpc in size. Specifically, we reduce the flux density of regions $I_{\mathrm{DoG,norm}} > 0.75$ by 80 percent and apply this procedure a second time.

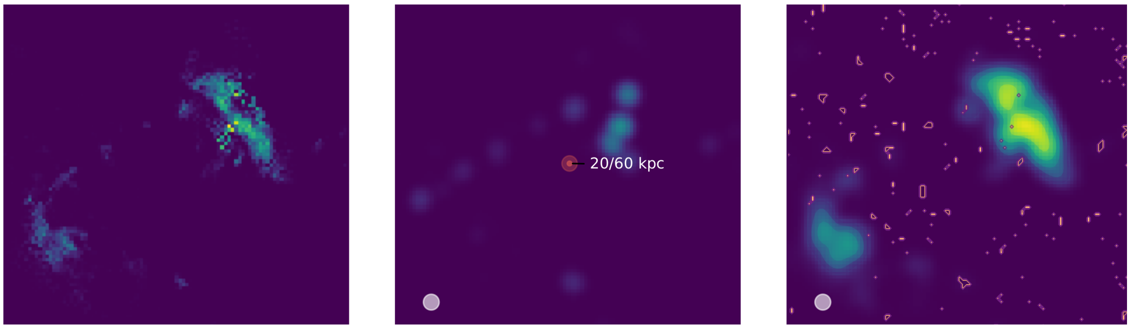

FIGURE 3.7: Effect of the DoG-filter on a typical simulated galaxy cluster with compact and extended radio emission: Shown are raw simulation **(left)**, the removed emission at synthesized resolution **(middle)**, and the synthesized image after application of the mask (filled contours) due to $I_{\mathrm{DoG,norm}}$ **(right)**.

The threshold is specifically chosen for the MUSIC-2 simulation and based on our own assessment of the high-resolution images (left panel Fig. 3.7) to decide which shocks are spurious and which not. Because the Difference-of-Gaussians filter can leverage the full resolution of the simulation, this method gracefully handles the source confusion that might arise from using a shape based filter of sources at NVSS-like resolution as used in Nuza et al. (2017). From comparing the synthetic image with and without the DoG-filter we can conclude that while the DoG technique marginally decreases the number of compact relic detections and faint relics it cannot account for the full discrepancy of observed and simulated radio emission - at least not if we leave the shocks from the simulation that are very likely physical untouched.

In Nuza et al. (2017) we reasoned that the compact objects are most likely "a combination of the simulation technique and the lack of energy feedback in [the] simulations." Since then we further iterated on the question if additional radiative physics within the simulation leads to less compact emission: Skillman et al. (2013) find that independent of the implemented radiative physics simulations produce essentially the same radio relic populations. This is why Skillman et al. (2013) prefer to use the adiabatic over radiative simulation. Through our own experiments (see App. B) we come to the same conclusion as Skillman et al. (2013): Radio relics should be predominantly produced in the outskirts of galaxy clusters - regions whose thermal properties are only negligible affected by cooling. We add the notion that radiative simulations that include AGN-feedback can have even more spurious, compact shocks and for brevity use the adiabatic MUSIC-2 simulation henceforward.

Removal of compact relics

Examples of NVSS radio relics only being recently discovered are PSZ1 G200 (Kale et al., 2017), RXC J0225 (Shakouri et al., 2016), and A3527-bis (de Gasperin et al., 2017) - making it clear, that the sample of radio relics detectable in NVSS is very likely incomplete. To correct for this, we aim at identifying morphological differences between the radio relics of synthetic and NVSS-based samples. The most simple morphological parameters that can be compared are shape s and LAS. On the logarithmic LAS-shape distribution we apply a Principial Component Analysis (PCA) to find the axis of largest variation for NVSS and MUSIC-2 radio relics. A PCA finds the orthogonal projections (components) of the data which are linearly uncorrelated from each other and by that identifies the projections along which the variation is maximized. The first principal component explains 88 percent of the variance in the data. Along this first principal component NVSS and MUSIC-2 relics show a strong separation from each other. The result is shown in Fig. 3.8. Note that a PCA on another MUSIC-2 sample would yield very similar principal components. As our goal is to exert control over the sample of compact simulated relics we introduce a probability p_{select} for each radio relic to be considered in the final survey, parameterized by logistic function:

$$\begin{aligned} p_{\text{select}} &= \frac{1}{1+\exp(-x)} \qquad (3.18)\\ \text{with} \quad x &= (\text{PC1} - b_{\text{pca,filter}})/a_{\text{pca,filter}} \\ \text{and PC1} &= 0.584(\log_{10}(\text{LAS}[']) - 0.451) \\ &\quad - 0.812(\log_{10}(s) + 0.469) \qquad (3.19) \end{aligned}$$

with b parameterizing the point where the object detection is only about 27 percent complete (with larger b indicating a less complete sample) and a setting the ‘width’ of the transition. For this chapter we use $a_{\text{pca,filter}} = 0.08$ and $b_{\text{pca,filter}} = -0.08$ as subjectively chosen best-guesses for those values. Like the LAS-shape-based cut in Nuza et al. (2017) this helps to balance the sample of compact radio relics but allows a continuous transition towards the compact end of the radio relic population. Note that for $a \rightarrow 0$ the function turns into hard cut in parameter space similar to the one used by Nuza et al. (2017). With this method we are able to correct the cluster counts and relic morphological statistics (Fig. 3.9), thereby increasing the similarity of the synthetic distribution with NVSS in LAS-flux-shape space.

To conclude, because we use the same simulation as Nuza et al. (2017) and can only theorize on the cause for the overabundance of small and roundish radio relics, we

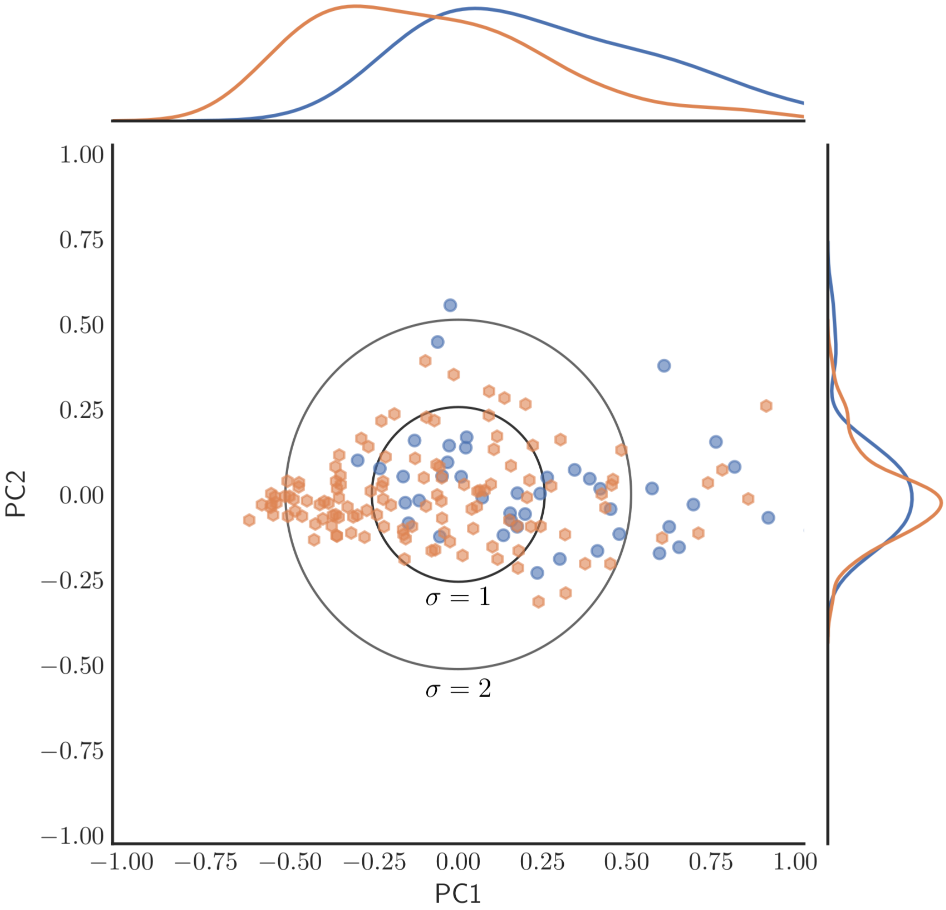

FIGURE 3.8: Principal components of the PCA applied on the NVSS (blue) and MUSIC-2 (orange) sample in the LAS-shape space.

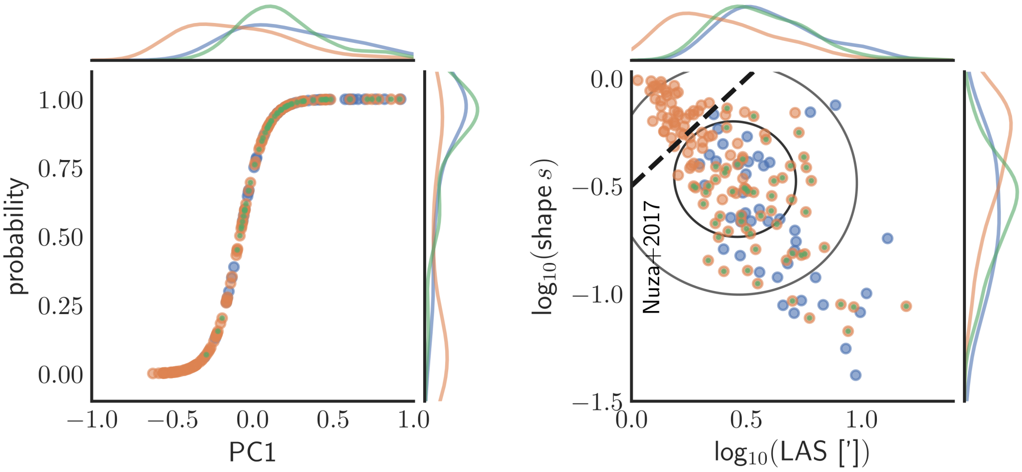

FIGURE 3.9: Detection probability distribution **(left)** and LAS-shape distribution **(right)** of NVSS relics (blue) and MUSIC-2 relics before (orange) and after (green) stochastic filtering. The circles denote the points that are projected to one and two-times the unit-variance.

will have to consider it as a part of the model specific behavior. We do, however, account for this behavior in two ways: Firstly, we use a DoG-filter to remove for spurious shocks. Secondly, we describe the detection probability p_{select} of the relics in the synthetic survey with a logistic function. The function is applied on the first principal component derived from the relic distribution in shape-LAS plane. For each galaxy cluster a number randomly drawn from the interval [0,1] is used to decide which synthetic relics are selected for the survey sample and which not.

3.3.2 About the MUSIC-2 host clusters of synthetic relics

We get useful insights by investigating the parameter plane that is often used to identify the Malmquist bias: For cosmological surveys this bias is most visible in the $P - z$ plane. Because cluster mass and radio relic luminosity are correlated in NVSS (Fig. 2.8) we alternatively investigate the bias in the $M - z$ plane (Fig. 3.10). This depiction helps us to understand what the effective similarity of galaxy clusters of the NVSS relic sample and the synthetic sample is.

MUSIC-2 and NVSS clusters with relic detections follow different trends: There is an overlap of both in the redshift range $z = 0.15 - 0.3$. At redshifts below $z = 0.15$ NVSS detections belong to galaxy clusters that are *less* massive than the central galaxy clusters in MUSIC-2. Clusters in our simulated sample, in this regime, are in general very massive and not representative for the NVSS-clusters. For redshifts above $z = 0.3$ NVSS detections exists in galaxy clusters that are *more* massive than the simulated ones. At this point we know, that due to the selection bias, different biases in the clusters masses exists.

From Fig. 3.10 we can conclude that for NVSS-like synthetic surveys it is sufficient to only consider simulated clusters that fulfill the empirical criterion:

$$\log_{10}(M_{200}/\mathrm{M}_{\odot}) > 13.6 + 2z_{\mathrm{cl}} \, . \tag{3.20}$$

Using this simple cut reduces the number of sampled MUSIC-2 clusters within the redshift range $0.05 - 0.70$ by about 70 percent. We employ this cut in the following sections to boost the speed of any mock-simulation (along with the measures described in Appendix D).

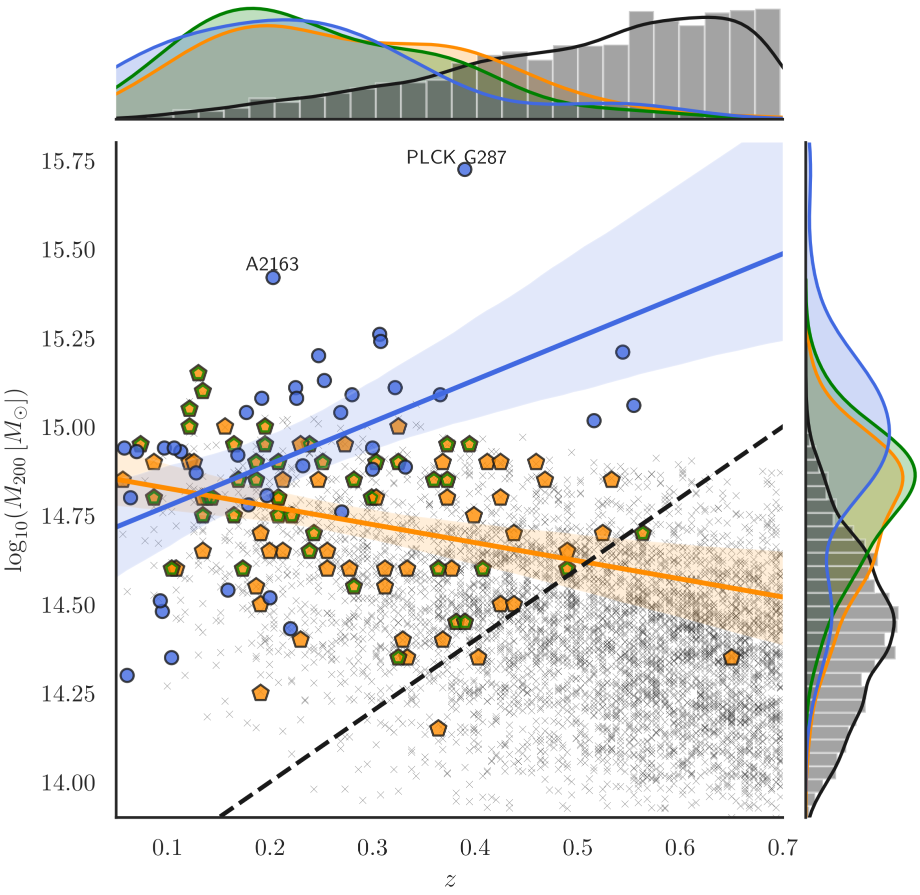

FIGURE 3.10: Scatterplot of cluster masses over redshift for NVSS relic-hosting clusters (*blue circles*) and MUSIC-2 clusters of a typical synthetic sky survey. Also denoted are all sampled MUSIC-2 clusters (*small, gray crosses*), those clusters hosting relics without the filter described in section 3.3.1 (*orange pentagons*), and the clusters hosting relics after applying the filter (*thick green borders*). The normalized occurrence rate of each type of clusters is added on the x and y axis. While the simulated clusters span a wide range, clusters with relic detections populate a different area. NVSS clusters at low redshifts span a wider redshift and mass range than MUSIC-2 clusters with relic detections. The regressions with shaded 68 % confidence interval show, that the distributions follow different trends. The empirical cut of Eq. 3.20 in cluster mass is denoted with the dashed black line.

The upper NVSS outliers are A2163 at $z = 0.20$, and PLCK G287 at $z = 0.39$.

3.3.3 Relic scatter plots

We will leverage the statistics shown in Sec. 2.4 to compare NVSS with the synthetic survey (Fig. 3.11). Depending on the compared quantity the DSA model from thermal pool electrons gives a good result with the assumed set of parameters (Tab. 3.2). At this point it is however not clear, if a match to all observed properties is possible with this model. We reproduce the strong correlation in $P_{1.4,\mathrm{rest}}$−LLS from Sec. 2.4.1, Eq. 2.12. By constructing a synthetic survey with different sensitivities (Fig.3.12) we show that the exact normalization of this correlation largely depends on the survey sensitivity. This is important, because it reveals that any regression on quantities in surface-brightness limited surveys is prone to selection biases.

3.3.4 Averaged physical quantities of MUSIC-2 relics

The advantage of the synthetic survey over NVSS is that we can easily investigate the physical quantities that are linked to the radio emission. Fig. 3.13 shows the physical quantities for one mock survey with aforementioned model parameters. It reproduces NVSS-like relics quite well in most quantities but the distance. The smoothed particles downstream have temperatures $T \sim 7 - 20\,\mathrm{keV} > 7\,\mathrm{keV} = T_0$ and densities $n_\mathrm{e} \sim 10^{-3}\,\mathrm{cm}^{-3}$. Partially, this is the immediate effect of compression, as the flux-averaged Mach numbers are quite high ($\mathcal{M} = 3 \ldots 6$). While the average relic area is around $0.1\,\mathrm{Mpc}^2$ all other quantities are, in average, larger than the normalizing quantities used in Eq. 3.8. This explains, why for this particular parameter set, relics with radio powers $\gtrsim 10^{24}\,\mathrm{W/Hz}$ are simulated.

In summary, the analysis shows that higher relic luminosities are mostly related to the following quantities, in increasing order of importance (absolute value of Pearson-correlation): temperature T, density n_e, area A, and, by least, the Mach number. Colafrancesco et al. (2017) argue that the absence of any correlation between radio power and Mach number indicates that the radio relic properties are mainly governed by the pre-existing CR electron population. Fig. 3.13 shows that a missing correlation in $\mathcal{M}$ and $P_{1.4}$ can arise in radio relic models without any pre-existing CRes, possibly from an interplay of relic projection and selection effects. We therefore reject the statement of Colafrancesco et al. (2017) on concrete insights on the pre-existence of CRes in the ICM arising from a lack of this correlation.

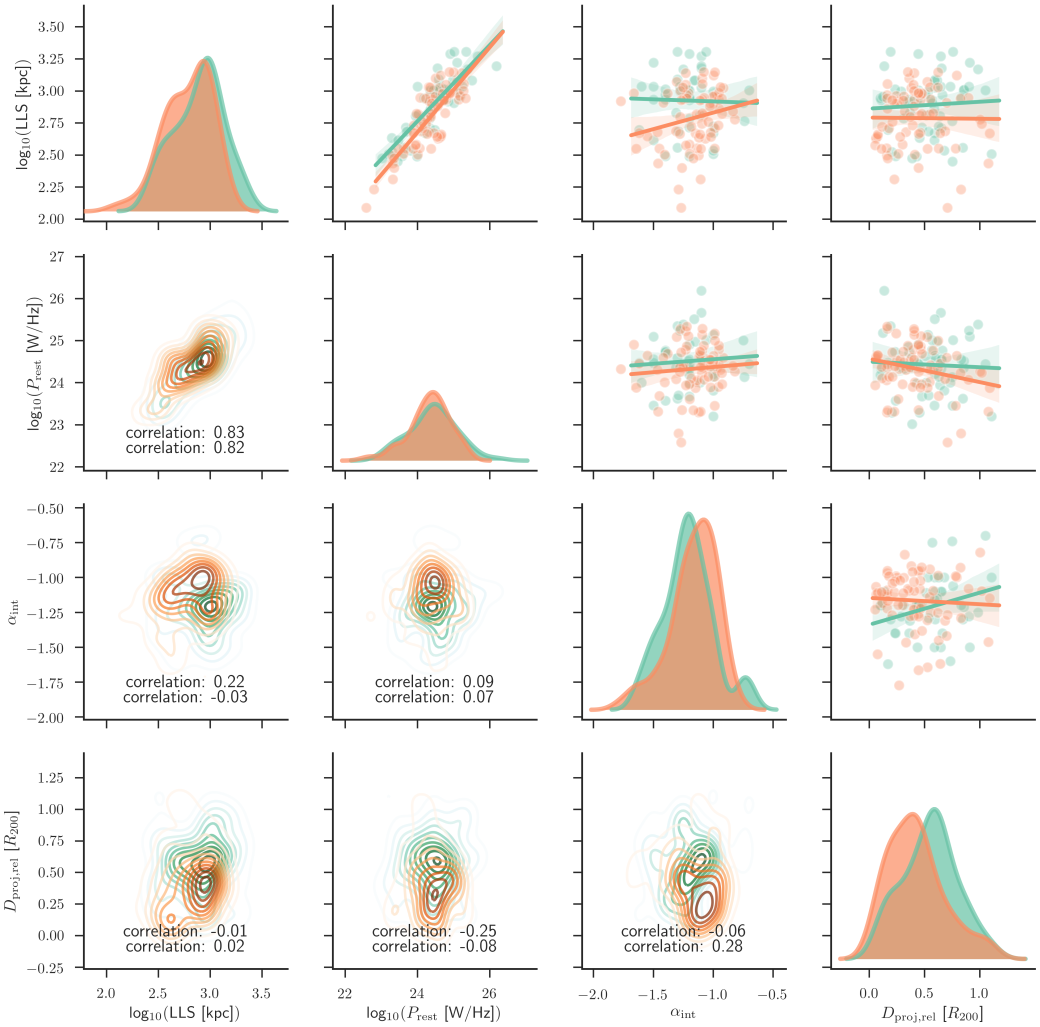

FIGURE 3.11: A comparison of relic properties measured in NVSS (*green*) with the synthetic survey based on model Tab. 3.2 (*orange*): Shown are the linear regression with 1σ confidence shaded area (**upper right**) and the KDEs for one (**central diagonal**), and two parameters (**lower left**). Both surveys match well in power and size but remain with a discrepancy in the integrated spectral index and distance to the cluster center.

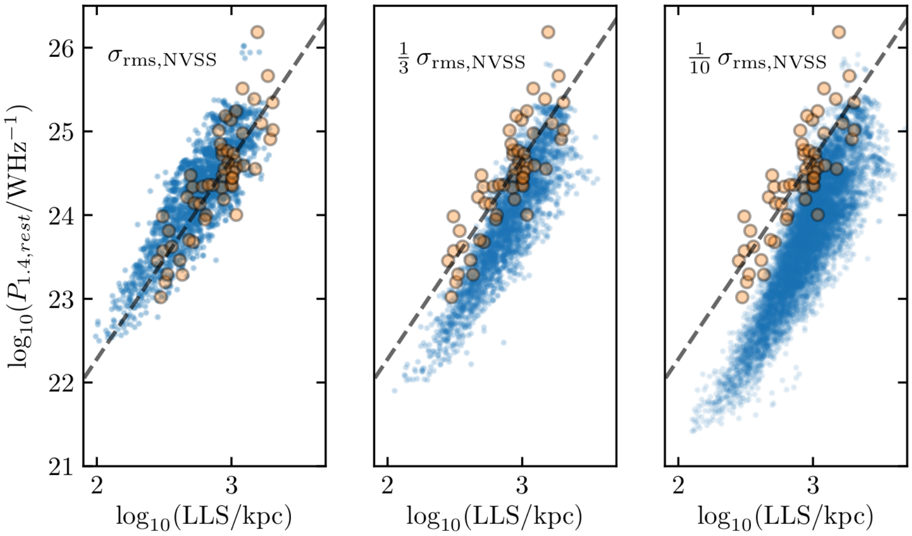

FIGURE 3.12: Shown is the $P_{1.4,\rm rest}$-LLS distribution of relics in NVSS (*orange*) and for a synthetic survey with three different survey sensitivities (*blue*, 36 realizations each).

3.3.5 The averaged projected relic in MUSIC-2

Both in the scatter-matrix and in the comparison of the average projected relic (Fig. 3.14) we see that the model attributes more relic emission towards the inner 0.5 R_{200} of the galaxy cluster (Nuza et al., 2017) than NVSS . In the analysis of twenty merging galaxy clusters Vazza et al. (2012, Fig. 4) found the peak synchrotron emission at 0.5 $R_{\rm vir} \equiv 0.6\,R_{200}$ for similar magnetic field assumptions as those in this work. While this is more in line with the findings of NVSS, their analysis makes simpler assumptions about the selections of clusters and relics.

One of the questions we want to answer is that if a fine-tuning of the model parameters is able to bring the distance of radio relics in agreement with observational data. In Fig. 3.14 we see the effect of changing κ towards values that favor strong magnetic fields and hence brighter radio relics in the cluster outskirts while keeping B_0 and ξ_e fixed. While more overlap can be achieved at $\kappa = 0$ it is clear that a homogeneous magnetic field strength stands in conflict with the empirical evidence (Sec. 3.2.3). Our findings confirm that simulated relics differ from observed ones, i.e. they are found in greater proximity to their host cluster (comp. Fig. 3.14). One might argue that adiabatic HD-simulations of thermal-pool DSA relics are insufficient to provide a population of relics that peaks at the cluster distance of 0.6 R_{200}. It is therefore worthwhile to assess if the full available parameter space yields solutions that match the NVSS radio relic population in its key features.

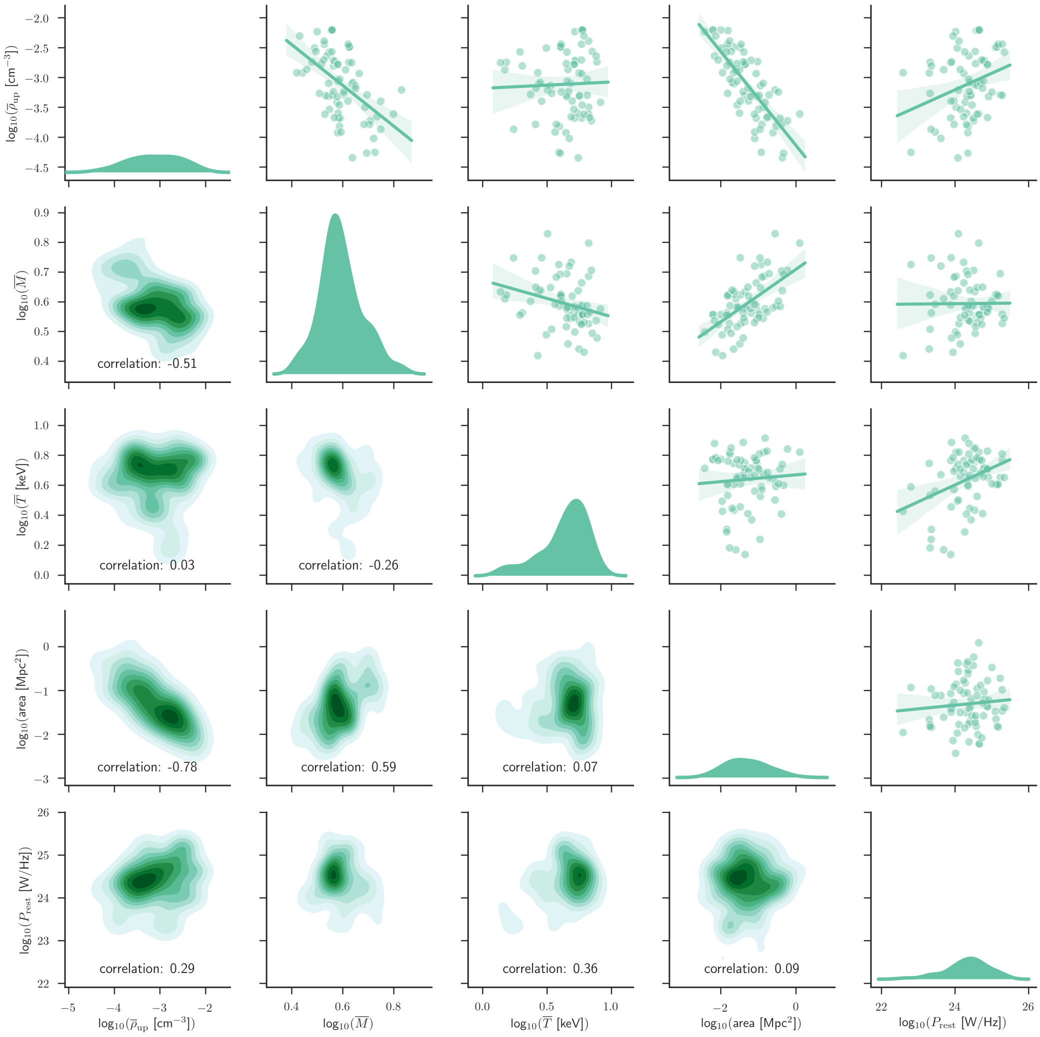

FIGURE 3.13: Scatter matrix of the flux averaged physical quantities used in Eq. 3.8 to compute the shock radio emissivity for the same model parameters as in Fig 3.11: Shown are the linear regression with 1σ confidence shaded area (**upper right**) and the KDEs for one (**central diagonal**) and two parameters (**lower left**).

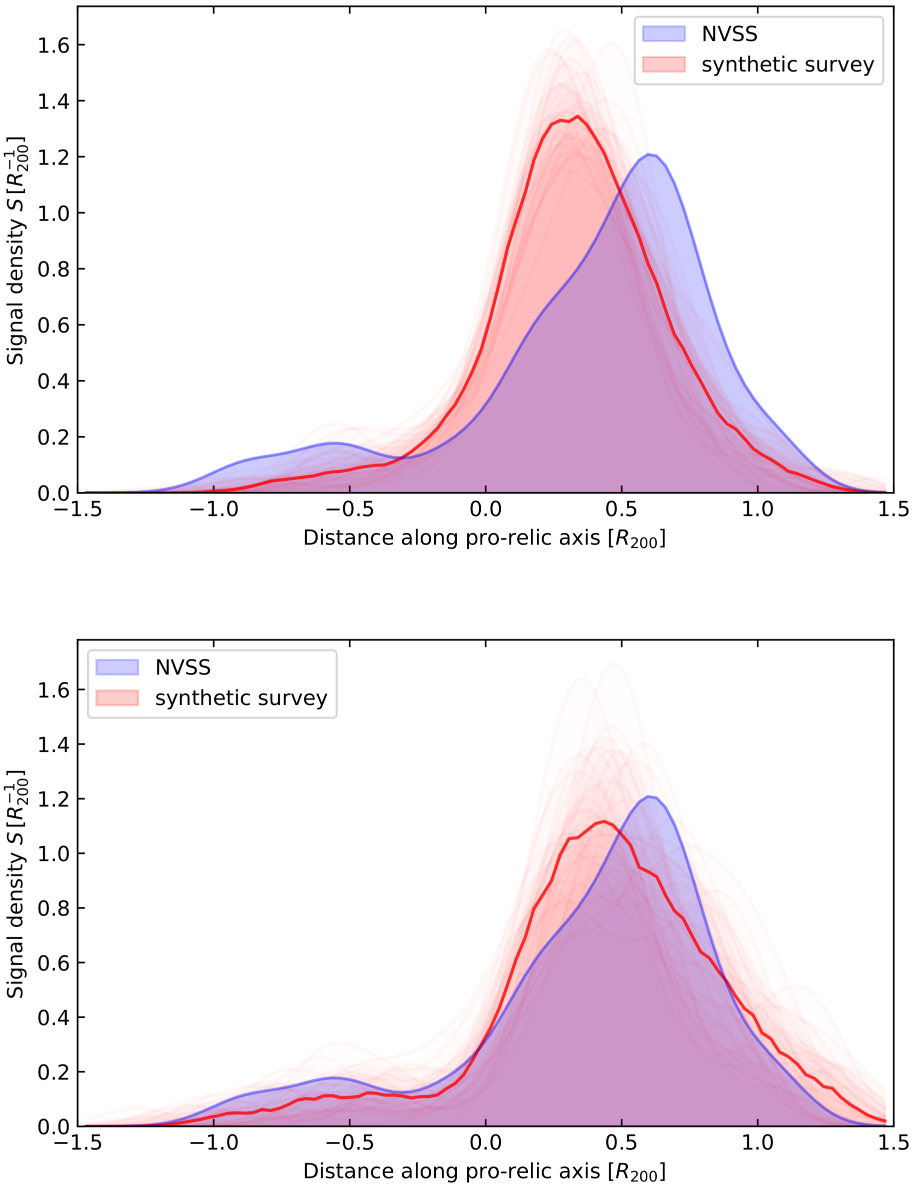

FIGURE 3.14: Shown is the average projected radio relic for the MUSIC-2 simulation with the parameters described in this section (**top**) and with a magnetic field density scaling of $\kappa = 0$ (**bottom**) for 36 runs each. The median signal of the synthetic survey at given distance is denoted as the thick red line. As the magnetic fields becomes more homogeneous more relic emission is found in the cluster outskirts. For a $\kappa = 0$ the peak of NVSS is however not fully recovered.

3.4 Summary

We described how we updated the scheme of Nuza et al. (2017) to create a mock survey based on the hydrodynamical simulation MUSIC-2. The simulated volume is smaller than the volume observed by the synthetic survey. Sampling bias will be present. We implement several measures to improve on the realism of the used simulation and the features of the synthetic radio relic population:

- To each simulated galaxy cluster we assign a galaxy cluster snapshot and project the observed quantities along a random direction, taken from one subvolume of $2R_{200}$.
- The MUSIC-2 adiabatic simulation shows shocks from small substructures that we do not consider to occur in more sophisticated simulations of the ICM. We apply a Difference of Gaussians (DoG) filter to remove spurious signal. A relative overabundance of compact relics in MUSIC-2 remains.
- Applying a probabilistic selection function of radio relics based on data projected towards the first principal component in the LLS-shape space allows one to create a synthetic survey which is similar to NVSS in the relic morphological statistics. With the probabilistic selection, this model expresses the assumption that faint and compact relics have a detection probability significantly lower than one. One bias that we consider unaddressed in the mock survey is a bias in the sampled mass-range of galaxy clusters.

Investigating the relic statistics reveals that a reasonable match of observed and synthetic sky survey would need to change the model so that it would to lead to relatively more detections of bright radio relics at $0.6R_{200}$. We rebut the argument of Colafrancesco et al. (2017) that a missing correlation of radio power and integrated spectral index must go along with a significant contribution of pre-existing CRes to the radio relic emission. As the employed model has many ill-constrained parameters, we deem it important to search the existing parameter space for the best possible solutions. We will focus on the physical parameters (ξ_e, B_0, and κ) as well as the selection bias $b_{\mathrm{pca,filter}}$.

Chapter 4

Approximate Bayesian Inference of Radio Relic Model Parameters

In Cha. 3 we described a model based on the cosmological simulation MUSIC-2 and asked if it is able to reproduce the observed NVSS relic population. In this chapter we infer the best matching parameters of the radio relic model brought up in the last chapter. We explain why we use approximate Bayesian computation for parameter inference in Sec. 4.1, describe its implementation in Sec. 4.2. In Sec. 4.3 and Sec. 4.4 we show the inferred parameters of this analysis and assess their implications on the origin of radio relics.

4.1 Parameter inference on population models

Population models yield statistics on the properties of single entities. Those statistics allow us to incorporate native measures of physically disconnected objects, like radio relic, into the model inference. The inference, however, comes with its own methodological requirements. The scheme of parameter inference that one can apply is sensitively linked to the problem description.

4.1.1 About Bayesian Inference and its limitations

The *Bayesian theorem* describes how to update the probability of a hypotheses, given the evidence and already existing (prior) knowledge:

$$P(\text{hypothesis}|\text{evidence}) = \frac{P(\text{evidence}|\text{hypothesis}) \cdot P(\text{hypothesis})}{P(\text{evidence})} \tag{4.1}$$

Put into the context of parameter inference for scientific models, one can infer the posterior probability density function (PDF), also called the posterior distribution $P(\theta|\mathcal{D})$ of the parameters θ of a given model from the data $\mathcal{D}$:

$$P(\theta|\mathcal{D}) = \frac{P(\mathcal{D}|\theta)\, P(\theta)}{P(\mathcal{D})}\,. \tag{4.2}$$

It is derived from the conditional likelihoods $P(\mathcal{D}|\theta)$, the prior probability $P(\theta)$ of the model, and the marginal likelihood $P(\mathcal{D})$ that we already know as *evidence*. This theorem allows one to seamlessly combine prior knowledge with new observations. In addition, it provides a probability density instead of a point estimate of the most probable case, as retrieved by maximum likelihood approaches.

In the field of parameter inference the Bayesian method has found strong approval due to its ability to optimize the inferred quality by both using the maximal support of data and minimizing the bias, which only leaves it to the predictive power of the model to reproduce the data. It, however, comes with its own methodological requirements. It is only applicable to models that can be described by Markov chain processes of the exponential family - which includes Gaussian (noise) processes. This is for example the case if an image is corrupted by Gaussian noise or a power spectrum by pink noise. This assumption, however, often is violated once more complex processes are at play and lead to a likelihood function that is hardly traceable.

A set of *likelihood-free* techniques has been developed to address this issue and allow the parameter inference on a wider range of models. Likelihood-free parameter inference techniques are listed as one of the key methods that will be used to advance cosmology in the 2020s (Paul et al., 2019). Approximate Bayesian computation (ABC) is one of those techniques.

4.1.2 Approximate Bayesian Computation

Approximate Bayesian computation (ABC) was introduced by Tavaré et al. (1997) and J. K. Pritchard et al. (1999) to allow estimating the posterior distribution $P(\theta|\mathcal{D})$ if the likelihood $P(\mathcal{D}|\theta)$ is not analytical derivable. It is based on the idea, that any model realization drawn from the true posterior probability density will lead to data similar to the ones observed. Finding the true posterior probability density now becomes a question of finding models that reproduce the observations in their key properties. Specifically, one can draw realizations from the prior and only accept those trials that resemble the observation the best. The distribution of the accepted trials in the model parameter space will allow an *approximation* of the true posterior distribution. Depending on the employed scheme the approximation of $P(\theta|\mathcal{D})$ can be very close to the real posterior.

The workflow of creating an ABC method is as follows: First one defines parameters θ_i of a forward model M with output $O(M,\theta)$. This is followed by defining the distance metric $\Delta(O,D)$ to compare O of the forward model with available data $\mathcal{D}$. Lastly, one has to choose the acceptance interval ϵ. The model trial $O(M,\theta)$ is accepted if:

$$\Delta(O_{\mathrm{M},\theta},D) \leq \epsilon \tag{4.3}$$

and else rejected. One example of ABC is shown in Fig. 4.1. We show this example, because for this particular case we can estimate the true posterior through Bayesian inference and confirm that the ABC estimate is in the best case exact (see Appendix C). Because of the statistical nature of the forward model, the output $\boldsymbol{O}$ and hence the metric distance $\Delta(\boldsymbol{O},\boldsymbol{D})$ can be different even for model realizations with the same parameters $\boldsymbol{\theta}$. This is why for a given $\boldsymbol{\epsilon}$ some model realizations close to the final posterior are discarded, while others which are further away are kept.

One of the challenges in ABC is to define the acceptance interval $\boldsymbol{\epsilon}$. While an acceptance interval that is wide will lead to a very poor estimate of the posterior distribution, a small $\boldsymbol{\epsilon}$ will require an extensive number of forward model realizations. There is, however, no need to keep ϵ fixed. *ABC sequential Monte Carlo* (ABC-SMC, Beaumont et al., 2009; Toni et al., 2009), also referred to as ABC population Monte Carlo (ABC-pmc) methods, are inspired by sequential Markov chain Monte Carlo (MCMC) approaches. There the estimate of the posterior distribution is iteratively improved and the acceptance interval ϵ shrunken iteratively. This allows ABC sequential samplers to decrease the number of required forward model trials with respect to simple ABC. Still ABC-pmc holds all favorable properties, allowing for convergence to the approximate posterior distribution density without the need to define any explicit conditional probabilities. The pseudo-code is shown in Algorithm **??**. Estimating the posterior probability density is done in every iteration and a key factor of efficient parameter sampling in ABC-pmc (Alg. **??**, line 13). We use an optimal local covariance matrix kernel (OLCM), where the posterior distribution is estimated locally by a variable number of model trials in the nearby parameter space (Filippi et al., 2013). This approach combines a high ratio of accepted to rejected model samples, i.e. the acceptance ratio, with a good exploration of the parameter space (Akeret et al., 2015).

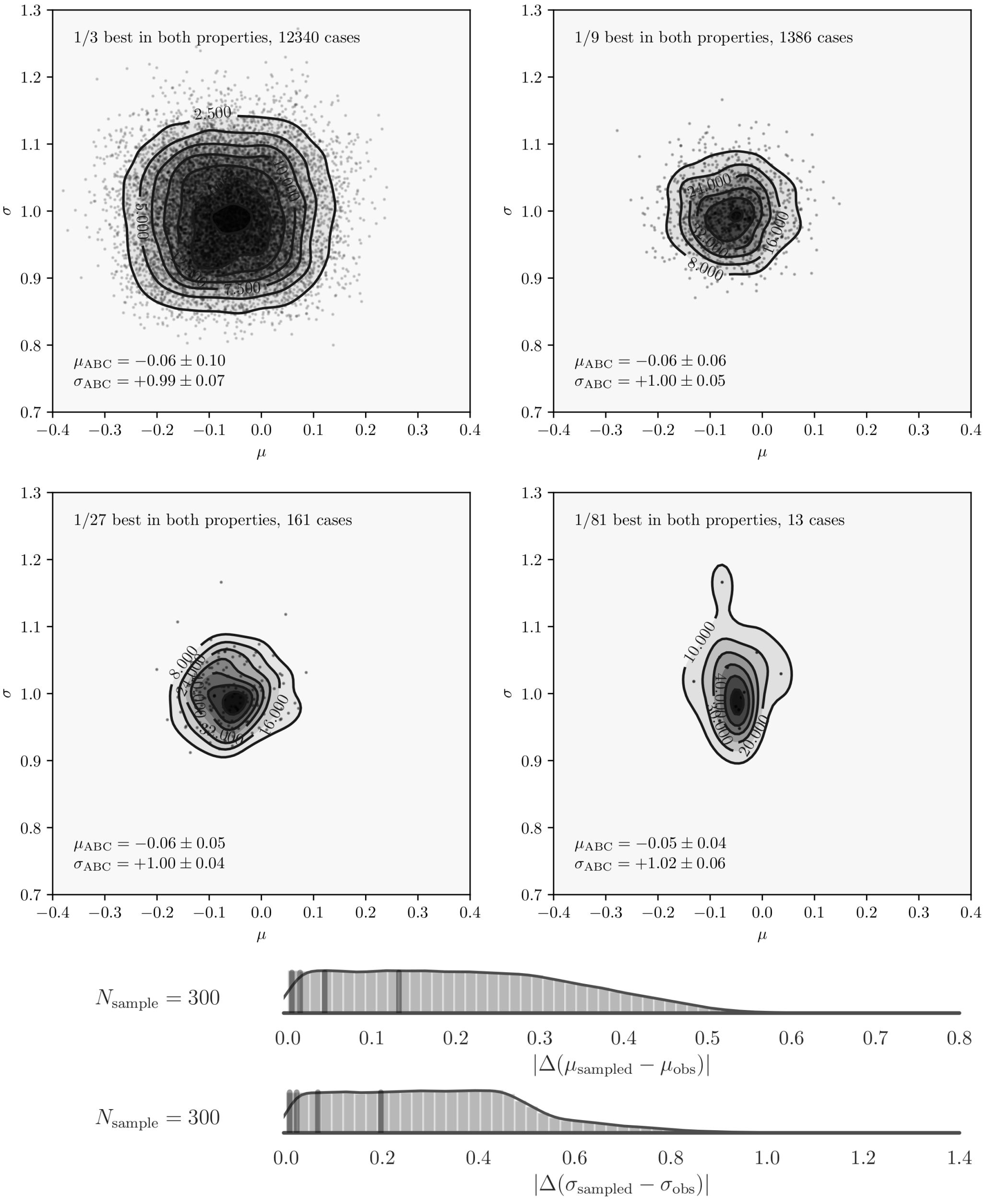

FIGURE 4.1: An example of ABC with $N_{\text{trial}} = 10^5$ model trials uniformly sampled from the shown parameter ranges: $N_{\text{sample}} = 300$ measures are sampled from a Gaussian distribution with $\mu_{\text{true}} = 0$ and $\sigma_{\text{true}} = 1$. For each trial, model parameters are sampled from $\mu_{\text{prior}} = [-0.4, 0.4]$ and $\sigma_{\text{prior}} = [0.7, 1.3]$. **Top:** From left to right, top to down are selected the 1/3, 1/9, 1/27, and 1/81 fractions of *model trials* with the smallest deviation from the *data* in terms of derived mean and variance. For this particular example the solution converges to the exact probability density function (PDF) when taking the models that belong to the 1/9 best in both criteria. The estimate of the posterior converges to $\mu_{\text{posterior}} = -0.06^{+0.06}_{-0.06}$ and $\sigma_{\text{posterior}} = 1.00^{+0.05}_{-0.05}$. More data, i. e. a larger N_{sample}, would yield a better constraint. We see that estimating the posterior with a limited number of model trials does impose a sampling error, which is most pronounced for the most restrictive threshold ϵ. **Bottom:** Shown are the KDE distributions of the differences in μ and σ with the selection criteria ϵ being indicated by a vertical line.

4.2 Building up intuition for ABC-pmc

In this section we describe a simple case of ABC-pmc-based inference on the NVSS data set to help the reader to develop an understanding of the strengths and caveats of this technique. We proceed to describe the metrics that we use for our inference.

4.2.1 Summary statistics and distance metrics

The basic idea of ABC is to compare the forward-model and the available data based on a set of measurements. Estimating the discrepancy between the observed and simulated data in a high-dimensional space is highly non-trivial. The subspace where both model and observed data overlap will shrink exponentially with the dimensionality of the data space. The number of required forward-model runs to get an accepted sample, in consequence, increases exponentially with the number of comparison criteria. This effect is called the *curse of dimensionality* and if not accounted for will make any analysis unbearably slow. It is hence a sensible measure to limit the number of compared criteria via dimensionality reduction techniques.

One of these ways is to use summary statistics. Summary statistics provide low-dimensional representations of the data that can be used in the metric $\Delta(O,D)$ which is a one-dimensional representation of the dissimilarity between model and data. The posterior distribution estimated by ABC will still converge to the real posterior distribution if one uses *sufficient* summary statistics (Casella and Berger, 2001; Robert et al., 2011). In the case of a Gaussian distribution of data these sufficient statistics are the mean and (co)variance - which we exploited in Fig. 4.1. These sufficient statistics, however, only exist if the likelihood of the data distribution can be described by the exponential family of distributions.

In all other cases the estimated posterior will be an approximation of the true posterior. The goal within any ABC procedure is not to find the *sufficient* but to find an *informative* summary statistics. The suitability of a metric for model selection can be described with the concept of Fisher information. It is a description for the amount of information an observed random variable caries about an unknown parameter θ. In practice one wants to choose a representation where the variance of the observed variable (of different forward-model outputs) is small relative to the differences caused by changing the model parameters. The choice of summary statistics always involves a trade-off between retaining as much Fisher information as possible while limiting the dimensionality of the metric (Aeschbacher et al., 2012). Advanced studies choose a number of linear combinations of summary statistics, that maximize the independence of the parameter estimates (Heavens et al., 2000). In our case we motivate the choice of the used metrics by sensitivity tests (see Sec. 4.2.3-4.2.2) - thereby focusing on explainable metrics rather then the highest possible model selection strength.

4.2.2 Fisher information of the used metrics

We explore which metrics are informative in our case, i.e. useful to further shrink the model parameter space. We therefore test in the sense of Fisher information, if the stochastic variation of the model is small compared to the variation of the data any model parameter. In preparation for applying the ABC-pmc procedure and the full set of physical model parameters we investigate how some the metric distance between NVSS and some models changes when varying ξ_e and κ.

Number count of relic hosting clusters: Δ_{count}

We base our first metric distance Δ_{count} on the relative difference in the number of clusters with relic detections

$$\Delta_{\mathrm{count}} = \frac{|N_1 - N_2|}{\sqrt{N_1 \cdot N_2}} \tag{4.4}$$

in both surveys. In our case, we use $N_1 = N_{\mathrm{cl,NVSS}} = 39$ and hence favor synthetic surveys with similar N_2. The metric distance ranges from $[0, \sqrt{\max(N_1,N_2)/\min(N_1,N_2)}]$. It is very straightforward to apply this metric Δ_{count}, yet it is sensitive to detection biases. As described in Sec. 3.3.1 we mimic detection biases in the synthetic survey through a probabilistic selection of radio relics, based on their size and shape.

While number count will be correlated with all parameters that have an influence on the number of radio relic detections, it is insensitive to the position and morphology of radio relics. We agree with Pinzke et al. (2013) on the notion that relic number counts alone are not sufficient to differentiate between different models of particle acceleration. It is, however, a way to normalize the efficiency ξ_e of the acceleration process with respect to the magnetic field strength (Fig. 4.2). In this example we see, that Δ_{count} is a very effective at discriminating between ξ_{e} up two a relative difference of less than 50 percent. We also see that κ also has an influence on the number of clusters with radio relic detections.

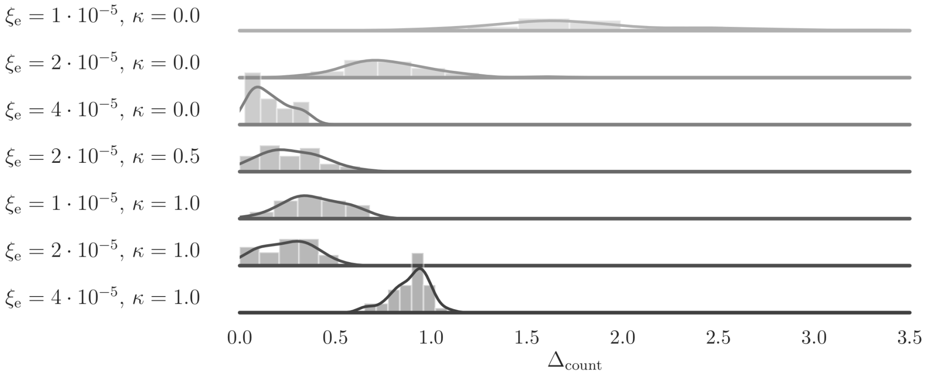

FIGURE 4.2: Shown is the distribution of the metric Δ_{count} for 36 samples smoothed by a KDE when varying the efficiency ξ_e and κ.

Power-LLS distribution: Δ_{2DKS}

Radio power and LLS are the strongest correlated pair of variables in our data. Like Δ_{count} this distributions depends on ξ_e but also shows an sensitivity to the magnetic field exponent κ, and the detection bias parameter $b_{\text{pca,filter}}$ (Fig.4.3). A two-dimensional two-sided Kolmogorov-Smirnov test (Peacock, 1983; Fasano and Franceschini, 1987)[1] returns the probability p_{ks} of the hypotheses that both samples

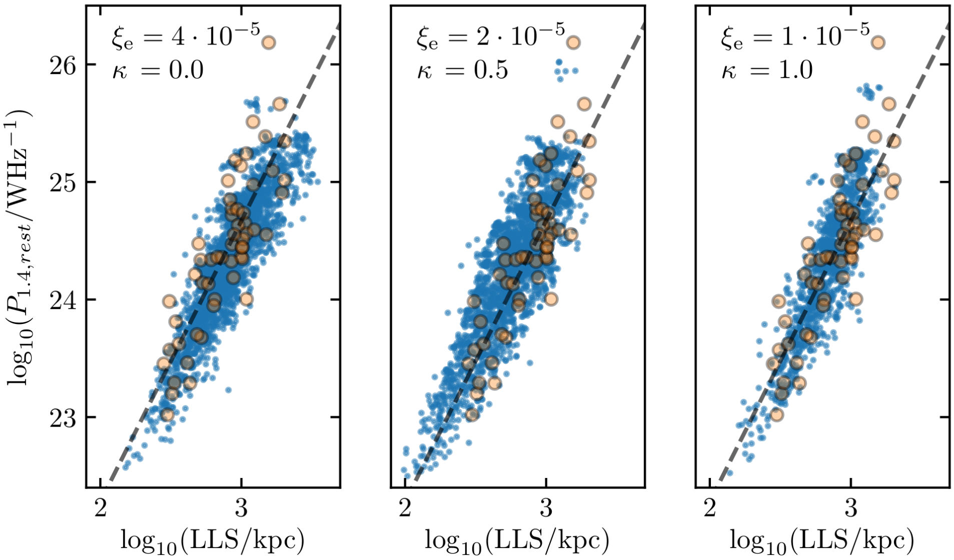

FIGURE 4.3: Shown is the $P_{1.4,\text{rest}}$-LLS distribution of relics in NVSS (*orange*) and MUSIC-2 sampled from three different model parameter sets each reproducing roughly the same number of radio relics (*blue*, 36 realizations each). The slope is influenced by κ, a larger κ leads to more compact relics. From Fig 3.9 we know that $b_{\text{pca,filter}}$ influences the number balance between small and larger radio relics.

---

[1] The fact that this is a strong correlation would allow to test for the correlation coefficient.

are drawn from the same distribution. Specifically, it computes the difference of the cumulative sums along the parameter axis/pair between the distributions. The supremum, i.e. largest occurring discrepancy is a statistical indicator for the similarity of both samples. The advantage of this test is that it works on small samples of continuous (i.e. unbinned) data points. While the one-dimensional test does not assumes a specific (i.e. Gaussian) distribution the two-dimensional makes an implicit assumption that this is the case. The test's wide applicability, however, comes at the cost of reduced discriminating power, being visible in the relatively large overlap between the different models (Fig. 4.4). We apply this test on the $P_{1.4}$-LLS distribution of radio relics. The metric

$$\Delta_{\mathrm{2DKS}} = 1 - p_{\mathrm{ks}}(D,O) \tag{4.5}$$

is sensitive to the total number of relics (Fig. 4.4) as well as to κ. The reason is that κ affects the slope of the $P_{1.4}$ and LLS correlation, while the distribution of relics along this correlation is mainly affected by the normalization of the electron acceleration efficiency ξ_e.

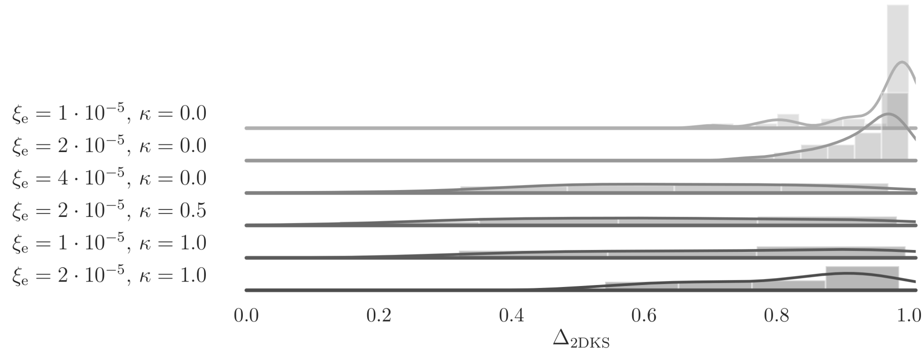

FIGURE 4.4: Shown is the distribution of the metric Δ_{2DKS} for 36 samples smoothed by a KDE when varying the efficiency ξ_e and κ. Note that the model $\xi_e = 4 \cdot 10^{-5}, \kappa = 1.0$ was removed from those plot as its density histogram would be very peaked at values of one and hence disturb the scale of the other plots.

The average projected relic: $\Delta_{\text{average relic}}$

In Sec. 2.4.3 we introduced the average projected relic in terms of distance of R_{200}. This statistic can be used to identify if the relics are found in the correct distance to the cluster center. In the Cha. 3, Fig. 3.14, we found that this summary statistics is sensitive to κ. The metric itself is the total difference of the smoothed radial profile of the average radio relic (Eq.2.20) derived from NVSS and the synthetic survey:

$$\Delta_{\text{average relic}} = \sum_i |S_{\mathrm{D},1}(r_i) - S_{\mathrm{D},2}(r_i)| \,. \tag{4.6}$$

Because the sum of all bins of S_D is strictly one (Eq. 2.18), this metric evaluates a similarity of two data-sets between zero and two. Note that the minimal reachable difference $\Delta_{\text{average relic}} \sim 0$ is not attained within the selected parameter sets. Lacking a parameter combination that leads to $\Delta = 0$ is a strong hint at a limited *expressiveness* of a model. Models which are to simplistic will only be able to reproduce a subset of summary statistics. With increasing complexity, a model is able to reproduce a larger set of possible observations. Trying to fit a model on criteria that it cannot reproduce, will bias the estimate of the other parameters in an unpredictable way.

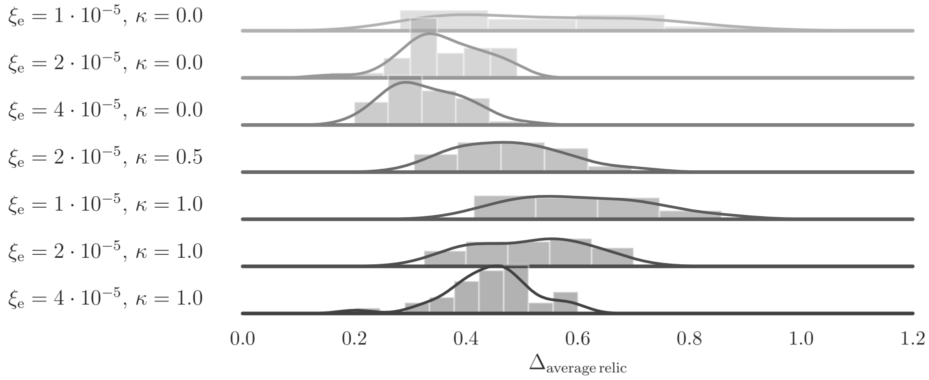

FIGURE 4.5: Shown is the distribution of the metric $\Delta_{\text{average relic}}$ for 36 samples smoothed by a KDE when varying the efficiency ξ_e and κ.

The average integrated spectral index: $\Delta_{\overline{\alpha}_{\text{int}}}$

In addition to the dissimilarity in average projected relic position we measured Mach numbers in NVSS that are slightly different than the ones derived from synthesized surveys (Fig. 3.11). We employ the difference of the arithmetic means of α_{int} of both samples:

$$\Delta_{\overline{\alpha}_{\text{int}}} = |\overline{\alpha}_{\text{int},1} - \overline{\alpha}_{\text{int},2}| \tag{4.7}$$

as a simple metric that encodes the effectiveness of particle acceleration for different Mach numbers. For our particular case with $\overline{\alpha}_{\text{int},1} = \overline{\alpha}_{\text{int,NVSS}} = -1.213$ (using the known α_{int} from Tab. 2.3). Investigating this $\Delta_{\overline{\alpha}_{\text{int}}}$ for the model selection (Fig. 4.6) reveals that it favors higher values of κ than $\Delta_{\text{average relic}}$. As the average Mach number

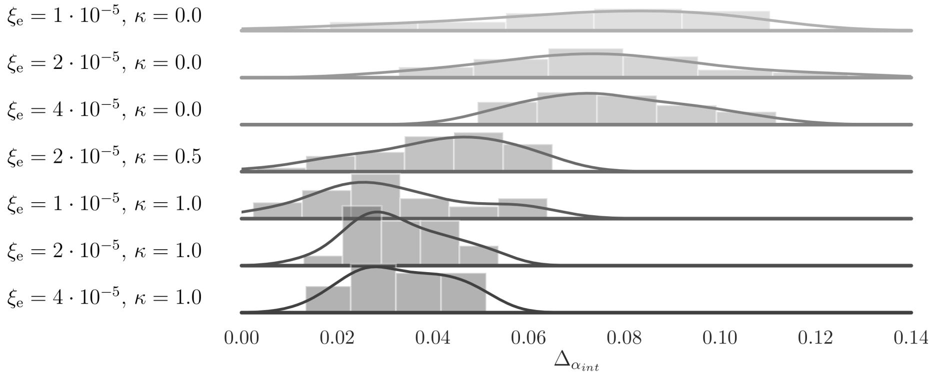

FIGURE 4.6: Shown is the distribution of the metric $\Delta_{\overline{\alpha}_{\text{int}}}$ for 36 samples smoothed by a KDE when varying the efficiency ξ_e and κ.

of shocks in clusters increases with larger distance both optimization criteria are antagonistic when selecting models (compare Sec. 4.2.2) - yet we have to reproduce relics that are farther out than the average simulation. Using both metrics for ABC results in a PDF which compromises between both.

4.2.3 Example: One free parameter, one metric

As a first trial of model inference on the NVSS dataset and the model of a synthetic survey introduced in Cha. 3, we test how our approach performs in the case of an unknown ξ_e. We set a uniform prior in the logarithmic space for ξ_e bounded within $[-7, -4]$. All other variables of the used model remain fixed:

- survey completeness $p_{\text{compl}} = 0.82$ (Eq. 3.6),
- magnetic field normalization $B_0 = 1\,\mu$G, density scaling exponent $\kappa = 0.5$ (Eq. 3.10), enhancement factor $\zeta = 0.85$ due to compression (Eq. 3.11),
- "Filter"-criteria, i.e. $S_{1.4} > 8\sigma_{\text{rms}} \cdot$ beam, DoG (Fig.3.7), and shape-based detection probability (Eq. 3.19).

We will constrain the unknown parameter ξ_e only due to the number count Δ_{count} of filtered galaxy clusters. We base our rejection threshold ϵ on quantile: model samples are accepted that rank in the 0.75 best quantile (for every metric) compared to all models accepted in the last iteration. For each iteration we choose a population size of 135 samples to be accepted. Once the chosen number of model realizations fall within ϵ, the iteration step is completed. Once the estimated PDF becomes stationary, i.e. doesn't change any longer, we can assume ABC-pmc to be completed. At this stage the acceptance ratio is continuously decreasing as smaller ϵ do not help in shrinking

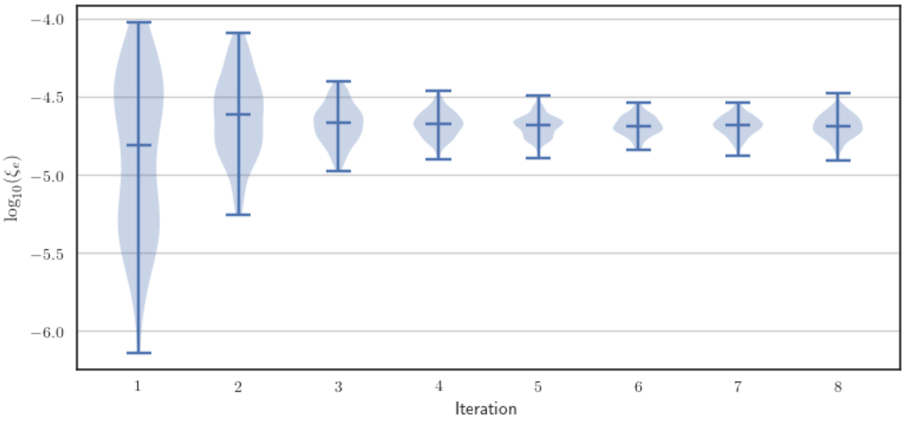

FIGURE 4.7: Violin plot of the development of the posterior-estimate of the efficiency ξ_e over all twelve iterations. This experiment generated 4000 model samples, using 2500 CPU hours of computing time.

the PDF any more. At its extreme the shrinkage of the acceptance ratio goes with $quantile^{N_{\mathrm{metric}}}$, in this case $0.75^1 = 0.75$ per iteration.

The evolution of the estimated PDF is shown in Fig 4.7: Within 5 iterations the estimate of the posterior probability converges to $\xi_e = -4.69 \pm 0.08$. As we will see in the next section, once we relax the assumptions on the magnetic field parameters, this estimate becomes less confined.

4.3 Exploring the standard emission model

Here we present the first results of ABC-pmc modeling to explore the whole parameter space of the standard emission model that we used throughout this work. The full parameter set that we can explore consists of three emission model plus one detection bias parameter. In this experiment the used summary statistics are Δ_{count}, $\Delta_{\mathrm{average\,relic}}$, $\Delta_{\mathrm{2DKS-test}}$, and $\Delta_{\overline{\alpha}_{\mathrm{int}}}$. Though there are several methods to constrain B_0, ξ_e, and κ which we label as the model $M_{\mathrm{DSA,therm}}$ we show that even with the limited number of NVSS relic clusters we are able to set a constraint on these parameters.

At each ABC-pmc iteration step we required 250 simulation trials to be within the 0.85 quantile of all metrics compared to all models selected at the last iteration. At the first step of iteration we start with an uniform prior in the parameter space $\boldsymbol{\theta}$ of $M_{\mathrm{DSA,therm}}$ and set the initial constrains to $\Delta_{\mathrm{count}} < 3$, $\Delta_{\mathrm{average\,relic}} < 0.7$, $\Delta_{\mathrm{2DKS-test}} < 0.98$, and $\Delta_{\overline{\alpha}_{\mathrm{int}}} < 0.2$. We consider a of number 250 trials as sufficient to allow an estimate of the posterior distribution $P(\theta|\mathcal{D})$ for the given number of free model parameters. In any typical ABC-pmc experiment several thousands to tens of thousand model realizations are produced. In practice the final quality of the model inference will become limited if the forward model is computational prohibitive (Schmit and J. R. Pritchard, 2018; Kern et al., 2017). Because of this, the rate at which the forward model produces predictions is one of our prime interests. In Appendix D we describe what measures we took to reduce the run-time of ABC-pmc to roughly two weeks per *experiment* for the used hardware of 16 CPUs.

The acceptance ratio between the last two iterations shrank by the maximum possible margin of $0.51 \sim quantile^{N_{\mathrm{metric}}} = 0.85^4 = 0.52$ indicating convergence. For this particular experiment, ABC-pmc converged to a stable estimate of the posterior (Fig 4.8) within 6 iterations. We let the procedure run further after the 6th iteration iteration, to gather more model trials that fulfilled the selection criteria $\Delta_{\mathrm{count}} < 0.799$, $\Delta_{\mathrm{average\,relic}} < 0.2667$, $\Delta_{\mathrm{2DKS-test}} < 0.7196$, and $\Delta_{\overline{\alpha}_{\mathrm{int}}} < 0.0435$.

The estimated PDF reveals several degeneracies in the parameter estimate: Firstly, as pointed out by Nuza et al. (2017) B_0 and ξ_e are strongly negatively correlated when only accounting for the number of (elongated) relics. The slope of this correlations flattens below $B_0 \sim 5\,\mu$G, causing the PDF to *bend* at this threshold. The reason for the flattening of the PDF is the lower dependency of the total emitted synchrotron emission on the magnetic fields for magnetic field strengths above B_{cmb} as described in Sec. 3.2.2. This degeneracy can only partially be broken when invoking the two-dimensional two-sided Kolmogorov-Smirnov test (Δ_{2DKS}) on the LLS-$P_{1.4}$ distribution of radio relics. To break this degeneracy one needs to incorporate metrics that are informative for ξ_e or B_0. A measurement of further relic properties like polarization or Faraday Rotation measured in future surveys will likely be suited to further confine the parameters of the magnetic field, and with that also the acceleration efficiency ξ_e. Secondly, while the marginalized estimate of κ (the exponent of the magnetic field to density scaling) is $0.56^{+0.49}_{-0.63}$, it is negatively correlated with the strength B_0 of the magnetic field. A similar positive, yet positive correlation is seen with $b_{\mathrm{pca,filter}}$ (the survey completeness for compact relics) and κ.

While absolute values of $B_0 \gtrsim 10\,\mu$G and a homogeneous magnetic field $\kappa \sim 0$ are not excluded by the estimated $\log_{10}(B_0/\,\mu\mathrm{G}) = 1.2^{+0.40}_{-0.49}$ and $\kappa = 0.56^{+0.49}_{-0.63}$ they are not supported by direct studies of the magnetic field (Govoni et al., 2017) or estimates of the magnetic field strength downstream the shock due to the width of radio relics ($5 - 10\,\mu$G as by Rajpurohit et al., 2018). Note that higher values than measured can be expected if other amplification effects of magnetic fields take place downstream the shock. By selecting trials with $B_0 < 5\,\mu$G we can investigate the assumption that the magnetic fields are in line with the known literature values. This assumption leads to a more confined $\xi_{\mathrm{e}} = -4.71^{+0.14}_{-0.13}$, $\kappa = 0.94^{-0.38}_{-0.35}$, suggesting a somewhat

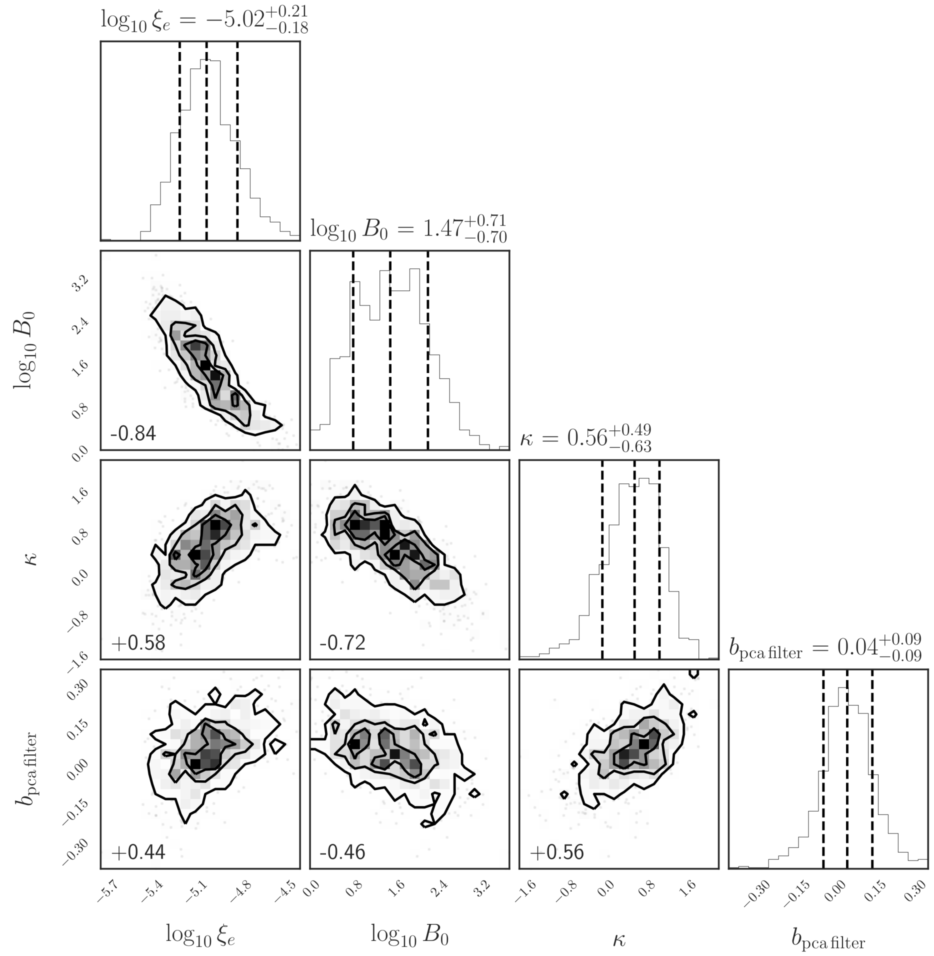

FIGURE 4.8: `Corner`-plot (Foreman-Mackey, 2016) including the 950 model trials that fulfilled the ϵ requirements of the last (fifth) iteration - which we deem to have converged: The labels on top of each histogram indicate the mean and one sigma variance. The labels on top of each 1D-histogram show the 0.5 quantile of the marginalized distribution with the upper and lower errors referring to the $+\sigma$ and $-\sigma$ quantile. The density-plots show contours engulfing the sample within the 30, 60, 90 percent of highest density, respectively. The values in the lower-left of each density-plot indicate the Pearson-correlation.

higher magnetic-field to density scaling than proposed by other the observations. Interestingly, the additional constraint on B_0 effectively suppresses all degeneracies but of the one between κ and $b_{\mathrm{pca,filter}}$. This suggests that knowing either B_0 or ξ_e would reduce the uncertainties of this analysis drastically.

One of the major advantages of (approximate) Bayesian computation is that one can quantify the suitability of the model to reproduce the observed data (Fig. 4.9). A possible shortcomings of the model becomes visible by the remaining discrepancy in $\Delta_{\mathrm{average\,relic}}$ - which is 0.30 ± 0.05 which is six standard deviations away from a perfect match with NVSS. This discrepancy is also depicted in Fig. 4.10. Likewise, $\Delta_{\mathrm{average\,relic}}$ is of by two standard deviations, indicating that the best solutions do not always yield a sufficient match. Either the observed relic population or the NVSS sample of radio relics contrives a very improbable configuration or, much more likely, the used model is not fully adequate to reproduce the observed relic population.

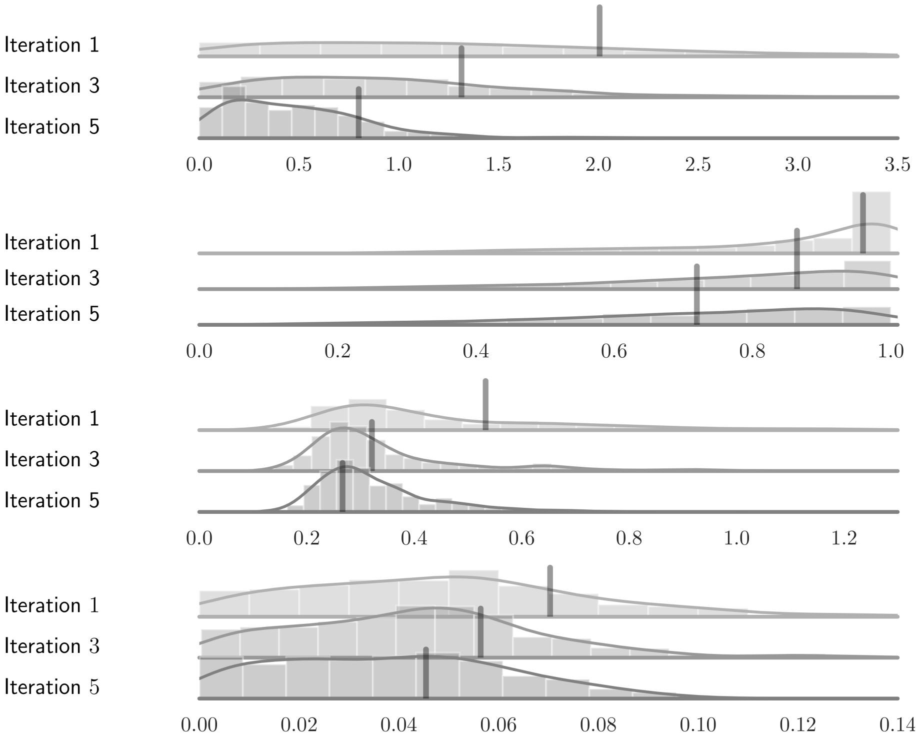

FIGURE 4.9: Shown is the KDE distribution of the metric distances Δ_{count} *(top)*, $\Delta_{\mathrm{average\,relic}}$ *(middle)*, Δ_{2DKS} *(middle low)*, and $\Delta_{\overline{\alpha}_{\mathrm{int}}}$ *(bottom)* for 72 samples at the given iteration steps after the initial prior parameter proposal. The selection criteria ϵ become more restrictive by each iteration and are indicated by a vertical line.

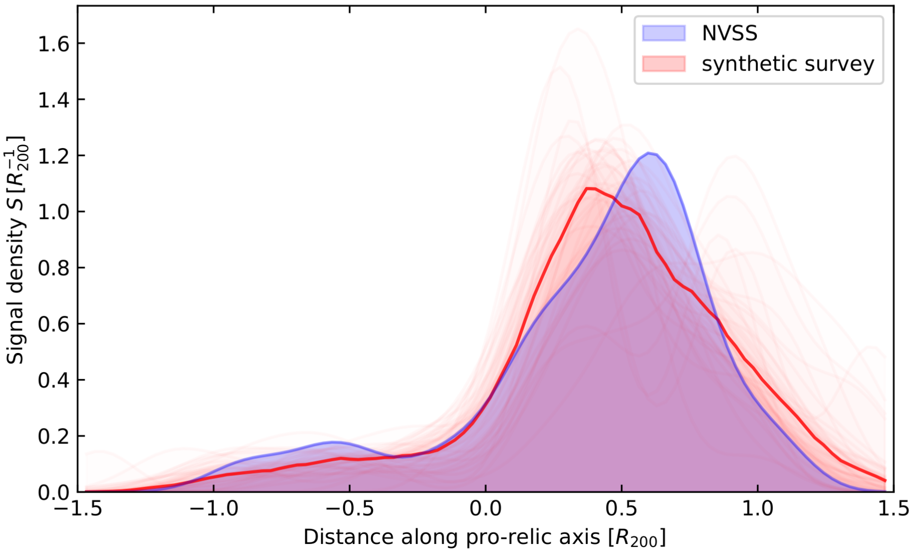

FIGURE 4.10: Shown is the distance distribution for 36 models samples drawn from the finally estimated parameters indicating a remaining discrepancy.

4.4 Exploring a model with pre-existing CR electrons

We made it to one of our the goals of this work to test if thermal pool DSA can explain the observed radio relic population. While we found in Nuza et al. (2017) a prescription that explains the relic population in many respects, it falls short to explain the relics' projected distance from the cluster-center. As already mentioned in Sec. 1.2.2 several authors suggest that at least part of the radio relics observed could arise due to electrons re-accelerated predominantly from the pre-existing CR-content in galaxy clusters. We test if this assumption can lead to a better match of observed and synthetic radio relic statistics by investigating a toy-model of ICM population of pre-existing CRes.

4.4.1 Description of the model extension

We label this model $M_{\mathrm{DSA,pre}}$. Our approach parameterizes the pre-existing CR electron population of the ICM by the last time t_{shocked} since acceleration through DSA happened: A high Mach number shock accelerates a fraction $\Xi_{\mathrm{ratio}} > 1$ of thermal electrons in the ICM, at a set time t before the current shock event. The aging of the electrons is assumed to be dominated by synchrotron losses and the IC-process (Eq. 1.13 - Eq. 1.14). By assuming that the accelerated CR population was accelerated by a strong shock to a momentum distribution with an exponent of $p_{\mathrm{inj}} = -2$ this results in an additional emission arising from the pre-existing CR electron population relative to the already produced emission:

$$\gamma_{\text{boost}} = 2.4 \cdot 10^4 \left(\frac{t_{\text{shocked}}}{1\ \text{Gyr}} \right)^{-1} \left(\frac{B^2_{\text{upstream}} + B^2_{\text{cmb}}}{1\ \mu\text{G}} \right)^{-1/2} \tag{4.8}$$

with the magnetic field used being the upstream magnetic field, before amplification through compression. This results in a boosting-factor of synchrotron emission that, due to the momentum-power-index of the accelerated electron population, dependents on the Mach-number (Eq. 1.22):

$$f_{\text{boost}} = \Xi_{\text{ratio}} \cdot \gamma_{\text{boost}}^{p_{\text{inj}} - p_{\text{thermal, inj}}} \tag{4.9}$$

with the total emission being

$$f_{\text{tot}} = f_{\text{thermal}} \cdot (1 + f_{\text{boost}})\,. \tag{4.10}$$

The resulting enhancement of radio emission compared over the radio emission of our previous model can bee seen in Fig 4.11. By using the above formula, we neglect any

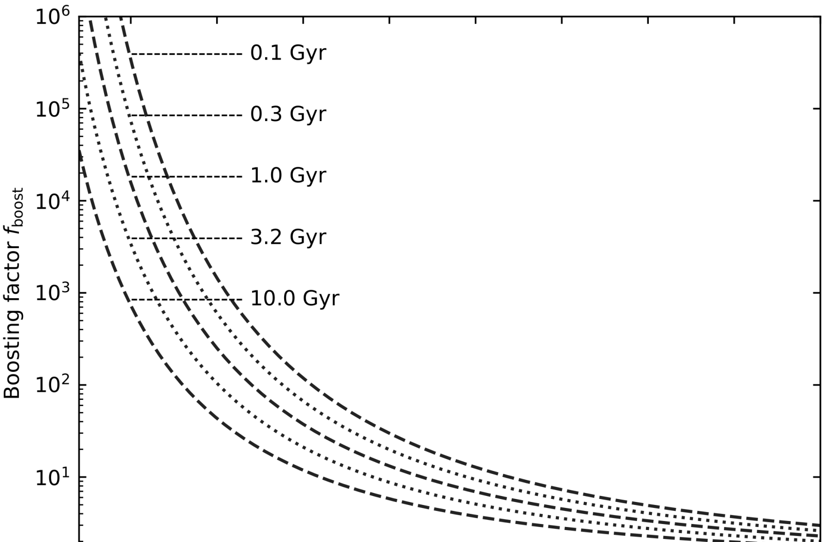

FIGURE 4.11: Shown is the boosting factor f_{boost} due to Eq. 4.9 for a 4 μG upstream equivalent magnetic field strength and a pre-accelerated fraction $\Xi_{\text{ratio}} = 1$.

change in magnetic field strength or redshift, within the time frame of the last strong shock. The aging of the CR electron population should hence be underestimated, in regions where the background CMB equivalent magnetic field strength changed significantly since the last acceleration event.

The brightness of relics that originate from pre-existing electrons is less dependent on the Mach number of the shock, i.e. inner shocks would be brightened relative to the outer shocks. The fact that observed relics are farther away than simulated ones, however implies a radial dependence of the pre-existing CR electron fraction - which we aim at modeling. We parameterize the time since the last shock through an attenuated power law relation to the ICM density:

$$t_{\mathrm{shocked}} = t_0 \left(\frac{n_{\mathrm{e}}}{10^{-6}\mathrm{cm}^{-3}} \right)^{s_{\mathrm{n}}} . \tag{4.11}$$

The slope s_{n} derives itself from the aging time t_1 at low density, the aging time t_2 at high densities and the corresponding density contrast:

$$s_{\mathrm{n}} = \frac{\log(n_0) - \log(n_1)}{\log(t_0) - \log(t_1)} . \tag{4.12}$$

Our model of pre-existing CRes hence can cover the case of cluster-wide events with $t_1 = t_2$ as well as processes leading to a gradient of pre-existing CR electron age across the cluster with $t_1 \neq t_2$. It is possible to model the cause of the acceleration of pre-existing electrons as a quasi-static process or as a stochastic independent process. The later seems to be more likely if the pre-existing CR electron populations steems from events like major mergers or AGN activity. Because we assume a stochastic independent process, i.e. a Poisson-process, t_{shocked} turns to an average waiting time and is hence multiplied with a factor f_{poisson} sampled from a Poisson distribution with unit waiting time:

$$P(T > t) = \exp\left(-t/t_{\mathrm{shocked}}\right), \tag{4.13}$$

$$t_{\mathrm{shocked}} \rightarrow t_{\mathrm{shocked}} \cdot f_{\mathrm{poisson}} \tag{4.14}$$

for every sampled galaxy cluster.

4.4.2 Contribution of cosmic ray electrons to the relic emission

The ABC-pmc iterations are carried out exactly like in the previous sections. An analysis of the correlations within the set of parameters $\vec{\theta}$ shows us that all other parameters that were already incorporated in the previous model of DSA on thermal pool are not significantly influenced. While the model parameters conform to a wide range of possible pre-existing CR-electron content they mostly move within the initially selected prior range (Fig. 4.12) which implies that the hole expressiveness of the model does not help in improving any metrics.

The absolute correlation of the parameters describing the pre-existing CR electron population (Ξ_{ratio},t_1,t_2) with the parameters of the thermal-pool based DSA are all smaller 0.1, except from the correlation between $log_{10}(t_1)$ and κ being 0.15. This suggests that the inclusion of pre-existing electrons in the model is bound to a small impact on the NVSS -like relic properties.

The correlation within Θ_{ratio},t_1, and t_2 are somewhat stronger. Both t_1 and t_2 are positively correlated with Θ_{ratio}, meaning that the overall impact of a stronger fraction of pre-existing CRes in the DSA process is balanced by longer aging t, corresponding to a smaller event rate. Fig 4.14 suggests that pre-existing CRes do not have a considerable contribution to the radio relic emission at NVSS frequencies and sensitivities ($S_{1.4,\mathrm{pre}}/S_{1.4,\mathrm{tot}} < 0.01$).

The inferred small impact of pre-existing CRes to the pool of radio relics might be stunning at first, but at least partially be attributed to decisions made for the sample selection: As we assume a model of random re-acceleration events allowing for those events widens the spread of the radio relic properties - which is not observed. Any model with parameters that result in a significant contribution of pre-existing CRes to the radio emission will also suffer from a large variance in the observed integrated spectral index. Models that allow a significant contribution of pre-existing electrons lead to radio-phoenix like objects (size of few hundred kpc, larger areal luminosity, $\alpha_{\mathrm{int}} < -1.5$). Note that our conclusion is restricted to the relatively bright sample of NVSS relics, after exclusion of sources that might be considered as phoenixes and by including relics in the NVSS sample with $\alpha_{\mathrm{int}} > -1$. We hence might be biased by our sample selection. Future studies should consider this.

The quantities in Fig 2.7 excellently follow the correlation of NVSS, including the strong positive correlation between $P_{1.4}$ and LLS; the weaker positive correlation between α_{int} and $D_{\mathrm{proj,pix}}$; and the missing correlation between α_{int} and $P_{1.4}$.

Adding pre-existing CRes to the model does not yield better results for any of the investigated metrics (Tab. 4.1). The number of free parameters however increases by three. Any difference might be spurious and the result of noise in the posterior-estimation by ABC-pmc . Trials that fulfill the ABC-pmc selection criteria attribute less than one percent of their relic emission a population of pre-existing CRes. We do conclude that the bulk of the known radio relic properties can be explained by thermal pool DSA paired with an non-negligible detection bias towards larger and

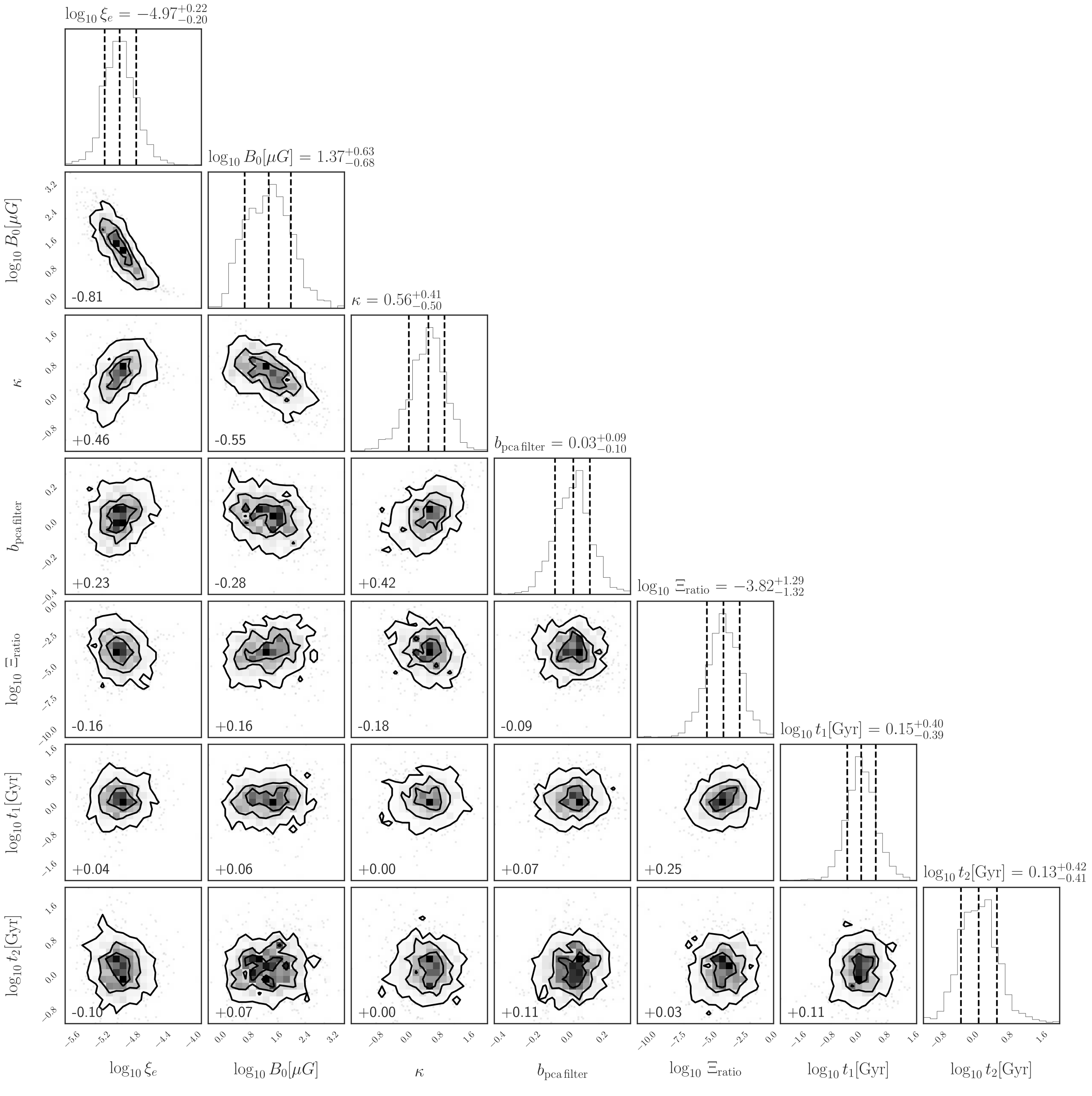

FIGURE 4.12: `Corner`-plot (Foreman-Mackey, 2016) of inferred model parameters parameters for a model including pre-existing CRes including the $\sim$ 900 model trials that fulfilled the ϵ requirements of the last (fifth) iteration - which we deem to have converged: The labels on top of each 1D-histogram show the 0.5 quantile of the marginalized distribution with the upper and lower errors referring to the $+1\sigma$ and $-\sigma$ quantile. The density-plots show contours engulfing the sample within the 30, 60, 90 percent of highest density, respectively. The values in the lower-left of each density-plot indicate the Pearson-correlation.

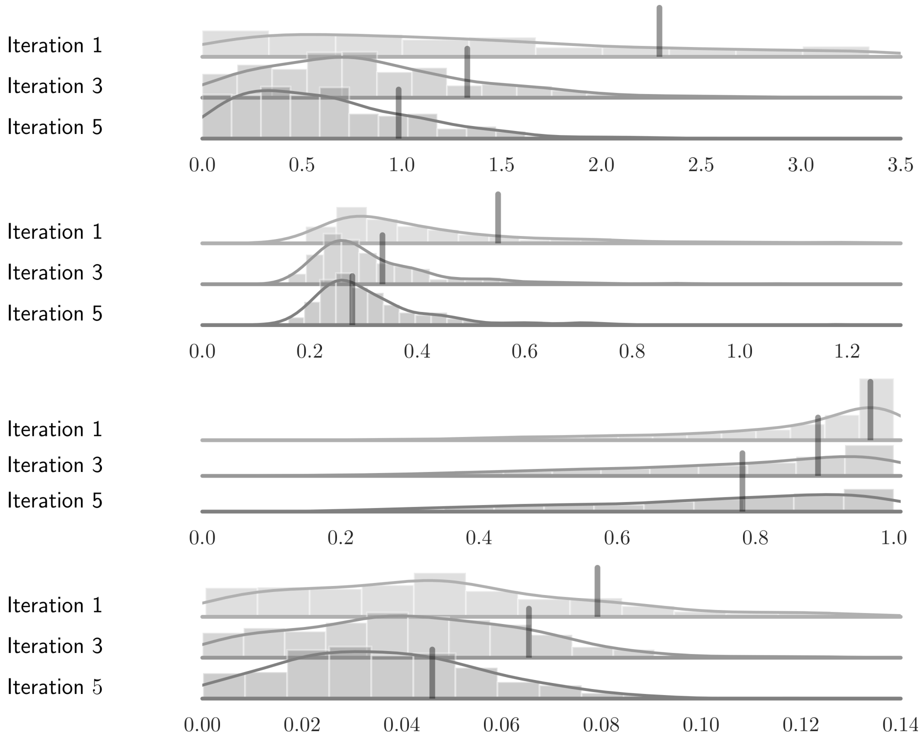

FIGURE 4.13: Shown is the KDE distribution of the metric distances Δ_{count} *(top)*, $\Delta_{\mathrm{average\,relic}}$ *(middle)*, Δ_{2DKS} *(middle low)*, and $\Delta_{\overline{\alpha}_{\mathrm{int}}}$ *(bottom)* for 500 samples at the given iteration step. The selection criteria ϵ become more restrictive by each iteration and are indicated by a vertical line.

more extended relics ($b_{\mathrm{pcafilter}} = 0.0 \pm 0.1$). A significant contribution of pre-existing CRes to the synchrotron emission observed for NVSS relics is disfavored.

TABLE 4.1: Metric distances of both investigated models at the last iteration, with $+1\sigma$ and -1σ range

Metric	$M_{\mathrm{DSA,therm}}$	$M_{\mathrm{DSA,pre}}$
Δ_{count}	$0.43^{+0.38}_{-0.29}$	$0.57^{+0.51}_{-0.37}$
$\Delta_{\mathrm{2DKS-test}}$	$0.77^{+0.16}_{-0.27}$	$0.80^{+0.16}_{-0.28}$
$\Delta_{\mathrm{average\,relic}}$	$0.30^{+0.14}_{-0.06}$	$0.29^{+0.14}_{-0.06}$
$\Delta_{\overline{\alpha}_{\mathrm{int}}}$	$0.038^{+0.024}_{-0.026}$	$0.038^{+0.025}_{-0.021}$

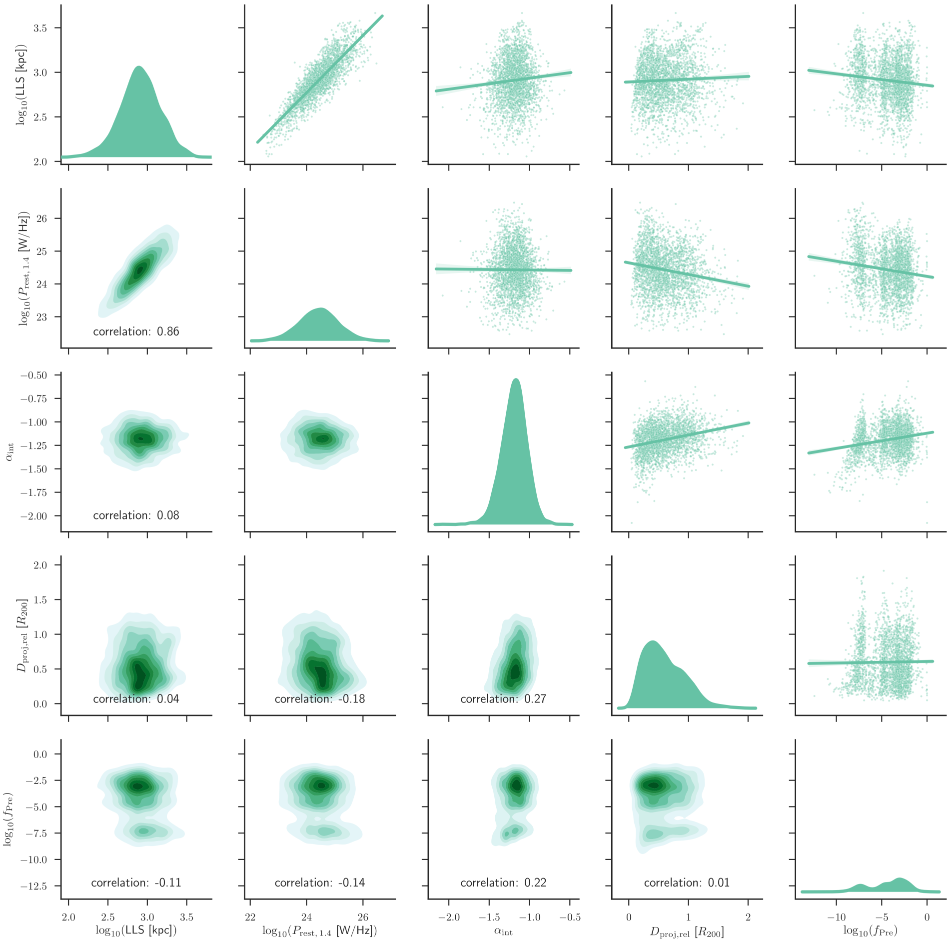

FIGURE 4.14: Scatterplot matrix of 30 model trials with pre-existing CRes drawn from the estimated PDF of the last (fifth) iteration. The fractional contribution of the pre-existing CRes to the synchrotron emission at 1.4 GHz is denoted with f_{pre}.

4.5 Potential of future studies

New sky surveys

Because any object already classified as radio relic within the scientific community needed to fulfill a number of selection criteria, the sample of known radio relics yields a number of informative measures. However, only for few radio relics images of high physical resolution that include spectral and polarization information exist (van Weeren et al., 2010; Owen et al., 2014; Shimwell et al., 2015; Rajpurohit et al., 2018). Including surveys, that contain those capabilities and increase the radio relic sample, especially towards objects with steeper spectral indices would be an efficient measure to provide this method the information it needs to discern models with pre-existing CRes from models without.

Wider class selection

Some detections in our simulation with a significant amount of pre-existing CRes might be considered as phoenixes. Our used sample of diffuse radio emission contains only radio relics and excludes radio phoenixes as well as radio haloes. A sample that includes these two additional classes would be more sensitive to the transitive CR-electron population and better suited to constrain the physics of the electron acceleration in the ICM, given that the physical phenomena responsible for the latter two classes of objects would also be covered by the model.

More pathways of cosmic ray acceleration at shocks

The remaining difference of simulations and observed relics suggests that the parameter inference might be hampered by an over-simplified model of radio relic generation. This leaves room for improvement and investigation of models of radio relic generation including SDA , postshock turbulence, other forms of pre-existing CR-electron injectionsor non-stationary shocks.

Larger cosmological simulations

Simulated relics in our study reside in less massive clusters than in NVSS (Sec. 3.3.2). This will bias our parameter estimates to higher ξ_e. The recommended course of action for future studies is to include the most massive clusters that form in simulations with $V_{\mathrm{com}} \gg 1\,\mathrm{Mpc}^3$. For example, employing the re-simulation technique to the most massive clusters in simulations like Millenium-XXL (Angulo et al., 2012) could help to mitigate the mass bias between NVSS and the employed simulations (Tab. 3.1). Larger simulations would also imply larger samples of simulated galaxy clusters, and an higher internal variance of the synthetic surveys. This would help to reduce the unknown bias of ABC-pmc due to the limited sampling of the cosmological simulations. We additionally recommend galaxy cluster simulations to account for the the scaling of the observed volume with redshift to adopt a light-cone like simulation approach (Llinares, 2017).

Different magnetic field models

The magnetic field model that we use is an simplification. For example we strictly work with an average magnetic field model, which as shown by Rajpurohit et al. (2018) could lead to systematical deviations in inferred radio relic properties, especially when comparing multi-frequency observations. Within their MHD simulation Skillman et al. (2013) find an empirical scaling relation of the magnetic field with the density having the form of a saturated power law:

$$\langle B \rangle = B_0 \left(1 - e^{-n/n_0}\right) \tag{4.15}$$

with $B_0 = 0.75\ \mu\mathrm{G}$ for the average magnetic field and $n_0 = 4.0 \cdot 10^{-4}\,\mathrm{cm}^{-3}$ for the saturation electron density and an average deviation of half an order of magnitude. For densities below the saturation density the relation $\langle B \rangle \propto n_{\mathrm{e}}$ holds. Even more, advancing one step further using a magneto-hydrodynamical simulation would allow to retrieve the shock obliquity directly from the shock normal and the magnetic field (Wittor et al., 2017). With a reliable model of the magnetic field in the ICM one could focus the inference on other model parameters like the acceleration mechanisms.

New likelihood-free inference techniques

The understanding to build informative summary statistics has been made considerable advancement have been made in the last years (Aeschbacher et al., 2012; Prangle, 2015). Recently, Charnock et al. (2018) proposed a data-driven approach that creates a non-linear combination out of a given set of statistics that is optimal in preserving the Fisher information. Similarly, in the field of population-genetics Mondal et al. (2019) employed the formalism described in Jiang et al. (2017) to find a minimal set of highly suited summary statistics. In addition, J. Alsing et al. (2018, Eq. 2.7) developed a more efficient particle sampling proposal and their findings for cosmological parameter inference in Justin Alsing et al. (2018) - labeling their method *Density Estimation Likelihood-Free Inference*, and later extended this approach to learn summary statistics that are robust to systematic uncertainties (Justin Alsing et al., 2019).

4.6 Summary

In this chapter we aimed at finding those parameters of the model described in Cha. 3 that have most support by the NVSS sky survey. With ABC population Monte Carlo (ABC-pmc) we adopt a method that allows us to constrain these parameters based on statistics of radio relics. Specifically we find the PDF of parametrizations of the ICM magnetic fields, DSA acceleration efficiency, and survey completeness - all of them with significant correlations to each other:

- The inferred magnetic field parameters are $\log_{10}(B_0/\,\mu\mathrm{G}) = 1.47^{+0.71}_{-0.70}$ and $\kappa = 0.56^{+0.49}_{-0.63}$. This study therefore within a large error-margin favors a higher magnetic field strength but a similar density scaling than previous investigations literature (Govoni et al., 2017, $B \sim (2 \pm 1)\,\mu\mathrm{G}$, $\kappa \sim 0.5 \ldots 1.0$).
- The estimate of the radio relic selection bias $b_{\mathrm{pca\,filter}} = 0.04^{+0.09}_{-0.09}$ is strongly correlated with the exponent κ of the density-based magnetic field scaling. Assuming a more complete sample leads to a lower estimate of κ. An estimated $40 - 60$ percent of all relics above 3.6 mJy flux density at 1.4 GHz are still undiscovered.
- The inferred electron acceleration efficiency $\log_{10}(\xi_\mathrm{e}) = -5.0 \pm 0.2$ is much smaller than inferred by (Botteon et al., 2019), revealing systematic differences in the approach and data base.
- Including the average spectral index as a selection criterion for models (i.e. as a metric) leads to a more confined κ and a lower correlation of other parameters with the selection bias.
- The statistics of radio relic properties show excellent agreement in two out of four aspects. While the number count and the LLS-power correlation can be well matched, a mismatch of the average projected distance of the relics from their host clusters remains as well as a mismatch of the average spectral index remains. This suggests, that better models of radio the origin of radio relics should exist.

Adding a simplified representation of pre-existing CRes to the model essentially favors the same statistics of radio relics properties, including the remaining discrepancy in the found distance of radio relics from their host-clusters centers. The inferred contribution of pre-existing CRes has a wide spread with most scenarios having virtually no contribution of pre-existing CRes to the emission ($f_{\mathrm{pre}} < 10^{-2}$). In fact, models with a significant contribution of pre-existing CRes on the radio power of NVSS radio relics are disfavored through the impact on the integrated spectral index they would have.

We thereby show the viability of ABC-pmc for parameter inference and model selection within the considered scope. Because of the scaling of the computational requirements of ABC-pmc with the depth of any survey it is foreseeable that future studies of this kind will facilitate the use of improved heuristics on the model sampling and selection procedure, most likely furthered by methods of machine learning. We also recommend future studies to consider larger simulated volumes, and upcoming surveys like LoTSS. Due to the potential of our method we confidently recommend to use it as a supplement to targeted studies of radio relics. Future sky surveys that map diffuse emission in galaxy clusters in a homogeneous way will contribute to unraveling the physics of the ICM.

Bibliography

Abell, G. O. (May 1958). "The Distribution of Rich Clusters of Galaxies." In: ApJS 3, p. 211. DOI: `10.1086/190036`.

Abell, G. O., H. G. Corwin Jr., and R. P. Olowin (May 1989). "A catalog of rich clusters of galaxies". In: ApJS 70, pp. 1–138. DOI: `10.1086/191333`.

Ackermann, M., M. Ajello, A. Albert, W. B. Atwood, L. Baldini, J. Ballet, G. Barbiellini, D. Bastieri, K. Bechtol, R. Bellazzini, E. Bissaldi, R. D. Blandford, E. D. Bloom, R. Bonino, E. Bottacini, J. Bregeon, P. Bruel, R. Buehler, G. A. Caliandro, R. A. Cameron, M. Caragiulo, P. A. Caraveo, J. M. Casandjian, E. Cavazzuti, C. Cecchi, et al. (Mar. 2016). "Search for Gamma-Ray Emission from the Coma Cluster with Six Years of Fermi-LAT Data". In: ApJ 819, 149, p. 149. DOI: `10.3847/0004-637X/819/2/149`. arXiv: `1507.08995 [astro-ph.HE]`.

Aeschbacher, S., M. A. Beaumont, and A Futschik (Nov. 2012). "A Novel Approach for Choosing Summary Statistics in Approximate Bayesian Computation". In: Genetics. eprint: `112.143164`.

Akeret, J., A. Refregier, A. Amara, S. Seehars, and C. Hasner (Aug. 2015). "Approximate Bayesian computation for forward modeling in cosmology". In: JCAP 8, 043, p. 043. DOI: `10.1088/1475-7516/2015/08/043`. arXiv: `1504.07245`.

Alsing, J., B. D. Wandelt, and S. M. Feeney (Aug. 2018). "Optimal proposals for Approximate Bayesian Computation". In: arXiv e-prints. arXiv: `1808.06040 [math.ST]`.

Alsing, Justin, Tom Charnock, Stephen Feeney, and Benjamin Wand elt (July 2019). "Fast likelihood-free cosmology with neural density estimators and active learning". In: MNRAS, p. 1888. DOI: `10.1093/mnras/stz1960`. arXiv: `1903.00007 [astro-ph.CO]`.

Alsing, Justin, Benjamin Wandelt, and Stephen Feeney (July 2018). "Massive optimal data compression and density estimation for scalable, likelihood-free inference in cosmology". In: MNRAS 477.3, pp. 2874–2885. DOI: `10.1093/mnras/sty819`. arXiv: `1801.01497 [astro-ph.CO]`.

Anderson, L., A. Pontzen, A. Font-Ribera, F. Villaescusa-Navarro, K. K. Rogers, and S. Genel (Oct. 2018). "Cosmological Hydrodynamic Simulations with Suppressed

Variance in the Lyman-α Forest Power Spectrum”. In: arXiv e-prints. arXiv: `1811.00043`.

Angulo, R. E., V. Springel, S. D. M. White, A. Jenkins, C. M. Baugh, and C. S. Frenk (Nov. 2012). “Scaling relations for galaxy clusters in the Millennium-XXL simulation”. In: MNRAS 426, pp. 2046–2062. DOI: `10.1111/j.1365-2966.2012.21830.x`. arXiv: `1203.3216`.

Bahcall, N. A. and R. Cen (Apr. 1993). “The mass function of clusters of galaxies”. In: ApJL 407, pp. L49–L52. DOI: `10.1086/186803`.

Baring, M. G. (1997). “Diffusive Shock Acceleration : the Fermi Mechanism.” In: Very High Energy Phenomena in the Universe; Moriond Workshop. Ed. by Y. Giraud-Heraud and J. Tran Thanh van, p. 97. eprint: `astro-ph/9711177`.

Beaumont, M. A., J. M. Cornuet, J. M. Marin, and C. P. Robert (Dec. 2009). “ Adaptive approximate Bayesian computation”. In: Biometrika 96.4, pp. 983–990. DOI: `10.1093/biomet/asp052`. eprint: `0901.1925`.

Becker, R. H., R. L. White, and D. J. Helfand (Sept. 1995). “The FIRST Survey: Faint Images of the Radio Sky at Twenty Centimeters”. In: ApJ 450, p. 559. DOI: `10.1086/176166`.

Bertin, E. and S. Arnouts (June 1996). “SExtractor: Software for source extraction.” In: A&A S 117, pp. 393–404. DOI: `10.1051/aas:1996164`.

Blandford, R. and D. Eichler (Oct. 1987). “Particle acceleration at astrophysical shocks: A theory of cosmic ray origin”. In: PhysRep 154, pp. 1–75. DOI: `10.1016/0370-1573(87)90134-7`.

Bocquet, S., A. Saro, K. Dolag, and J. J. Mohr (Mar. 2016). “Halo mass function: baryon impact, fitting formulae, and implications for cluster cosmology”. In: MNRAS 456, pp. 2361–2373. DOI: `10.1093/mnras/stv2657`. arXiv: `1502.07357`.

Böhringer, Hans, Gayoung Chon, and C. A. Collins (Oct. 2014). “The extended ROSAT-ESO Flux Limited X-ray Galaxy Cluster Survey (REFLEX II). IV. X-ray luminosity function and first constraints on cosmological parameters”. In: A&A 570, A31, A31. DOI: `10.1051/0004-6361/201323155`. arXiv: `1403.2927`.

Böhringer, Hans, Gayoung Chon, and Masataka Fukugita (Dec. 2017). “The extended ROSAT-ESO Flux-Limited X-ray Galaxy Cluster Survey (REFLEX II). VII. The mass function of galaxy clusters”. In: A&A 608, A65, A65. DOI: `10.1051/0004-6361/201731205`. arXiv: `1708.02449 [astro-ph.CO]`.

Bonafede, A., Marcus Brüggen, R. van Weeren, F. Vazza, G. Giovannini, H. Ebeling, A. C. Edge, Matthias Hoeft, and U. Klein (Oct. 2012). “Discovery of radio haloes and double relics in distant MACS galaxy clusters: clues to the efficiency of particle acceleration". In: MNRAS 426, pp. 40–56. DOI: `10.1111/j.1365-2966.2012.21570.x`. arXiv: `1206.6102 [astro-ph.CO]`.

Bonafede, A., L. Feretti, M. Murgia, F. Govoni, G. Giovannini, D. Dallacasa, K. Dolag, and G. B. Taylor (Apr. 2010). "The Coma cluster magnetic field from Faraday rotation measures". In: A&A 513, A30+. DOI: `10.1051/0004-6361/200913696`. arXiv: `1002.0594 [astro-ph.CO]`.

Bonafede, A., H. T. Intema, Marcus Brüggen, M. Girardi, M. Nonino, N. Kantharia, R. J. van Weeren, and H. J. A. Röttgering (Apr. 2014). "Evidence for Particle Re-acceleration in the Radio Relic in the Galaxy Cluster PLCKG287.0+32.9". In: ApJ 785, 1, p. 1. DOI: `10.1088/0004-637X/785/1/1`. arXiv: `1402.1492`.

Botteon, A., G. Brunetti, D. Ryu, and S. Roh (July 2019). "Shock acceleration efficiency in radio relics". In: arXiv e-prints, arXiv:1907.00966, arXiv:1907.00966. arXiv: `1907.00966 [astro-ph.HE]`.

Brunetti, G. and T. W. Jones (Mar. 2014). "Cosmic Rays in Galaxy Clusters and Their Nonthermal Emission". In: International Journal of Modern Physics D 23, 1430007-98, pp. 1430007–98. DOI: `10.1142/S0218271814300079`. arXiv: `1401.7519`.

Brunetti, G. and A. Lazarian (Apr. 2011). "Particle reacceleration by compressible turbulence in galaxy clusters: effects of a reduced mean free path". In: MNRAS 412, pp. 817–824. DOI: `10.1111/j.1365-2966.2010.17937.x`. arXiv: `1011.1198`.

Caprioli, D. and A. Spitkovsky (Mar. 2014). "Simulations of Ion Acceleration at Non-relativistic Shocks. I. Acceleration Efficiency". In: ApJ 783, 91, p. 91. DOI: `10.1088/0004-637X/783/2/91`. arXiv: `1310.2943 [astro-ph.HE]`.

Carassou, Sébastien, Valérie de Lapparent, Emmanuel Bertin, and Damien Le Borgne (Sept. 2017). "Inferring the photometric and size evolution of galaxies from image simulations. I. Method". In: A&A 605, A9, A9. DOI: `10.1051/0004-6361/201730587`. arXiv: `1704.05559 [astro-ph.IM]`.

Casella, G. and R. L. Berger (2001). Statistical Inference. Duxbury: Thomson Learning.

Charnock, Tom, Guilhem Lavaux, and Benjamin D. Wandelt (Apr. 2018). "Automatic physical inference with information maximizing neural networks". In: Phys.R̃ev. 97.8, 083004, p. 083004. DOI: `10.1103/PhysRevD.97.083004`. arXiv: `1802.03537 [astro-ph.IM]`.

Cho, Jungyeon (Dec. 2014). "Origin of Magnetic Field in the Intracluster Medium: Primordial or Astrophysical?" In: ApJ 797.2, 133, p. 133. DOI: `10.1088/0004-637X/797/2/133`. arXiv: `1410.1893 [astro-ph.CO]`.

Clowe, D., M. Brada, A. H. Gonzalez, M. Markevitch, S. W. Randall, C. Jones, and D. Zaritsky (Sept. 2006). “A Direct Empirical Proof of the Existence of Dark Matter”. In: ApJL 648, pp. L109–L113. DOI: `10.1086/508162`. eprint: `astro-ph/0608407`.

Colafrancesco, S., P. Marchegiani, and C. M. Paulo (Nov. 2017). “The correlation between radio power and Mach number for radio relics in galaxy clusters”. In: MNRAS 471, pp. 4747–4759. DOI: `10.1093/mnras/stx1806`. arXiv: `1707.07677 [astro-ph.HE]`.

Condon, J. J., W. D. Cotton, E. W. Greisen, Q. F. Yin, R. A. Perley, G. B. Taylor, and J. J. Broderick (May 1998). “The NRAO VLA Sky Survey”. In: AJ 115, pp. 1693–1716. DOI: `10.1086/300337`.

Condon, J. J. and S. M. Ransom (2019). Essential Radio Astronomy. URL: `https://www.cv.nrao.edu/~sransom/web/Ch5.html` (visited on 07/07/2019).

Daddi, E., S. Jin, V. Strazzullo, M. T. Sargent, T. Wang, C. Ferrari, E. Schinnerer, V. Smoli, A. Calabró, R. Coogan, J. Delhaize, I. Delvecchio, D. Elbaz, R. Gobat, Q. Gu, D. Liu, M. Novak, and F. Valentino (Sept. 2017). “Radio Selection of the Most Distant Galaxy Clusters”. In: ApJL 846.2, L31, p. L31. DOI: `10.3847/2041-8213/aa8808`. arXiv: `1708.06910 [astro-ph.CO]`.

de Gasperin, F., H. T. Intema, and D. A. Frail (Mar. 2018). “A radio spectral index map and catalogue at 147-1400 MHz covering 80 per cent of the sky”. In: MNRAS 474.4, pp. 5008–5022. DOI: `10.1093/mnras/stx3125`. arXiv: `1711.11367 [astro-ph.IM]`.

de Gasperin, F., H. T. Intema, J. Ridl, M. Salvato, R. van Weeren, A. Bonafede, J. Greiner, R. Cassano, and Marcus Brüggen (Jan. 2017). “Tracing low-mass galaxy clusters using radio relics: the discovery of Abell 3527-bis”. In: A&A 597, A15, A15. DOI: `10.1051/0004-6361/201628945`. arXiv: `1609.08339`.

de Gasperin, F., R. J. van Weeren, Marcus Brüggen, F. Vazza, A. Bonafede, and H. T. Intema (Nov. 2014). “A new double radio relic in PSZ1 G096.89+24.17 and a radio relic mass-luminosity relation”. In: MNRAS 444, pp. 3130–3138. DOI: `10.1093/mnras/stu1658`. arXiv: `1408.2677`.

de Haan, T., B. A. Benson, L. E. Bleem, S. W. Allen, D. E. Applegate, M. L. N. Ashby, M. Bautz, M. Bayliss, S. Bocquet, M. Brodwin, J. E. Carlstrom, C. L. Chang, I. Chiu, H.-M. Cho, A. Clocchiatti, T. M. Crawford, A. T. Crites, S. Desai, J. P. Dietrich, M. A. Dobbs, A. N. Doucouliagos, R. J. Foley, W. R. Forman, G. P. Garmire, E. M. George, et al. (Nov. 2016). “Cosmological Constraints from Galaxy Clusters in the 2500 Square-degree SPT-SZ Survey”. In: ApJ 832, 95, p. 95. DOI: `10.3847/0004-637X/832/1/95`. arXiv: `1603.06522`.

Dietrich, J. (Apr. 2016). NFW: NFW v0.1 (Version v0.1). `https://github.com/joergdietrich/NFW`. DOI: `10.5281/zenodo.50664`. arXiv: `1706.04203`.

Dolag, K., E. Komatsu, and R. Sunyaev (Dec. 2016). "SZ effects in the Magneticum Pathfinder simulation: comparison with the Planck, SPT, and ACT results". In: MNRAS 463, pp. 1797–1811. DOI: `10.1093/mnras/stw2035`. arXiv: `1509.05134`.

Dolag, K., S. Schindler, F. Govoni, and L. Feretti (Nov. 2001). "Correlation of the magnetic field and the intra-cluster gas density in galaxy clusters". In: A&A 378, pp. 777–786. DOI: `10.1051/0004-6361:20011219`. eprint: `astro-ph/0108485`.

Donnert, J. M. F., A. Stroe, G. Brunetti, D. Hoang, and H. Roettgering (Oct. 2016). "Magnetic field evolution in giant radio relics using the example of CIZA J2242.8+5301". In: MNRAS 462, pp. 2014–2032. DOI: `10.1093/mnras/stw1792`. arXiv: `1603.06570 [astro-ph.HE]`.

Drabent, A., Matthias Hoeft, R. F. Pizzo, A. Bonafede, R. J. van Weeren, and U. Klein (Mar. 2015). "Diffuse radio emission in the complex merging galaxy cluster Abell 2069". In: A&A 575, A8, A8. DOI: `10.1051/0004-6361/201424828`. arXiv: `1412.6337 [astro-ph.GA]`.

Duffy, A. R., J. Schaye, S. T. Kay, and C. Dalla Vecchia (Oct. 2008). "Dark matter halo concentrations in the Wilkinson Microwave Anisotropy Probe year 5 cosmology". In: MNRAS 390, pp. L64–L68. DOI: `10.1111/j.1745-3933.2008.00537.x`. arXiv: `0804.2486`.

Eckert, D., V. Ghirardini, S. Ettori, E. Rasia, V. Biffi, E. Pointecouteau, M. Rossetti, S. Molendi, F. Vazza, F. Gastaldello, M. Gaspari, S. De Grandi, S. Ghizzardi, H. Bourdin, C. Tchernin, and M. Roncarelli (Jan. 2019). "Non-thermal pressure support in X-COP galaxy clusters". In: A&A 621, A40, A40. DOI: `10.1051/0004-6361/201833324`. arXiv: `1805.00034 [astro-ph.CO]`.

Eddington, A. S. (Mar. 1913). "On a formula for correcting statistics for the effects of a known error of observation". In: MNRAS 73, pp. 359–360. DOI: `10.1093/mnras/73.5.359`.

Ensslin, T. A., P. L. Biermann, U. Klein, and S. Kohle (Apr. 1998). "Cluster radio relics as a tracer of shock waves of the large-scale structure formation". In: A&A 332, pp. 395–409. eprint: `astro-ph/9712293`.

EnSSlin, T., C. Pfrommer, F. Miniati, and K. Subramanian (Mar. 2011). "Cosmic ray transport in galaxy clusters: implications for radio halos, gamma-ray signatures, and cool core heating". In: A&A 527, A99, A99. DOI: `10.1051/0004-6361/201015652`. arXiv: `1008.4717`.

Farnsworth, D., L. Rudnick, S. Brown, and G. Brunetti (Dec. 2013). "Discovery of Megaparsec-scale, Low Surface Brightness Nonthermal Emission in Merging

Galaxy Clusters Using the Green Bank Telescope”. In: ApJ 779, 189, p. 189. DOI: `10.1088/0004-637X/779/2/189`. arXiv: `1311.3313`.

Fasano, G. and A. Franceschini (Mar. 1987). “A multidimensional version of the Kolmogorov-Smirnov test”. In: MNRAS 225, pp. 155–170. DOI: `10.1093/mnras/225.1.155`.

Feretti, L., G. Giovannini, F. Govoni, and M. Murgia (May 2012). “Clusters of galaxies: observational properties of the diffuse radio emission”. In: A&AR̃ev. 20, 54. ACM, p. 54. DOI: `10.1007/s00159-012-0054-z`. arXiv: `1205.1919 [astro-ph.CO]`.

Filippi, S., C. P Barnes, J. Cornebise, and M. P. H. Stumpf (Mar. 2013). “On optimality of kernels for approximate Bayesian computation using sequential Monte Carlo”. In: Statistical Applications in Genetics and Molecular Biology 12, pp. 87–107. DOI: `10.1515/sagmb-2012-006`.

Finoguenov, A., C. L. Sarazin, K. Nakazawa, D. R. Wik, and T. E. Clarke (June 2010). “XMM-Newton Observation of the Northwest Radio Relic Region in A3667”. In: ApJ 715, pp. 1143–1151. DOI: `10.1088/0004-637X/715/2/1143`. arXiv: `1004.2331`.

Foreman-Mackey, Daniel (June 2016). “corner.py: Scatterplot matrices in Python”. In: The Journal of Open Source Software 1.2, p. 24. DOI: `10.21105/joss.00024`. URL: `https://doi.org/10.21105/joss.00024`.

Giacconi, R., S. Murray, H. Gursky, E. Kellogg, E. Schreier, and H. Tananbaum (Dec. 1972). “The Uhuru catalog of X-ray sources.” In: ApJ 178, pp. 281–308. DOI: `10.1086/151790`.

Golovich, Nathan, William A. Dawson, David M. Wittman, Reinout J. van Weeren, Felipe Andrade-Santos, M. James Jee, Bryant Benson, Francesco de Gasperin, Tiziana Venturi, Annalisa Bonafede, David Sobral, Georgiana A. Ogrean, Brian C. Lemaux, Marua Brada, Marcus Brüggen, and Annika H. G. Peter (June 2018). “Merging Cluster Collaboration: A Panchromatic Atlas of Radio Relic Mergers”. In: arXiv e-prints, arXiv:1806.10619, arXiv:1806.10619. arXiv: `1806.10619 [astro-ph.CO]`.

Govoni, F., M. Murgia, V. Vacca, F. Loi, M. Girardi, F. Gastaldello, G. Giovannini, L. Feretti, R. Paladino, E. Carretti, R. Concu, A. Melis, S. Poppi, G. Valente, G. Bernardi, A. Bonafede, W. Boschin, M. Brienza, T. E. Clarke, S. Colafrancesco, F. de Gasperin, D. Eckert, T. A. Ensslin, C. Ferrari, L. Gregorini, et al. (Mar. 2017). “Sardinia Radio Telescope observations of Abell 194 - the intra-cluster magnetic field power spectrum”. In: ArXiv e-prints. arXiv: `1703.08688`.

Guo, X., L. Sironi, and R. Narayan (Oct. 2014a). “Non-thermal Electron Acceleration in Low Mach Number Collisionless Shocks. I. Particle Energy Spectra and

Acceleration Mechanism”. In: ApJ 794, 153, p. 153. DOI: `10.1088/0004-637X/794/2/153`. arXiv: `1406.5190 [astro-ph.HE]`.

– (Dec. 2014b). “Non-thermal Electron Acceleration in Low Mach Number Collisionless Shocks. II. Firehose-mediated Fermi Acceleration and its Dependence on Pre-shock Conditions”. In: ApJ 797, 47, p. 47. DOI: `10.1088/0004-637X/797/1/47`. arXiv: `1409.7393 [astro-ph.HE]`.

Heald, G. H., R. F. Pizzo, E. Orrú, R. P. Breton, D. Carbone, C. Ferrari, M. J. Hardcastle, W. Jurusik, G. Macario, D. Mulcahy, D. Rafferty, A. Asgekar, M. Brentjens, R. A. Fallows, W. Frieswijk, M. C. Toribio, B. Adebahr, M. Arts, M. R. Bell, A. Bonafede, J. Bray, J. Broderick, T. Cantwell, P. Carroll, Y. Cendes, et al. (Oct. 2015). “The LOFAR Multifrequency Snapshot Sky Survey (MSSS). I. Survey description and first results”. In: A&A 582, A123, A123. DOI: `10.1051/0004-6361/201425210`. arXiv: `1509.01257 [astro-ph.IM]`.

Heavens, A. F., R. Jimenez, and O. Lahav (Oct. 2000). “Massive lossless data compression and multiple parameter estimation from galaxy spectra”. In: MNRAS 317, pp. 965–972. DOI: `10.1046/j.1365-8711.2000.03692.x`. eprint: `astro-ph/9911102`.

Hitomi Collaboration, F. Aharonian, H. Akamatsu, F. Akimoto, S. W. Allen, L. Angelini, M. Audard, H. Awaki, M. Axelsson, A. Bamba, M. W. Bautz, R. Blandford, L. W. Brenneman, G. V. Brown, E. Bulbul, E. M. Cackett, R. E. A. Canning, M. Chernyakova, M. P. Chiao, P. S. Coppi, E. Costantini, J. de Plaa, C. P. de Vries, J.-W. den Herder, C. Done, et al. (Nov. 2017). “Atmospheric gas dynamics in the Perseus cluster observed with Hitomi”. In: ArXiv e-prints. arXiv: `1711.00240 [astro-ph.HE]`.

Hoeft, Matthias and Marcus Brüggen (Feb. 2007). “Radio signature of cosmological structure formation shocks”. In: MNRAS 375, pp. 77–91. DOI: `10.1111/j.1365-2966.2006.11111.x`. eprint: `arXiv:astro-ph/0609831`.

Hoeft, Matthias, Marcus Brüggen, G. Yepes, S. Gottlöber, and A. Schwope (Dec. 2008). “Diffuse radio emission from clusters in the MareNostrum Universe simulation”. In: MNRAS 391, pp. 1511–1526. DOI: `10.1111/j.1365-2966.2008.13955.x`. arXiv: `0807.1266`.

Hogg, D. W., I. K. Baldry, M. R. Blanton, and D. J. Eisenstein (Oct. 2002). “The K correction”. In: arXiv Astrophysics e-prints. eprint: `astro-ph/0210394`.

Hong, S. E., H. Kang, and D. Ryu (Oct. 2015). “Radio and X-Ray Shocks in Clusters of Galaxies”. In: ApJ 812, 49, p. 49. DOI: `10.1088/0004-637X/812/1/49`. arXiv: `1504.03102 [astro-ph.HE]`.

Hoyle, F. (Aug. 1969). “Magnetic Fields and Highly Condensed Objects”. In: Nature 223.5209, p. 936. DOI: `10.1038/223936a0`.

Hurier, G., R. Adam, and U. Keshet (Feb. 2019). “First detection of a virial shock with SZ data: implication for the mass accretion rate of Abell 2319”. In: A&A 622, A136, A136. DOI: `10.1051/0004-6361/201732468`.

Hurley-Walker, N., J. R. Callingham, P. J. Hancock, T. M. O. Franzen, L. Hindson, A. D. Kapiska, J. Morgan, A. R. Offringa, R. B. Wayth, C. Wu, Q. Zheng, T. Murphy, M. E. Bell, K. S. Dwarakanath, B. For, B. M. Gaensler, M. Johnston-Hollitt, E. Lenc, P. Procopio, L. Staveley-Smith, R. Ekers, J. D. Bowman, F. Briggs, R. J. Cappallo, A. A. Deshpande, et al. (Jan. 2017). “GaLactic and Extragalactic All-sky Murchison Widefield Array (GLEAM) survey - I. A low-frequency extragalactic catalogue”. In: MNRAS 464, pp. 1146–1167. DOI: `10.1093/mnras/stw2337`. arXiv: `1610.08318`.

Iapichino, Luigi and Marcus Brüggen (July 2012). “Magnetic field amplification by shocks in galaxy clusters: application to radio relics”. In: MNRAS 423, pp. 2781–2788. DOI: `10.1111/j.1365-2966.2012.21084.x`. arXiv: `1204.2455 [astro-ph.CO]`.

Intema, H. T. (2014). “SPAM: A data reduction recipe for high-resolution, low-frequency radio-interferometric observations”. In: vol. 13. Astronomical Society of India Conference Series. arXiv: `1402.4889 [astro-ph.IM]`.

Intema, H. T., P. Jagannathan, K. P. Mooley, and D. A. Frail (Feb. 2017). “The GMRT 150 MHz all-sky radio survey. First alternative data release TGSS ADR1”. In: A&A 598, A78, A78. DOI: `10.1051/0004-6361/201628536`. arXiv: `1603.04368`.

Intema, H. T., S. van der Tol, W. D. Cotton, A. S. Cohen, I. M. van Bemmel, and H. J. A. Röttgering (July 2009). “Ionospheric calibration of low frequency radio interferometric observations using the peeling scheme. I. Method description and first results”. In: A&A 501, pp. 1185–1205. DOI: `10.1051/0004-6361/200811094`. arXiv: `0904.3975 [astro-ph.IM]`.

Itahana, M., M. Takizawa, H. Akamatsu, T. Ohashi, Y. Ishisaki, H. Kawahara, and R. J. van Weeren (Dec. 2015). “Suzaku observations of the galaxy cluster 1RXS J0603.3+4214: Implications of particle acceleration processes in the “Toothbrush” radio relic”. In: PASJ 67, 113, p. 113. DOI: `10.1093/pasj/psv084`. arXiv: `1508.05845 [astro-ph.HE]`.

Jiang, B., T. Wu, C. Zheng, and W. Wong (Mar. 2017). “Learning summary statistic for approximate Bayesian computation via deep neural network.” In: Statistica Sinica 27, pp. 1595–1618. arXiv: `1510.02175`.

Kale, R. and K. S. Dwarakanath (Jan. 2012). “Multi-frequency Studies of Radio Relics in the Galaxy Clusters A4038, A1664, and A786”. In: ApJ 744, 46, p. 46. DOI: `10.1088/0004-637X/744/1/46`. arXiv: `1109.3261`.

Kale, R., D. R. Wik, S. Giacintucci, T. Venturi, G. Brunetti, R. Cassano, D. Dallacasa, and F. de Gasperin (Aug. 2017). "Discovery of a radio relic in the low mass, merging galaxy cluster PLCK G200.9-28.2". In: ArXiv e-prints. arXiv: `1708.01718`.

Kang, H. (June 2017). "Shock Acceleration Model with Postshock Turbulence for Giant Radio Relics". In: ArXiv e-prints. arXiv: `1706.03201 [astro-ph.HE]`.

Kang, H. and D. Ryu (Sept. 2010). "Diffusive Shock Acceleration in Test-particle Regime". In: ApJ 721.1, pp. 886–892. DOI: `10.1088/0004-637X/721/1/886`. arXiv: `1008.0429 [astro-ph.HE]`.

Kang, H., D. Ryu, R. Cen, and J. P. Ostriker (Nov. 2007). "Cosmological Shock Waves in the Large-Scale Structure of the Universe: Nongravitational Effects". In: ApJ 669, pp. 729–740. DOI: `10.1086/521717`. arXiv: `0704.1521`.

Kang, H., D. Ryu, and T. W. Jones (Sept. 2012). "Diffusive Shock Acceleration Simulations of Radio Relics". In: ApJ 756, 97, p. 97. DOI: `10.1088/0004-637X/756/1/97`. arXiv: `1205.1895 [astro-ph.HE]`.

Kempner, J. C., E. L. Blanton, T. E. Clarke, T. A. EnSSlin, M. Johnston-Hollitt, and L. Rudnick (2004). "Conference Note: A Taxonomy of Extended Radio Sources in Clusters of Galaxies". In: The Riddle of Cooling Flows in Galaxies and Clusters of galaxies. Ed. by T. Reiprich, J. Kempner, & N. Soker, pp. 335–+. eprint: `arXiv:astro-ph/0310263`.

Kern, N. S., A. Liu, A. R. Parsons, A. Mesinger, and B. Greig (Oct. 2017). "Emulating Simulations of Cosmic Dawn for 21 cm Power Spectrum Constraints on Cosmology, Reionization, and X-Ray Heating". In: ApJ 848, 23, p. 23. DOI: `10.3847/1538-4357/aa8bb4`. arXiv: `1705.04688`.

Kierdorf, M., R. Beck, Matthias Hoeft, U. Klein, R. J. van Weeren, W. R. Forman, and C. Jones (Apr. 2017). "Relics in galaxy clusters at high radio frequencies". In: A&A 600, A18, A18. DOI: `10.1051/0004-6361/201629570`. arXiv: `1612.01764`.

Klein, Ulrich and Andrew Fletcher (2014). Galactic and Intergalactic Magnetic Fields. Science.

Klypin, Anatoly A., A. V. Kravtsov, J. S. Bullock, and J. R. Primack (June 2001). "Resolving the Structure of Cold Dark Matter Halos". In: ApJ 554, pp. 903–915. DOI: `10.1086/321400`. eprint: `astro-ph/0006343`.

Klypin, Anatoly A., Sebastian Trujillo-Gomez, and Joel Primack (Oct. 2011). "Dark Matter Halos in the Standard Cosmological Model: Results from the Bolshoi Simulation". In: ApJ 740.2, 102, p. 102. DOI: `10.1088/0004-637X/740/2/102`. arXiv: `1002.3660 [astro-ph.CO]`.

Klypin, Anatoly A., G. Yepes, S. Gottlöber, F. Prada, and S. HeSS (Apr. 2016). “MultiDark simulations: the story of dark matter halo concentrations and density profiles”. In: MNRAS 457, pp. 4340–4359. DOI: `10.1093/mnras/stw248`. arXiv: `1411.4001`.

Kunz, M. W., A. A. Schekochihin, S. C. Cowley, J. J. Binney, and J. S. Sanders (Feb. 2011). “A thermally stable heating mechanism for the intracluster medium: turbulence, magnetic fields and plasma instabilities”. In: MNRAS 410.4, pp. 2446–2457. DOI: `10.1111/j.1365-2966.2010.17621.x`. arXiv: `1003.2719 [astro-ph.CO]`.

Lagage, P. O. and C. J. Cesarsky (Sept. 1983). “The maximum energy of cosmic rays accelerated by supernova shocks”. In: A&A 125, pp. 249–257.

Landau, L. D. and E. M. Lifshitz (1959). Fluid mechanics. Oxford: Pergamon Press.

Lee, S.-H., D. C. Ellison, and S. Nagataki (May 2012). “A Generalized Model of Nonlinear Diffusive Shock Acceleration Coupled to an Evolving Supernova Remnant”. In: ApJ 750, 156, p. 156. DOI: `10.1088/0004-637X/750/2/156`. arXiv: `1203.3614 [astro-ph.HE]`.

Llinares, C. (Sept. 2017). “The shrinking domain framework I: a new, faster, more efficient approach to cosmological simulations”. In: arXiv e-prints. arXiv: `1709.04703`.

Lodato, G. and C. J. Clarke (June 2011). “Resolution requirements for smoothed particle hydrodynamics simulations of self-gravitating accretion discs”. In: MNRAS 413, pp. 2735–2740. DOI: `10.1111/j.1365-2966.2011.18344.x`. arXiv: `1101.2448 [astro-ph.SR]`.

Loi, F., M. Murgia, F. Govoni, V. Vacca, L. Feretti, G. Giovannini, E. Carretti, F. Gastaldello, M. Girardi, F. Vazza, R. Concu, A. Melis, R. Paladino, S. Poppi, G. Valente, W. Boschin, T. E. Clarke, S. Colafrancesco, T. EnSSlin, C. Ferrari, F. de Gasperin, L. Gregorini, M. Johnston-Hollitt, H. Junklewitz, E. Orrù, et al. (Dec. 2017). “Observations of the galaxy cluster CIZA J2242.8+5301 with the Sardinia Radio Telescope”. In: MNRAS 472, pp. 3605–3623. DOI: `10.1093/mnras/stx2197`. arXiv: `1708.07125`.

Longair, M. S. (Feb. 2011). High Energy Astrophysics.

Macario, G., M. Markevitch, S. Giacintucci, G. Brunetti, T. Venturi, and S. S. Murray (Feb. 2011). “A Shock Front in the Merging Galaxy Cluster A754: X-ray and Radio Observations”. In: ApJ 728, pp. 82–+. DOI: `10.1088/0004-637X/728/2/82`. arXiv: `1010.5209 [astro-ph.CO]`.

Malarecki, J. M., D. H. Jones, L. Saripalli, L. Staveley-Smith, and R. Subrahmanyan (May 2015). “Giant radio galaxies - II. Tracers of large-scale structure”. In: MNRAS 449, pp. 955–986. DOI: `10.1093/mnras/stv273`. arXiv: `1502.03954`.

Marinacci, Federico, Mark Vogelsberger, Rüdiger Pakmor, Paul Torrey, Volker Springel, Lars Hernquist, Dylan Nelson, Rainer Weinberger, Annalisa Pillepich, Jill Naiman, and Shy Genel (Nov. 2018). "First results from the IllustrisTNG simulations: radio haloes and magnetic fields". In: MNRAS 480.4, pp. 5113–5139. DOI: `10.1093/mnras/sty2206`. arXiv: `1707.03396 [astro-ph.CO]`.

Markevitch, M. (Jan. 2006). "Chandra Observation of the Most Interesting Cluster in the Universe". In: The X-ray Universe 2005. Ed. by A. Wilson. Vol. 604. ESA Special Publication, p. 723. eprint: `astro-ph/0511345`.

Markevitch, M. and A. Vikhlinin (May 2007). "Shocks and cold fronts in galaxy clusters". In: PhysRep 443, pp. 1–53. DOI: `10.1016/j.physrep.2007.01.001`. eprint: `astro-ph/0701821`.

Marzke, R. O. (1998). "The Galaxy Luminosity Function at Zero Redshift: Constraints on Galaxy Formation". In: The Evolving Universe. Ed. by D. Hamilton. Vol. 231. Astrophysics and Space Science Library, p. 23. DOI: `10.1007/978-94-011-4960-0_3`.

Miniati, F., T. W. Jones, H. Kang, and D. Ryu (Nov. 2001). "Cosmic-Ray Electrons in Groups and Clusters of Galaxies: Primary and Secondary Populations from a Numerical Cosmological Simulation". In: ApJ 562, pp. 233–253. DOI: `10.1086/323434`. eprint: `astro-ph/0108305`.

Mondal, Mayukh, Jaume Bertranpetit, and Oscar Lao (Jan. 2019). "Approximate Bayesian computation with deep learning supports a third archaic introgression in Asia and Oceania". In: Nature Communications.

Mushotzky, R. F., J. Aird, A. J. Barger, N. Cappelluti, G. Chartas, L. Corrales, R. Eufrasio, A. C. Fabian, A. D. Falcone, E. Gallo, R. Gilli, C. E. Grant, M. Hardcastle, E. Hodges-Kluck, E. Kara, M. Koss, H. Li, C. M. Lisse, M. Loewenstein, M. Markevitch, E. T. Meyer, E. D. Miller, J. Mulchaey, R. Petre, A. J. Ptak, et al. (Mar. 2019). "The Advanced X-ray Imaging Satellite". In: arXiv e-prints. arXiv: `1903.04083 [astro-ph.HE]`.

Nelson, D., A. Pillepich, S. Genel, M. Vogelsberger, V. Springel, P. Torrey, V. Rodriguez-Gomez, D. Sijacki, G. F. Snyder, B. Griffen, F. Marinacci, L. Blecha, L. Sales, D. Xu, and L. Hernquist (Nov. 2015). "The illustris simulation: Public data release". In: Astronomy and Computing 13, pp. 12–37. DOI: `10.1016/j.ascom.2015.09.003`. arXiv: `1504.00362`.

Norris, R. P., A. M. Hopkins, J. Afonso, S. Brown, J. J. Condon, L. Dunne, I. Feain, R. Hollow, M. Jarvis, M. Johnston-Hollitt, E. Lenc, E. Middelberg, P. Padovani, I. Prandoni, L. Rudnick, N. Seymour, G. Umana, H. Andernach, D. M. Alexander, P. N. Appleton, D. Bacon, J. Banfield, W. Becker, M. J. I. Brown, P. Ciliegi, et al.

(Aug. 2011). “EMU: Evolutionary Map of the Universe”. In: PASA 28, pp. 215–248. DOI: `10.1071/AS11021`. arXiv: `1106.3219`.

Nuza, S. E., J. Gelszinnis, Matthias Hoeft, and G. Yepes (Aug. 2017). “Can cluster merger shocks reproduce the luminosity and shape distribution of radio relics?” In: MNRAS 470, pp. 240–263. DOI: `10.1093/mnras/stx1109`. arXiv: `1704.06661`.

Nuza, S. E., Matthias Hoeft, R. J. van Weeren, S. Gottlöber, and G. Yepes (Mar. 2012). “How many radio relics await discovery?” In: MNRAS 420, pp. 2006–2019. DOI: `10.1111/j.1365-2966.2011.20118.x`. arXiv: `1111.1721`.

Okabe, N. and G. P. Smith (Oct. 2016). “LoCuSS: weak-lensing mass calibration of galaxy clusters”. In: MNRAS 461, pp. 3794–3821. DOI: `10.1093/mnras/stw1539`. arXiv: `1507.04493`.

Owen, F. N., L. Rudnick, J. Eilek, U. Rau, S. Bhatnagar, and L. Kogan (Oct. 2014). “Wideband Very Large Array Observations of A2256. I. Continuum, Rotation Measure, and Spectral Imaging”. In: ApJ 794, 24, p. 24. DOI: `10.1088/0004-637X/794/1/24`. arXiv: `1408.5931`.

Paul, S., S. Salunkhe, A. Datta, and H. T. Intema (Mar. 2019). “Low-frequency radio study of MACS clusters at 610 and 235 MHz using the GMRT”. In: arXiv e-prints. arXiv: `1903.06799 [astro-ph.HE]`.

Peacock, J. A. (Feb. 1983). “Two-dimensional goodness-of-fit testing in astronomy”. In: MNRAS 202, pp. 615–627. DOI: `10.1093/mnras/202.3.615`.

Pfrommer, C., T. A. EnSSlin, V. Springel, M. Jubelgas, and K. Dolag (June 2007). “Simulating cosmic rays in clusters of galaxies - I. Effects on the Sunyaev-Zel’dovich effect and the X-ray emission”. In: MNRAS 378, pp. 385–408. DOI: `10.1111/j.1365-2966.2007.11732.x`. eprint: `astro-ph/0611037`.

Pinzke, A., S. P. Oh, and C. Pfrommer (Oct. 2013). “Giant radio relics in galaxy clusters: reacceleration of fossil relativistic electrons?” In: MNRAS 435, pp. 1061–1082. DOI: `10.1093/mnras/stt1308`. arXiv: `1301.5644 [astro-ph.CO]`.

Planck Collaboration, P. A. R. Ade, N. Aghanim, M. Arnaud, M. Ashdown, J. Aumont, C. Baccigalupi, A. J. Banday, R. B. Barreiro, R. Barrena, and et al. (Sept. 2016). “Planck 2015 results. XXVII. The second Planck catalogue of Sunyaev-Zeldovich sources”. In: A&A 594, A27, A27. DOI: `10.1051/0004-6361/201525823`. arXiv: `1502.01598`.

Prangle, D. (Dec. 2015). “Summary Statistics in Approximate Bayesian Computation”. In: ArXiv e-prints. arXiv: `1512.05633 [stat.CO]`.

Press, W. H. and P. Schechter (Feb. 1974). “Formation of Galaxies and Clusters of Galaxies by Self-Similar Gravitational Condensation”. In: ApJ 187, pp. 425–438. DOI: `10.1086/152650`.

Pritchard, J. K., M. T. Seielstad, A. Perez-Lezaun, and M. W. Feldman (Dec. 1999). "Population Growth of Human Y Chromosomes: A Study of Y Chromosome Microsatellites". In: SMBE 16.12, pp. 1791–1798. DOI: `10.1098/rsif.2008.0172`.

Pudritz, Ralph E. and Joseph Silk (July 1989). "The Origin of Magnetic Fields and Primordial Stars in Protogalaxies". In: ApJ 342, p. 650. DOI: `10.1086/167625`.

Rajpurohit, K., Matthias Hoeft, R. J. van Weeren, L. Rudnick, H. J. A. Röttgering, W. R. Forman, Marcus Brüggen, J. H. Croston, F. Andrade-Santos, W. A. Dawson, H. T. Intema, R. P. Kraft, C. Jones, and M. J. Jee (Jan. 2018). "Deep VLA Observations of the Cluster 1RXS J0603.3+4214 in the Frequency Range of 1–2 GHz". In: ApJ 852, 65, p. 65. DOI: `10.3847/1538-4357/aa9f13`. arXiv: `1712.01327`.

Rephaeli, Y. (Jan. 1979). "Relativistic electrons in the intracluster space of clusters of galaxies - The hard X-ray spectra and heating of the gas". In: ApJ 227, pp. 364–369. DOI: `10.1086/156740`.

Rephaeli, Yoel (Jan. 1988). "Magnetic fields in clusters of galaxies." In: Comments on Astrophysics 12, pp. 265–279.

Robert, C., J.-M. Marin, and N. S. Pillai (Jan. 2011). "Why approximate Bayesian computational (ABC) methods cannot handle model choice problems". In: ArXiv e-prints. arXiv: `1101.5091 [stat.CO]`.

Roettiger, K., J. O. Burns, and J. M. Stone (June 1999). "A Cluster Merger and the Origin of the Extended Radio Emission in Abell 3667". In: ApJ 518, pp. 603–612. DOI: `10.1086/307327`. eprint: `astro-ph/9902115`.

Röttgering, H., J. Afonso, P. Barthel, F. Batejat, P. Best, A. Bonafede, Marcus Brüggen, G. Brunetti, K. Chyy, J. Conway, F. de Gasperin, C. Ferrari, M. Haverkorn, G. Heald, Matthias Hoeft, N. Jackson, M. Jarvis, L. Ker, M. Lehnert, G. Macario, J. McKean, G. Miley, R. Morganti, T. Oosterloo, E. Orrù, et al. (Dec. 2011). "LOFAR and APERTIF Surveys of the Radio Sky: Probing Shocks and Magnetic Fields in Galaxy Clusters". In: Journal of Astrophysics and Astronomy 32, pp. 557–566. DOI: `10.1007/s12036-011-9129-x`. arXiv: `1107.1606`.

Ryu, D., H. Kang, E. Hallman, and T. W. Jones (Aug. 2003). "Cosmological Shock Waves and Their Role in the Large-Scale Structure of the Universe". In: ApJ 593, pp. 599–610. DOI: `10.1086/376723`. eprint: `astro-ph/0305164`.

Salvatier, John, Thomas V. Wieckiâ, and Christopher Fonnesbeck (Oct. 2016). PyMC3: Python probabilistic programming framework. ascl: `1610.016`.

Sarazin, C. L. (Jan. 1986). "X-ray emission from clusters of galaxies". In: Reviews of Modern Physics 58, pp. 1–115. DOI: `10.1103/RevModPhys.58.1`.

Schmit, C. J. and J. R. Pritchard (Mar. 2018). "Emulation of reionization simulations for Bayesian inference of astrophysics parameters using neural networks". In: MNRAS 475, pp. 1213–1223. DOI: `10.1093/mnras/stx3292`. arXiv: `1708.00011`.

Schowengerdt, R. A. (2007). Remote Sensing: Models and Methods for Image Processing. Elsevier Inc.

Sehgal, N., G. Addison, N. Battaglia, E. S. Battistelli, J. R. Bond, S. Das, M. J. Devlin, J. Dunkley, R. Dünner, M. Gralla, A. Hajian, M. Halpern, M. Hasselfield, M. Hilton, A. D. Hincks, R. Hlozek, J. P. Hughes, A. Kosowsky, Y.-T. Lin, T. Louis, T. A. Marriage, D. Marsden, F. Menanteau, K. Moodley, M. D. Niemack, et al. (Apr. 2013). "The Atacama Cosmology Telescope: Relation between Galaxy Cluster Optical Richness and Sunyaev-Zel'dovich Effect". In: ApJ 767, 38, p. 38. DOI: `10.1088/0004-637X/767/1/38`. arXiv: `1205.2369`.

Sembolini, F., G. Yepes, M. De Petris, S. Gottlöber, L. Lamagna, and B. Comis (Feb. 2013). "The MUSIC of galaxy clusters - I. Baryon properties and scaling relations of the thermal Sunyaev-Zel'dovich effect". In: MNRAS 429, pp. 323–343. DOI: `10.1093/mnras/sts339`. arXiv: `1207.4438`.

Shakouri, S., M. Johnston-Hollitt, and G. W. Pratt (July 2016). "The ATCA REXCESS Diffuse Emission Survey (ARDES) - I. Detection of a giant radio halo and a likely radio relic". In: MNRAS 459, pp. 2525–2538. DOI: `10.1093/mnras/stw812`.

Shimwell, T. W., M. Markevitch, S. Brown, L. Feretti, B. M. Gaensler, M. Johnston-Hollitt, C. Lage, and R. Srinivasan (May 2015). "Another shock for the Bullet cluster, and the source of seed electrons for radio relics". In: MNRAS 449, pp. 1486–1494. DOI: `10.1093/mnras/stv334`. arXiv: `1502.01064 [astro-ph.HE]`.

Shimwell, T. W., H. J. A. Röttgering, P. N. Best, W. L. Williams, T. J. Dijkema, F. de Gasperin, M. J. Hardcastle, G. H. Heald, D. N. Hoang, A. Horneffer, H. Intema, E. K. Mahony, S. Mandal, A. P. Mechev, L. Morabito, J. B. R. Oonk, D. Rafferty, E. Retana-Montenegro, J. Sabater, C. Tasse, R. J. van Weeren, Marcus Brüggen, G. Brunetti, K. T. Chyy, J. E. Conway, et al. (Feb. 2017). "The LOFAR Two-metre Sky Survey. I. Survey description and preliminary data release". In: A&A 598, A104, A104. DOI: `10.1051/0004-6361/201629313`. arXiv: `1611.02700 [astro-ph.IM]`.

Skillman, S. W., E. J. Hallman, B. W. O'Shea, J. O. Burns, B. D. Smith, and M. J. Turk (July 2011). "Galaxy Cluster Radio Relics in Adaptive Mesh Refinement Cosmological Simulations: Relic Properties and Scaling Relationships". In: ApJ 735, 96, p. 96. DOI: `10.1088/0004-637X/735/2/96`. arXiv: `1006.3559`.

Skillman, S. W., H. Xu, E. J. Hallman, B. W. O'Shea, J. O. Burns, H. Li, D. C. Collins, and M. L. Norman (Mar. 2013). "Cosmological Magnetohydrodynamic Simulations of Galaxy Cluster Radio Relics: Insights and Warnings for Observations". In: ApJ 765, 21, p. 21. DOI: `10.1088/0004-637X/765/1/21`. arXiv: `1211.3122`.

Springel, Volker and Glennys R. Farrar (Sept. 2007). "The speed of the 'bullet' in the merging galaxy cluster 1E0657-56". In: MNRAS 380.3, pp. 911–925. DOI: `10.1111/j.1365-2966.2007.12159.x`. arXiv: `astro-ph/0703232 [astro-ph]`.

Stobie, R. S. (Sept. 1980). "Analysis of astronomical images using moments". In: Journal of the British Interplanetary Society 33, pp. 323–326.

Takizawa, Motokazu, Ryo Nagino, and Kyoko Matsushita (Aug. 2010). "Mass Estimation of Merging Galaxy Clusters". In: PASJ 62, p. 951. DOI: `10.1093/pasj/62.4.951`. arXiv: `1004.3322 [astro-ph.CO]`.

Tavaré, S., D. J. Balding, R. C. Griffiths, and P. Donnelly (Dec. 1997). "Inferring Coalescence Times from DNA Sequence Data". In: Genetics Society of America 145.2, pp. 505–518.

Toni, T., D. Welch, N. Strelkowa, A. Ipsen, and MP. Stumpf (Feb. 2009). "Approximate Bayesian computation scheme for parameter inference and model selection in dynamical systems." In: JRSI 6.31, pp. 187–202. DOI: `10.1098/rsif.2008.0172`. arXiv: `0901.1925`.

Treumann, R. A. (Dec. 2009). "Fundamentals of collisionless shocks for astrophysical application, 1. Non-relativistic shocks". In: A&AR̃ev. 17, pp. 409–535. DOI: `10.1007/s00159-009-0024-2`.

van Weeren, R. J., F. Andrade-Santos, W. A. Dawson, N. Golovich, D. V. Lal, H. Kang, D. Ryu, M. Brìggen, G. A. Ogrean, W. R. Forman, C. Jones, V. M. Placco, R. M. Santucci, D. Wittman, M. J. Jee, R. P. Kraft, D. Sobral, A. Stroe, and K. Fogarty (Jan. 2017). "The case for electron re-acceleration at galaxy cluster shocks". In: Nature Astronomy 1, 0005, p. 0005. DOI: `10.1038/s41550-016-0005`. arXiv: `1701.01439 [astro-ph.HE]`.

van Weeren, R. J., F. de Gasperin, H. Akamatsu, Marcus Brüggen, L. Feretti, H. Kang, A. Stroe, and F. Zandanel (Jan. 2019). "Diffuse Radio Emission from Galaxy Clusters". In: arXiv e-prints. arXiv: `1901.04496 [astro-ph.HE]`.

van Weeren, R. J., H. J. A. Röttgering, Marcus Brüggen, and A. Cohen (Dec. 2009). "A search for steep spectrum radio relics and halos with the GMRT". In: A&A 508, pp. 75–92. DOI: `10.1051/0004-6361/200912501`. arXiv: `0910.2970`.

van Weeren, R. J., H. J. A. Röttgering, Marcus Brüggen, and Matthias Hoeft (Oct. 2010). "Particle Acceleration on Megaparsec Scales in a Merging Galaxy Cluster". In: Science 330, pp. 347–. DOI: `10.1126/science.1194293`. arXiv: `1010.4306 [astro-ph.CO]`.

Vazza, F. and Marcus Brüggen (Jan. 2014). "Do radio relics challenge diffusive shock acceleration?" In: MNRAS 437, pp. 2291–2296. DOI: `10.1093/mnras/stt2042`. arXiv: `1310.5707 [astro-ph.CO]`.

Vazza, F., Marcus Brüggen, C. Gheller, S. Hackstein, D. Wittor, and P. M. Hinz (Dec. 2017). "Simulations of extragalactic magnetic fields and of their observables". In: Classical and Quantum Gravity 34.23, 234001, p. 234001. DOI: `10.1088/1361-6382/aa8e60`. arXiv: `1711.02669`.

Vazza, F., Marcus Brüggen, C. Gheller, and P. Wang (Dec. 2014). "On the amplification of magnetic fields in cosmic filaments and galaxy clusters". In: MNRAS 445, pp. 3706–3722. DOI: `10.1093/mnras/stu1896`. arXiv: `1409.2640`.

Vazza, F., Marcus Brüggen, R. van Weeren, A. Bonafede, K. Dolag, and G. Brunetti (Apr. 2012). "Why are central radio relics so rare?" In: MNRAS 421, pp. 1868–1873. DOI: `10.1111/j.1365-2966.2011.20160.x`. arXiv: `1111.1720`.

Wenger, M., F. Ochsenbein, D. Egret, P. Dubois, F. Bonnarel, S. Borde, F. Genova, G. Jasniewicz, S. Laloë, S. Lesteven, and R. Monier (Apr. 2000). "The SIMBAD astronomical database. The CDS reference database for astronomical objects". In: A&A S 143, pp. 9–22. DOI: `10.1051/aas:2000332`. eprint: `astro-ph/0002110`.

White, M. (Feb. 2001). "The mass of a halo". In: A&A 367, pp. 27–32. DOI: `10.1051/0004-6361:20000357`. eprint: `astro-ph/0011495`.

Wittor, D., F. Vazza, and Marcus Brüggen (Feb. 2017). "Testing cosmic ray acceleration with radio relics: a high-resolution study using MHD and tracers". In: MNRAS 464, pp. 4448–4462. DOI: `10.1093/mnras/stw2631`. arXiv: `1610.05305 [astro-ph.HE]`.

Wylezalek, D., J. Vernet, C. De Breuck, D. Stern, M. Brodwin, A. Galametz, A. H. Gonzalez, M. Jarvis, N. Hatch, N. Seymour, and S. A. Stanford (May 2014). "The Galaxy Cluster Mid-infrared Luminosity Function at $1.3 < z < 3.2$". In: ApJ 786, 17, p. 17. DOI: `10.1088/0004-637X/786/1/17`. arXiv: `1403.2390`.

Yang, H.-Y. K. and C. S. Reynolds (Oct. 2016). "How AGN Jets Heat the Intracluster Medium - Insights from Hydrodynamic Simulations". In: ApJ 829, 90, p. 90. DOI: `10.3847/0004-637X/829/2/90`. arXiv: `1605.01725 [astro-ph.HE]`.

Young, R. A. (1987). The Gaussian derivative model for spatial vision: I. Retinal mechanisms. Vol. 2. Oxford: Pergamon Press, pp. 273–293. DOI: `10.1163/156856887X00222`.

Yuan, Z. S., J. L. Han, and Z. L. Wen (Nov. 2015). "The Scaling Relations and the Fundamental Plane for Radio Halos and Relics of Galaxy Clusters". In: ApJ 813, 77, p. 77. DOI: `10.1088/0004-637X/813/1/77`. arXiv: `1510.04980`.

Zinger, E., A. Dekel, Y. Birnboim, D. Nagai, E. Lau, and A. V. Kravtsov (May 2018). "Cold fronts and shocks formed by gas streams in galaxy clusters". In:

MNRAS 476.1, pp. 56–70. DOI: `10.1093/mnras/sty136`. arXiv: `1609.05308 [astro-ph.GA]`.

Zuhone, J. and M. Markevitch (Dec. 2009). “Cluster Core Heating from Merging Subclusters”. In: American Institute of Physics Conference Series. Ed. by S. Heinz and E. Wilcots. Vol. 1201. American Institute of Physics Conference Series, pp. 383–386. DOI: `10.1063/1.3293082`. arXiv: `0909.0560`.

Appendix A

NVSS additional tables

(please turn over page)

TABLE A.1: Non-exhaustive list of relic-hosting clusters, excluded from further analysis. Relics are excluded when: (i) the origin is most likely not shock acceleration, i.e. not gischt; (ii) the object was not mapped by NVSS , i.e. the source declination is to low; (iii) the emission is too faint; (iv) the relic cluster has a $z < 0.05$, hence NVSS cannot recover the flux density, and (v) the contamination by other sources is deemed to be too strong.

Cluster (1)	z [] (2)	M_{200} $[10^{14} M_\odot]$ (3)	S_{NVSS} [mJy] (4)	$S_{1.4,\mathrm{lit}}$ [mJy] (5)	Diff. Emi. RHR* (6)	References mass | relics (7)
1E 0657-55	0.296	25.1	low Dec	82.6	(•	Gio09 - Shi15
24P73	0.150	nan	not gischt	12.8	*	- Wee11b
0809+39	0.200	nan	too faint,no cluster	62.6	(	- Bro09
A13	0.094	4.0	not gischt	31.0	*	Fer12 - Slee01
A85	0.055	9.1	not gischt	43.0	*	Fer12 - Slee01
A133	0.057	5.5	not gischt	137.0	*	Ebe96 - Ran10
A209	0.206	11.2	too faint	0.7	(•	Gio09 - Gio09
A523	0.104	3.7	too faint	61.0	(• *	Fer12 - Wee11a
A548b	0.042	1.0	low z	121.0	( )	Fer12 - Fer06
A725	0.092	2.1	not gischt	6.0	*	Böh00 - Kem01
A754	0.054	6.0	too faint	6.0	(•	Fer12 - Mac11
A768	0.076	nan	not gischt	*nan*	*	-
A786	0.124	nan	not gischt	*nan*	*	-
A910	0.205	7.6	contam.,too faint	12.1	(	Ebe00 - Gov12
A959	0.288	7.8	not gischt,too faint	*nan*	•	Bir19 - Bir19
A1033	0.126	9.3	not gischt	46.9	*	Gas15b - Gas15b
A1367	0.022	3.2	low z,too faint	232.0	(•	Far13 - Far13
A1656	0.023	9.1	low z,too faint	260.0	(•	Fer12 - Fer12
A1758S	0.279	8.3	too faint	1.5	(	-
A2048	0.097	5.4	not gischt	19.0	*	Wee11b - Wee11b
A2063	0.078	3.5	not gischt	77.6	*	Fer12 - Kom94
A2146	0.035	3.8	low z,too faint	1.1	(•	- Hla17
A2255	0.081	6.8	too faint	23.0	(• *	Fer12 - Piz08
A2443	0.108	5.4	not gischt,contam.	6.5	*	Fer12 - Coh11
A3376	0.046	3.8	low z	302.0	( )*	Fer12 - Bag06
A3667	0.056	10.0	low Dec	1200.0	(*	Fer12 - Roe97
A4038	0.030	5.8	low z,not gischt	49.0	*	Fer12 - Slee01
ACT-CLJ01-49	0.870	37.2	low Dec	8.6	(• *	Lin14 - Lin14
A S753	0.014	2.3	low z,not gischt	460.0	*	Sub03 - Sub03
CL 0217+70	0.066	2.6	too faint	*nan*	(*	Fer12 - Bro11
CL 1446+26	0.370	6.9	contam.,too faint	5.3	(•	Fer12 - Gov12
MACS J0025	0.586	11.5	too faint	2.3	(*	Ebe07 - Ris17
MACS J0152	0.413	7.9	not gischt,too faint	1.0		- Pau19
MACS J2243	0.447	14.8	too faint	1.9	(	Can16 - Can16
MaxBCG 138+25	0.324	nan	not gischt	24.7	*	- Wee11b
MaxBCG 217+13	0.160	3.4	not gischt,contam.	14.6	*	Wee09 - Wee09
RXC J1234	0.229	11.2	too faint	3.1	(•	Kal15 - Kal15
S1081	0.220	nan	too faint,low Dec	2.4	(	- Mid08
KMA2007	0.160	3.4	not gischt	*nan*	*	-

TABLE A.2: Table of relic of sources that were subtracted from the NVSS images to receive clean relic regions.

Cluster (1)	RA [deg] (2)	Dec [deg] (3)	flux [mJ] (4)	type (5)	Θ_{major} [′] (6)	Θ_{minor} [′] (7)	θ [deg] (8)
1RXS J06+42	90.933	42.196	0.8	Point			
1RXS J06+42	90.940	42.229	0.6	Point			
1RXS J06+42	90.963	42.226	0.6	Point			
A115	-13.960	26.410	905.0	Extended	1.00	0.75	35
A115	-14.014	26.454	194.0	Extended	0.85	0.77	35
A115	-14.094	26.469	8.2	Point			
A521	73.568	-9.731	15.5	Point			
A746	137.185	51.550	6.9	Point			
A1240	170.853	43.169	1.0	Point			
A1240	170.891	43.176	0.8	Point			
A1443	180.298	23.093	77.0	Point			
A1612	191.969	-1.169	125.7	Extended	0.90	0.90	0
A1664	195.918	-23.682	35.0	Point			
A1682	196.690	46.559	145.0	Point			
A1682	196.707	46.559	3.5	Point			
A1682	196.763	46.563	1.2	Point			
A1682	196.692	46.561	10.2	Extended	0.90	0.75	150
A1682	196.695	46.556	16.2	Extended	0.90	0.75	150
A1758N	203.223	50.527	94.0	Extended	0.83	0.75	42
A1758N	203.236	50.529	5.0	Extended	0.83	0.75	42
A1758N	203.164	50.576	4.2	Point			
A1758N	203.160	50.560	5.4	Point			
A2061	229.993	30.567	4.7	Point			
A2256	255.592	78.683	1.7	Extended	7.00	0.79	15
A2345	321.893	-11.817	23.8	Point			
A2345	321.687	-11.875	25.3	Extended	1.00	0.75	80
A2345	321.703	-11.886	8.0	Point			
A2345	321.627	-11.843	2.4	Point			
A3411	130.519	-16.431	5.6	Point			
A3411	130.517	-16.428	4.0	Point			
A3527-bis	192.796	-35.013	5.5	Point			
A3527-bis	192.792	-35.017	3.2	Extended	0.88	0.88	50
CIZA J0107	16.954	54.116	1.5	Point			
CIZA J0107	16.948	54.116	3.0	Point			
CIZA J0107	16.910	54.084	0.8	Point			
CIZA J0107	16.966	54.150	1.0	Point			
CIZA J2243	340.829	53.119	24.0	Point			
CIZA J2243	340.605	52.974	6.9	Point			
MACS J0717	109.391	37.757	10.7	Extended	2.30	1.50	78
MACS J0717	109.404	37.739	0.2	Extended	1.10	0.75	120
MACS J0717	109.404	37.739	9.8	Point			
MACS J0717	109.386	37.750	15.4	Extended	0.95	0.75	30
MACS J1149	177.343	22.392	8.2	Point			
MACS J1149	177.428	22.345	1.5	Point			
PLCK G200	72.597	-2.957	1.5	Point			
PLCK G200	72.568	-2.968	1.5	Point			
PLCK G287	177.740	-27.967	7.0	Point			
PLCK G287	177.719	-27.965	2.3	Point			
PSZ1 G004	289.255	-32.492	8.0	Extended	0.90	0.80	70
PSZ1 G004	289.254	-32.493	10.3	Extended	1.10	0.80	70
PSZ1 G097	284.142	66.422	4.3	Point			
PSZ1 G097	284.163	66.368	10.5	Point			
ZwCl 0008	-2.837	52.529	280.0	Extended	1.20	0.81	50
ZwCl 0008	-2.802	52.544	44.0	Extended	0.85	0.85	0
ZwCl 0008	-2.844	52.473	44.0	Extended	1.40	0.75	60
ZwCl 2341	355.943	0.267	1.4	Extended	1.30	0.90	50

Appendix B

Difference between radiative and adiabatic MUSIC-2 simulations

Many hydrodynamic simulations tread the ICM with the adiabatic equation of state for gas, with the ratio of specific heat Γ being 5/3. The MUSIC-2 simulations were performed twice: Once with the adiabatic formalism and a second time with additional radiative physics. We take this as a opportunity to investigate if these different formalism and degrees of detail have an influence on our results. Radiative processes are implemented to make the thermal profile of the galaxy clusters more realistic. This physics includes cooling through bremsstrahlung and heating through AGN and star formation. As seen in Fig. B.1 the implementation of such does change the small-scale structures of galaxy clusters.

The ICMs bremsstrahlung facilitates the collapse from dense and isolated structures, to galaxies. Galaxies by themselves do not emit bremsstrahlung but heat the medium through star formation and AGN feedback. Kang et al. (2007) and Pfrommer et al. (2007) investigated the impact of radiative physics on the thermal profiles and shock properties of galaxy clusters. They found a remarkable similarity for adiabatic simulations and those with additional radiative physics. We ask if our synthetic survey the notion of Skillman et al. (2013) that adiabatic simulations might be sufficient to simulated cluster-wide shocks, and even be favored to make a disentanglement between . To facilitate a direct comparison, for both physics models we create survey products with an identical choice of mock-clusters and cluster orientations. We use the same magnetic field model used by Nuza et al. (2017) and choose an efficiency which leads to the detection of around 100 relic cluster from $z = 0.0 \ldots 0.7$ at NVSS -like resolution and frequency the survey.

In agreement with Kang et al., 2007, Fig.1 we see that implementation of radiative physics leads to the formation of galaxies and stars (see Fig. B.2). The rightmost panel

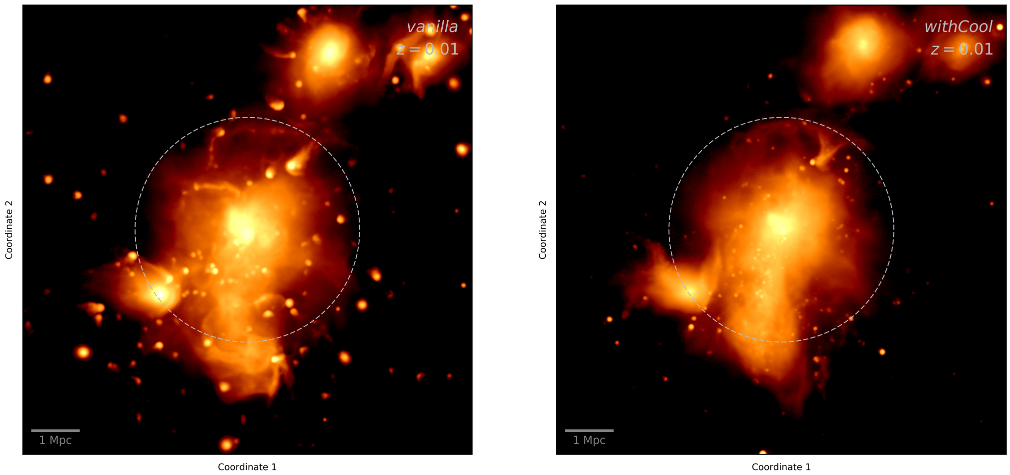

FIGURE B.1: Projection of the bolometric bremsstrahlung emission (particles above 3000 K) of the most massive cluster in MUSIC-2 without (left) and with cooling & star formation (right). Both radiative and adiabatic simulations lead to a similar merging state of galaxy clusters.

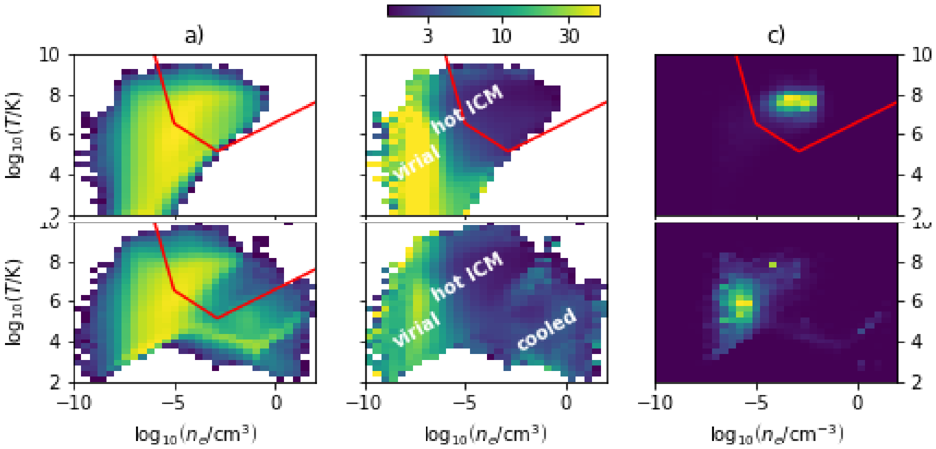

FIGURE B.2: Shown is the temperature T and density n_e assigned to SPH particles with $\mathcal{M} > 1.5$ in mock clusters with relic detections for adiabatic (top) and radiative (down) simulations. Plotted are particle numbers (left, logarithmic color-scale) average Mach number (middle), and radio power (right). The red line shows the boundaries of a former particle filter in the phase space that is not used anymore for this study. In agreement with Skillman et al. (2013), within the adiabatic simulation the majority of relic emission happens in a particular region of the temperature, electron number density, and Mach number phase space. In contrast, for the radiative simulation, the majority of emission is found for particles that are not attributed to the hot ICM.

of Fig. B.2 shows that, the distribution of radio emission in the density-temperature phase space is vastly different. While the Mach-numbers in the virial region of the radiative simulation are in average weaker there is more emission found in the transition region from virial to the hot ICM .

In fact this emission dominates by far the ICM radio emission for our particular radiative simulation. This emission predominantly does not show up as ICM shocks but as small ($< 200\,\mathrm{kpc}$) structures. with high surface brightness. Due to our best knowledge these shocks arise from the numerical implementation of galaxy heating by AGN feedback.

As we want to quantify if the relics in the cooling simulation differ from those in the non-cooling one we have to do a separation between relics and AGN /galaxy induced shocks. We accomplish this by a particle filter in the phase-space of particle properties and in the image plane removes most of the contaminating emission. Density and temperature space are chosen such that the detections of the adiabatic simulation are fully included.

Due to a limited resolution most large scale cosmological simulations will include this confusion with shocks from star/galaxy feedback. In future it will remain paramount for relic studies to further disentangle these shocks, which might simply arise from the feedback scheme from cluster merger shocks. Hence, our methods to disentangle them might remain relevant.

Appendix C

Parameter inference with a Monte-Carlo-Markov-Chain

We used the tool *pymc3* (Salvatier et al., 2016) to infer the model parameters via a Monte-Carlo-Markov-Chain process and plotted the inferred results in Fig.C.1. The distribution shows an uncorrelated estimate of the two parameters μ and σ with the same offset and uncertainty in the parameter estimation as created via ABC.

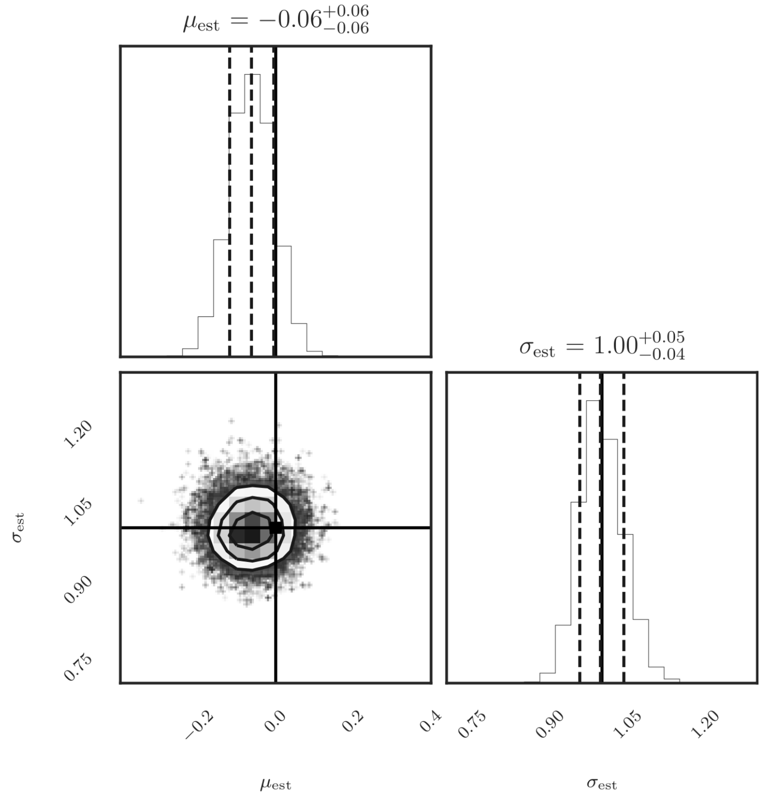

FIGURE C.1: Shown is the result of previous inference task with a so-called Markov-Chain-Monte-Carlo process; plotted via *corner* (Foreman-Mackey, 2016). The black, crossed line in the 2D-density plot denote the true parameter values.

Appendix D

Runtime requirements of ABCPMC and performance improvements

We took several measures to limit the runtime of the ABC-pmc process to less then one week:

I) Parallelization: Using more CPUs per run would speeds up the hole procedure if the process is CPU-power limited. In most off our cases the computation is however limited. Most notably is the need to read each dataset once per model evaluation. One might decrease this need by letting each process compute more than one model or in general by making the datasets available to the working memory. Because of the input/output (I/O) limitation we focus our measures on decreasing I/O.

II) Restricted sampling to clusters with likely detections: Severe speed-ups can be achieved when only considering those cluster in the (redshift,Mass) plane that also show detections in the real world survey. Not considering all clusters will decrease the strength of the ABC approach. We use the criterion defined by Eq. 3.20 to reduce the number of MUSIC-2 clusters that have to be simulated by more than 70 percent.

III) Restricted to resolution elements linked to radio emission: The computation of radio brightness and subsequent binning has to be run over each resolution elements. By choosing the few % of elements from which we would expect most of our emission we can speed up this procedure dramatically. For our analysis we use only consider shocked particles with $M > 1.5$. Due to this measure we are able to reduce the file size by an factor of 25. These particle filters are only viable for the generation of the radio-maps. X-Ray maps need the full number of particles - but luckily the generation of this can be limited to the small fraction of clusters that actually show a radio relic.

IV) Optimized I/O: We increased the load speed of cluster files through usage of Solid-State-Disk (SSD) memory by a factor of about 10. For our initially I/O limited procedure we were able to reduce the load time, so that the tasks is now CPU limited. Combined with I) and II) we limit the data-set that has to be read from memory to 2000 files of 5 MB each i.e. 10 GB per model evaluation. With a hard disk drive (HDD) we reach a read speed of $\sim$ 20 GB per minute, SSD performance was 200 GB per minute.

With this approach one can compute about two model-realizations/hour/core in MUSIC-2 for the standard DSA model. A future routine would strongly benefit from further performance improvements. The usage of computing clusters, optimizing the most resource-consuming subroutines, and graphics processing unit (GPU) usage are some options. Note that ABC of this scope is only viable, because we perform it in a post-processing manner: The most costly part i.e. the cosmological simulation itself is not redone. Performing ABC on the cosmological simulation in its whole would require considerable advances in the forward modeling of galaxy-cluster mergers and is out of scope of this work.

List of Abbreviations

ABC	approximate Bayesian computation 11–13
ABC-pmc	ABC population Monte Carlo 12
AGN	active galactic nuclei 8, 10
CPU	central processing unit 12
CR	cosmic ray 3
DSA	diffusive shock acceleration 3, 13
GPU	graphics processing unit 13
HDD	hard disk drive 13
I/O	input/output 12
ICM	intracluster medium 3, 8, 9
MUSIC-2	Marenostrum-MultiDark SImulations of galaxy Clusters second simulation suite 8, 9, 12, 13
NVSS	NRAO VLA Sky Survey 6–8
SPH	smoothed particle hydrodynamics 9
SSD	Solid-State-Disk 12, 13

Ehrenwörtliche Erklärung

Ich erkläre hiermit ehrenwörtlich, dass ich die vorliegende Arbeit selbständig, ohne unzulässige Hilfe Dritter und ohne Benutzung anderer als der angegebenen Hilfsmittel und Literatur angefertigt habe. Die aus anderen Quellen direkt oder indirekt übernommenen Daten und Konzepte sind unter Angabe der Quelle gekennzeichnet.

Bei der Auswahl und Auswertung folgenden Materials haben mir die nachstehend aufgeführten Personen in der jeweils beschriebenen Weise entgeltlich/unentgeltlich geholfen:

1. Dr. Matthias Hoeft - durch seine fachliche Betreuung der vorliegenden Arbeit,
2. Dr. Sebastián E. Nuza, - durch die gemeinsame Arbeit an einer wissenschaftlichen Publikation, auf deren Konzept diese Thesis aufbaut.

Weitere Personen waren an der inhaltlich-materiellen Erstellung der vorliegenden Arbeit nicht beteiligt. Insbesondere habe ich hierfür nicht die entgeltliche Hilfe von Vermittlungs- bzw. Beratungsdiensten (Promotionsberater oder andere Personen) in Anspruch genommen. Niemand hat von mir unmittelbar oder mittelbar geldwerte Leistungen für Arbeiten erhalten, die im Zusammenhang mit dem Inhalt der vorgelegten Dissertation stehen.

Die Arbeit wurde bisher weder im In- noch im Ausland in gleicher oder ähnlicher Form einer anderen Prüfungsbehörde vorgelegt. Die geltende Promotionsordnung der Physikalisch-Astronomischen Fakultät ist mir bekannt. Ich versichere ehrenwörtlich, dass ich nach bestem Wissen die reine Wahrheit gesagt und nichts verschwiegen habe.

Ort, Datum	Unterschrift d. Verfassers